

## PDF hosted at the Radboud Repository of the Radboud University Nijmegen

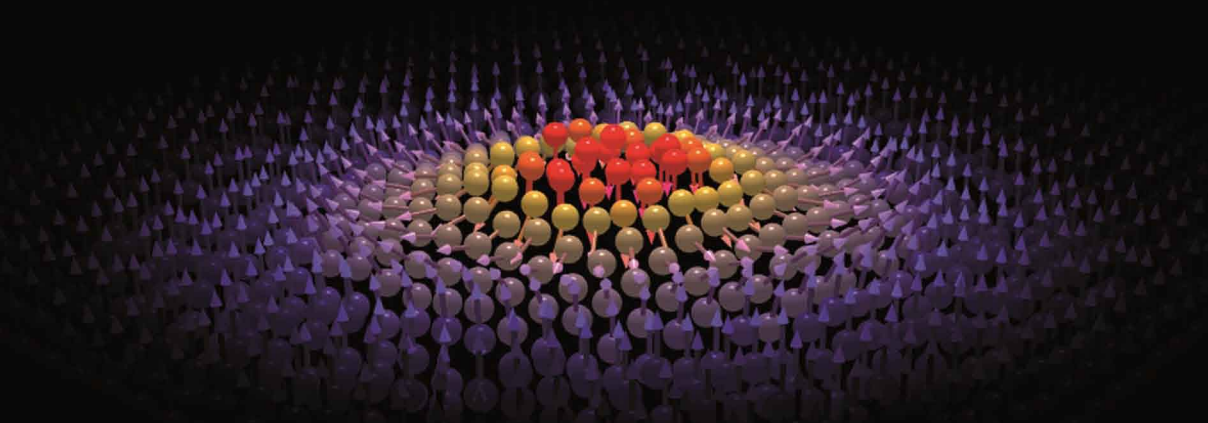
The following full text is a publisher's version.

For additional information about this publication click this link.

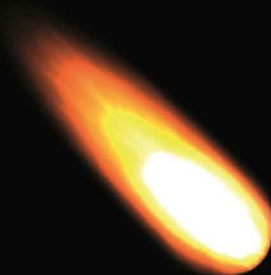
<http://hdl.handle.net/2066/106921>

Please be advised that this information was generated on 2017-12-06 and may be subject to change.

# Spectroscopic Study of Ultrafast Laser-Induced Magnetization Reversal



Sam Khorsand



# **Spectroscopic Study of Ultrafast Laser-Induced Magnetization Reversal**

Sam Khorsand

---

Copyright © 2013, by A.R. Khorsand

Printed by Ipskamp Drukkers B.V., Enschede, The Netherlands  
ISBN: 978-94-6191-641-9

A digital version of this thesis can be downloaded from <http://www.ru.nl>.

# **Spectroscopic Study of Ultrafast Laser-Induced Magnetization Reversal**

## **Proefschrift**

ter verkrijging van de graad van doctor  
aan de Radboud Universiteit Nijmegen  
op gezag van de rector magnificus prof. mr. S. C. J. J. Kortmann,  
volgens besluit van het college van decanen  
in het openbaar te verdedigen op dinsdag 5 maart 2013  
om 15:30 uur precies

door

**Ali Reza Khorsand**

geboren op 17 mei 1984  
te Teheran, Iran

**Promotoren:** Prof. dr. Th.H.M. Rasing  
Prof. dr. A.I. Kirilyuk

**Copromotor:** dr. A.V. Kimel

**Manuscriptcommissie:**

Prof. dr. A. Fasolino

Prof. dr. U. Bovensiepen    University Duisburg-Essen, Germany

Prof. dr. B. Koopmans    Eindhoven University of Technology

The work described in this thesis was financially supported by the Foundation for Fundamental Research on Matter (FOM), and partly by The Netherlands Organization for Scientific Research (NWO), the European Union's Seventh Framework Programme (FP7/2007-2013) Grants No. NMP3-SL-2008-214469 (UltraMagnetron), No. 214810 (FANTOMAS) as well as the European Research Council under the European Union's Seventh Framework Programme (FP7/2007-2013)/ERC Grant agreement No 257280 (Femtomagnetism).

---

## Preface

---

I remember very well the first time I met "magnetism". I'm playing with my action man. I was quite sure that he was the strongest man in the world. When I looked at a corner full of toys, I noticed a very strange "toy". In retrospect, I am convinced that this thing got in the toy section by some mistake, although after four years of PhD research I can defend that it was really a toy. I picked it up and looked at it to understand what you can do with this toy. It was grey, as round as a coin but it was much thicker. At a first glance it seemed quite boring, but that would change very soon. The toy fell out of my hand and broke in four equal pieces, each as thick as a coin. I tried to stack them back on top of each other. To my surprise, the first two coins glued back to each other! I was amazed! The third coin, however, jumped away when I tried to stack it. I found this toy just as interesting and confusing as the magic tricks of my dad. For a moment, I had lost the fourth coin. Then I looked at my action man and saw that it was glued to his belt. This was the proof: my action man really has super powers! I took this coin and tried to stick it on any object I saw in the kindergarten. I took it even home for a day.

In a way, magnets really are magic toys. Millenia after their discovery, they keep surprising scientists with novel phenomena and new physical concepts. It has been a great pleasure to work on these fascinating materials twenty years after my own discovery of magnetism.

You cannot do a PhD successfully on your own. From my current research group back to my university and even high school, I have met many people who have had an influence on this book in one way or another. I am truly indebted and grateful to everyone.

First of all, it has been a great honor and privilege to do my PhD research under

the supervision of Theo Rasing, Andrei Kirilyuk, and Alexey Kimel in one of the world's leading research groups in ultrafast magnetism.

I'd like to thank Theo Rasing for giving me the opportunity to work in this group. I greatly appreciate your sharp criticism and positive comments on my manuscripts, presentations, referee reports, and other scientific contributions. Your deep knowledge on many topics has been very valuable to me, and essential for this work.

Another man who has been invaluable for this thesis is Andrei Kirilyuk. As a master student attending Physics@FOM, I was fascinated by Andrei's talk about the research this group was doing. Your presentation was one of my reasons to send Theo an open application for a PhD position, one year later. That alone is worth a huge thank you! Furthermore, you taught me a lot on magneto-optics with your immense knowledge by answering the many questions I had without ever losing your patience. During my PhD, your door was always open for discussions. I have very much appreciated our discussions on my experimental results, and your suggestions for additional measurements when needed.

I am also very grateful to Alexey Kimel. I have learned a lot from your great knowledge and deep understanding of ultrafast phenomena in magnets. You have also a talent for presenting science, and that made your comments to my scientific work even more valuable. You pushed me to my limits with our discussions, and it has been a privilege to be supervised by one of the pioneers in the field of ultrafast magnetism. You have also been much more than a supervisor to me because of our common interest in football. It was a great pleasure to be team mates with you in UniVV, and the feared Huygens United.

My sincere thanks go to Marilou who made sure that my mind would not get too much distracted from my research. You have been always ready to help me with all the administrative things. Your good mood, continuous smiles and even singing in the halls makes sure that there is no room for stress in our group.

I am truly thankful to Dr. Arata Tsukamoto and Prof. Akiyoshi Itoh from Nihon University, Japan. They provided me TbFeCo and GdFeCo samples (magic magnets) which I used extensively. Without our close collaboration, this work would have been impossible.

Furthermore, I'd like to thank our excellent technical staff who supported the experiments. I could always approach Andre with laser-problems and you would do your best to solve them. I really admire your friendly and effective style of working. Tonnie's support in the lab was also incredibly important. I enjoyed working with you and I am very grateful for your help, and also for all the parts you made in the workshop for my experimental setup. Finally, I'd like to thank Albert. Your experience with and deep knowledge about laser systems has been very valuable to me, and to the group as a whole.

I would also like to thank my thesis committee members, Prof. Annalisa Fasolino, Prof. Bert Koopmans, and Prof. Uwe Bovensiepen for their time, interest, and helpful



feedback.

Motivators sometimes say: “the journey is the reward, not the destination”. This certainly does not always apply to PhD research. As a PhD researcher you have a lot of freedom, and at times I felt it was working against me because the direction I had chosen seemed to have a dead end. Therefore, if someone had said that sentence to me during the first half of my PhD, I would have laughed and considered it naive. But the same freedom allowed me to change subject. I continued in a new direction starting with some unorthodox measurements, which perhaps some others considered to be a dead end in the beginning. But it turned out to be the best decision I made, and it marked a turning point in my PhD research. We obtained some great new insights on all-optical magnetic recording, and this thesis is a product of that. Like for most other PhD’s, this journey was not a straight line, but perhaps that is the reason why I could enjoy the second half even more than I would have otherwise.

Nevertheless, because of my fantastic colleagues I could *always* go to work with great pleasure. I had great joy with the after-lunch table football matches, our feared and victorious Huygens United team, the visits to café Jos, the dinners at Don Pablo, the BBQ’s at Theo and Maria’s place, and many other events. I am very grateful to all my colleagues who gave me a wonderful time to look back at: Addis, Alex, Benny, Bowen, Chris, Davide, Dennis, Diana, big Dima, little Dima, Duncan, Fred, Hiroyuki, Ilie, Ilya, Jan, Jelena, Jeroen, Jing, Johan dJ, Johan M, Jonas, Joris, Jos, Katsunori, Kadir, Koen, Lars, Laura, Loic, Magnus, Michiel, Minko, Mathieu, Matteo, Magnus, Raja G, Ruslan, Sasha, Sergey, Shekar, Shoken, Siebe, Tahoorra, Thomas, Wei-Ta, Weizhe, and Yusuke.

I worked a lot, more than with anyone else, with Matteo. We found each other very soon after you came to Nijmegen, and immediately we involved each other in our projects. I learned a lot from your expertise in near-field optics, and the immense amount of scientific discussions we had. Apart from the many nice memories of doing research together (yes, no, no, yes, yes, no... $\times 1000$ ), going to a conference or summer school together with you was a guarantee for great fun. I can only hope to have such a colleague in my further carrier.

At the beginning of my PhD, it was Ilie who taught me important lab-skills for doing ultrafast pump-probe measurements. Special thanks to you for patiently sharing your expertise with me. I started my PhD together with Jan, with whom I performed my first static magneto-optical measurements. Thank you, also for being my Mathematica-companion! Later, I would work regularly together with Shekar and Addis, and we wrote nice publications together. Thank you for your collaboration. Just a few day before this writing, Addis had become a doctor on a memorable day.

Together with Jonas, Minko, and Alexey, I have been a member of UniVV. Special thanks go to all players of my favorite football team! You guys made sure that I had at least a few days a week to put my mind on something completely different.

Before I came to this group, I worked on thin film Bragg reflectors for the next

generation of lithography machines in the group of Fred Bijkerk. Although that was a very different topic than “ultrafast magnetism”, the theory I learned on light-matter interaction and the programs which I had written during that period, played an important role in the success of my PhD research. I’d like to thank Ryszard Sobierajski, Eric Louis, Fred Bijkerk, and the whole nSI research group.

I am also grateful to one of my motivators to do physics in the first place: my high-school teacher “meneer Manders”. Thank you for sharing your passion and knowledge of physics with me, and challenging us with beyond-textbook-exercises.

Most importantly, I would like to thank my lovely family for the unconditional support, interest, and care during the last four years, and all the years before. To my parents, this book is a product of the choices you made long ago. Thank you, and I’m truly proud of you! Special thanks go to my brother Salar. Being a physicist too, he made sure that I could always talk in full detail about my research, even if I was far away from my colleagues. My older brother Reza made me thrilled about science on a very young age through his great knowledge of astronomy and mathematics. Nakisa gave me the two most beautiful presents, and I could always share my PhD experiences with her. My oldest sister Panthea has been always supportive and very curious about my research. Thank you all, including Kees, Pari, Simon, Irene, Kiarash, Harry, Yvonne, Cristijn, and Coreline for your invaluable support.

Finally, my deepest gratitude go to Rosanne. Regularly, I had to go to the lab in the weekends, in the evenings or in the middle of the nights. Although it must have been inconvenient for you, you have always fully supported me and sometimes you even joined me in the lab! Thank you for all your support and encouragement.

Sam Khorsand

*15th of January, 2013.*

---

# Contents

---

<b>1</b>	<b>Introduction</b>	<b>1</b>
1.1	Magnetism and Technology . . . . .	2
1.2	Precessional Motion . . . . .	4
1.3	Ultrafast Laser-Induced Magnetization Dynamics . . . . .	6
1.4	Ultrafast All-Optical Magnetic Recording . . . . .	7
1.4.1	Multiple Shot Switching . . . . .	7
1.4.2	Single Shot Switching . . . . .	8
1.4.3	Multisublattice Dynamics . . . . .	10
1.5	Contribution and Scope of this Thesis . . . . .	11
<b>2</b>	<b>Rare-Earth Transition-Metal Alloys</b>	<b>17</b>
2.1	Introduction . . . . .	18
2.2	3d Transition Metals . . . . .	18
2.3	4f Rare Earth Metals . . . . .	19
2.4	Amorphous RE-TM Alloys . . . . .	21
2.4.1	Light and Heavy RE-TM Alloys . . . . .	22
2.4.2	Magnetic Properties of Heavy RE-TM Alloys . . . . .	22
2.4.3	Magnetic Structure: Sperrimagnetism . . . . .	25
2.4.4	Magneto-Optical Properties . . . . .	27
2.5	Materials under Study . . . . .	27
2.5.1	Growth . . . . .	28
2.5.2	GdFeCo . . . . .	28
2.5.3	TbFeCo . . . . .	29
2.6	Summary . . . . .	31

<b>3</b>	<b>Experimental Methods</b>	<b>37</b>
3.1	Introduction . . . . .	38
3.2	Measuring Magnetism with Light . . . . .	39
3.2.1	Linear Magneto-Optics . . . . .	40
3.2.2	Magnetic Circular Birefringence . . . . .	41
3.2.3	Magnetic Circular Dichroism . . . . .	42
3.2.4	Detection Scheme . . . . .	42
3.2.5	Magneto-Optical Imaging . . . . .	45
3.3	Measuring Ultrafast Magnetization Dynamics . . . . .	46
3.3.1	Femtosecond Amplified Laser System . . . . .	46
3.3.2	Ultrafast Magneto-Optical Pump-Probe Setup . . . . .	48
3.4	Optical Properties . . . . .	50
3.4.1	Optical Response of a Multilayer . . . . .	51
3.4.2	Variable Angle Spectroscopic Ellipsometer . . . . .	56
3.5	Summary . . . . .	58
<b>4</b>	<b>Role of Light in All-Optical Magnetic Recording</b>	<b>61</b>
4.1	Introduction . . . . .	62
4.2	Sample . . . . .	63
4.2.1	Optical Characterization . . . . .	63
4.2.2	Magneto-Optical Characterization . . . . .	64
4.3	Experimental Details . . . . .	64
4.4	Results and Discussion . . . . .	67
4.4.1	Inverse Faraday Effect . . . . .	69
4.4.2	Magnetic Circular Dichroism . . . . .	70
4.4.3	Switching Threshold . . . . .	72
4.5	Explaining Observations in other Work with MCD . . . . .	73
4.5.1	Sweeping over the Surface . . . . .	73
4.5.2	Exposing a Domain Wall . . . . .	74
4.6	Outlook . . . . .	75
4.6.1	Enhanced Control of Magnetic Recording . . . . .	76
4.6.2	Towards the Nanoscale . . . . .	76
4.7	Summary . . . . .	79
<b>5</b>	<b>Element Specific Probing with Visible Light</b>	<b>83</b>
5.1	Introduction . . . . .	84
5.2	Sample Properties . . . . .	85
5.3	Experimental Details . . . . .	85
5.4	Spectroscopic Measurements . . . . .	87
5.4.1	Spectroscopic TR-MOKE . . . . .	89
5.4.2	Transient Ferromagnetic State . . . . .	93

---

5.4.3	Generalization of Element Specific Probing with Visible Light . . .	93
5.4.4	Comparison with Conventional Element Specific Techniques . . .	95
5.5	Fluence Dependent Measurements . . . . .	95
5.5.1	Demagnetization Timescales . . . . .	97
5.5.2	Demagnetization Profiles . . . . .	97
5.5.3	Intersublattice Exchange Interaction . . . . .	98
5.6	Summary . . . . .	100
<b>6</b>	<b>Valorisation: Data Storage with the Speed of Light</b>	<b>103</b>
<b>7</b>	<b>Summary</b>	<b>113</b>
<b>8</b>	<b>Samenvatting</b>	<b>117</b>
	<b>List of Publications</b>	<b>121</b>
	<b>Curriculum Vitae</b>	<b>125</b>



# CHAPTER 1

---

## Introduction

---

*“Quantum mechanics is the key to understanding magnetism. When one enters the first room with this key there are unexpected things beyond, but it is always the master key that unlocks each door.”*

JOHN H. VAN VLECK, NOBEL LECTURE, 1977

## 1.1 Magnetism and Technology

Magnetism has a long and rich history, and has found many applications in today's technologies. Historic studies show that the first reports on magnetism were made already before Christ in the Ancient Chinese and Greek empires where it was observed that certain materials could attract or repel each other. It would take more than a millennium before magnetism had found its first application in the form of a needle pointing along the north-south direction: a compass. Although it would soon be used widely for navigation, it would take almost another millennium and the development of theories such as magneto-statics, electromagnetism, and later quantum mechanics before this phenomenon would be understood in more depth.

Classically, magnets can be considered as small circular electric currents which flow clockwise or anti-clockwise. The former can be defined as "magnetization up" and the latter as "magnetization down". In ferromagnets, these currents exist even in the absence of any external stimulus such as a magnetic field, and the magnetization can generally be just as likely in the "up" or "down" direction. As a consequence, ferromagnets have a non-unique ground state, whereas most other materials are characterized by a well-defined ground states. The direction of the ferromagnetic magnetization points in a direction defined by the history of the magnet. In a sense, this means that a magnet has a memory: its state gives information about its past. It is this fundamental property of magnets which has served as one of the cornerstones of magnetic data storage in current hard drive technology.

In magnetic storage devices the memory consists of logical bits which can be a "0" or a "1", corresponding to the magnetization of domains, i.e., small regions of a magnet, which point either "up" or "down", respectively. The demand for the ever increasing speed of computers has continuously fueled the study of possible routes for ultrafast magnetization reversal, i.e., switching "0" into "1", or vice versa. However, the switching times in current state-of-the-art technologies is almost saturated at a timescale of one nanosecond, which translates to a write/read speed of one gigabit per second [1]. The fundamental limits for switching times are set by the relevant magnetic interactions which define the route through which the magnetization reverses. The typical response times of magnetic phenomena are illustrated in figure 1.1, varying from domain wall motions to the exchange interactions, i.e., the strongest force in magnetism. It can be seen that if switching is driven by domain wall motion, the switching time is typically of the order of tens of nanoseconds up to microseconds. In current hard drive technology, however, magnetization is reversed through precessional motion in an external applied magnetic field, and occurs on a timescale of hundreds of picoseconds up to a nanosecond. From figure 1.1 it is evident that this timescale is not a fundamental limit in magnetism, as the typical timescale at which the exchange interaction affects the magnetic order is of the order of one to a hundred femtoseconds. Instead, the current limit is set by a lack of understanding of ultrafast



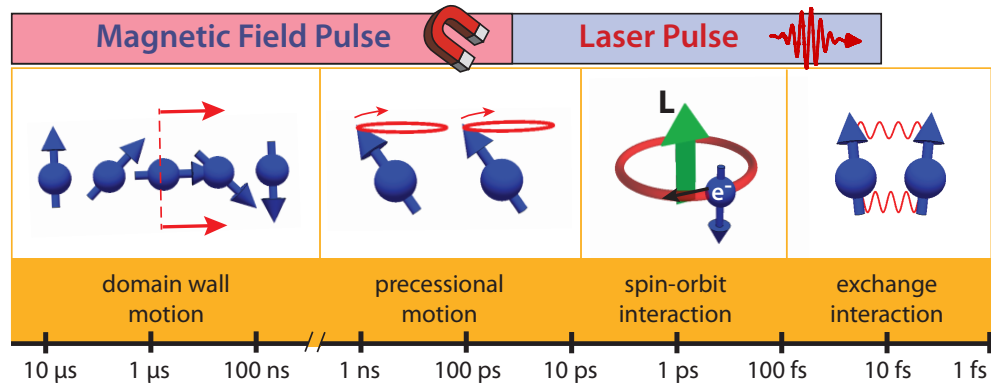


**Figure 1.1:** Typical timescales of magnetic phenomena calculated from  $t \approx h/E$ , where  $h$  is Planck’s constant and  $E$  is the typical energy of the magnetic interaction [4], compared with achievable time duration of magnetic and electromagnetic stimuli using conventional devices.

mechanisms in magnetic materials at (sub)picosecond timescales.

Currently, magnetism on the timescale of “thermal equilibrium”, i.e., the timescale at which the temperature of the magnet is well-defined, is understood and described well [2–4]. However, when the stimulus becomes shorter than the specific time at which thermal equilibrium is reached (typically of the order of picoseconds in metals), the magnet can get into a highly excited state at which the traditional laws of magnetism do not longer hold. There is a large gap in the physical understanding of magnetism and magnetic interactions at these short timescales. One of the fastest stimuli available are ultrashort laser pulses which, as can be seen from figure 1.1, can be as short as tens of femtoseconds with commercially available lasers. At these timescales, many novel and counter-intuitive magnetic phenomena have been discovered in the past 15 years [5–20]. Because of conservation of angular momentum, a change of magnetization must be accompanied with a flow of angular momentum from the magnetic system to another reservoir. It is this flow of angular momentum at the ultrashort timescale which is currently an open issue and a topic of intense discussion and speculation: through which reservoirs does angular momentum flow, and at which timescales? Can we control this flow at the (sub)picosecond timescale? These fundamental challenges, partly arising from the demands of the data storage industry, form the main motivation of the work presented here.

In the following, a brief explanation of magnetization dynamics and overview of previous work is given. The introductory chapter is concluded with today’s challenges in this field of research, the main contribution of this thesis, and its outline.

## 1.2 Precessional Motion

Magnetization dynamics is governed by the interaction of a magnetic field with the magnetic moment. The magnetic moment  $m$  consists of the spin moment (S) and orbital moment (L), which are generally strongly coupled due to the spin-orbit interaction, and give rise to a net angular momentum  $\mathbf{J}=\mathbf{L}+\mathbf{S}$ . The magnetic moment is often expressed in the angular momentum through  $\mathbf{m} = \gamma\mathbf{J}$ , where  $\gamma$  is the gyromagnetic ratio and is material dependent. An external magnetic field  $\mathbf{H}_{\text{eff}}$  exerts a torque on the system which induces a precessional motion of the magnetic moment around the magnetic field. This motion is given by  $\frac{d\mathbf{m}}{dt} = \gamma\mathbf{m} \times \mathbf{H}_{\text{ext}}$ . The precession has a frequency of  $\omega = \gamma H_{\text{ext}}$ .

Although this expression is derived for the magnetic moment of an isolated atom, it can be easily generalized to a magnetic medium with many atoms. When the magnetic moments of the atoms are strongly coupled, then all atomic moments rotate similarly and we can replace the atomic magnetic moment  $\mathbf{m}_i$  by a macroscopic magnetization  $\mathbf{M} = \sum_i \mathbf{m}_i/V$ , where  $V$  is the volume. Furthermore, the local magnetic field consists not only of the external magnetic field but also of the contribution of different types of anisotropies, such as shape anisotropy, and magneto-crystalline anisotropy. The contribution of all these fields can be considered as an effective magnetic field  $\mathbf{H}_{\text{eff}}$  which acts on the material. With these macroscopic approximations, the equation of motion of a macroscopic magnetization vector is obtained, which is also known as the Landau-Lifshitz equation in the nondissipative approximation [2]:

$$\frac{d\mathbf{M}}{dt} = \gamma\mathbf{M} \times \mathbf{H}_{\text{eff}}. \quad (1.1)$$

This equation describes a precessional motion of  $\mathbf{M}$  around the effective magnetic field  $\mathbf{H}_{\text{eff}}$ . It is an accurate description of systems where there is no damping, such as for electrons in vacuum. In most magnetic materials, however, the magnetization will eventually align along the magnetic field and, therefore, the inclusion of a damping term in Eq. 1.1 is essential. The damping term should be perpendicular (i) to the oscillatory motion in order to align  $\mathbf{M}$  along  $\mathbf{H}_{\text{eff}}$ , and (ii) to  $\mathbf{M}$  itself in order to conserve the net magnetic moment. This leads us to the famous phenomenological Landau-Lifshitz-Gilbert equation which describes damped precessional motions [3]:

$$\frac{d\mathbf{M}}{dt} = \gamma\mathbf{M} \times \mathbf{H}_{\text{eff}} + \gamma \frac{\alpha}{M} \mathbf{M} \times (\mathbf{M} \times \mathbf{H}_{\text{eff}}), \quad (1.2)$$

where  $\alpha$  is a dimensionless damping constant which is material dependent. It originates from angular momentum transfer from the magnetic system to another reservoir, such as the lattice, which is not further specified in this equation of motion.

The net magnetization can be reversed with precessional motion through two paths, illustrated in figure 1.2. In magnetic hard-drives, the conventional way to

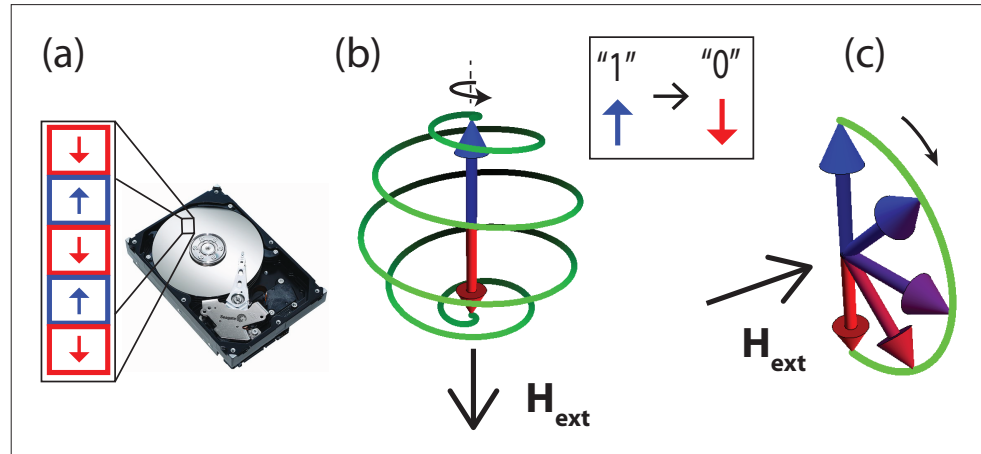


**Figure 1.2:** (a) A harddisk drive consisting of many domains with magnetization either “up” or “down”, corresponding to “1” and “0”, respectively. The reversal time of the “up” state to the “down” state defines the writing speed. (b) Path of precessional reversal with an antiparallel, and (c) perpendicular external magnetic field ( $H_{\text{ext}}$ ).

switch bits is by the application of a magnetic field in an anti-parallel direction compared to the magnetization, as shown in figure 1.2b. The torque on the magnetization together with the damping will induce a damped precessional motion which will eventually result in the reversal of the net magnetization. The reversal time is determined by the damping strength and precession time, and takes typically place on a nanosecond timescale [4, 21].

This can considerably be improved by applying the magnetic field pulse perpendicular to the magnetization, as illustrated in figure 1.2c. If the width corresponds to exactly a half-period of the precession-time, the magnetization will reverse. Using this method, where it is crucial to have an accurate control of the temporal width and the strength of the magnetic field, switching times of down to 100 ps are reported [22–25]. In principle, the switching time can be shortened even further by increasing the strength and decreasing the temporal width of the magnetic field pulse, as the precession frequency is proportional to the magnetic field strength. In practice, however, the maximum applicable field strength in devices is limited to typically 1 Tesla. Furthermore, the minimum width of magnetic field pulses in electronic devices is limited by self-induction to at least tens of ps. Apart from these practical limitations, recent experiments have demonstrated that there might be a fundamental limit for magnetization reversal with an external magnetic field pulse. Using uniquely short and strong magnetic field pulses induced by relativistic electron bunches from the

Stanford Linear Accelerator, it was shown that independent of the field strength, deterministic magnetization reversal does not take place for magnetic field pulses shorter than 2.3 ps [10]. It is therefore of great practical and fundamental interest to find an alternative stimulus to excite magnetism at (sub)picosecond time-scales.

### 1.3 Ultrafast Laser-Induced Magnetization Dynamics

One of the fastest available stimuli are ultrashort laser pulses. Commercial lasers allow time-durations of only a few tens of femtoseconds, while even attosecond pulses have been demonstrated [26–28]. Before these lasers were available, it was believed that optical pulses could affect magnetic order only at timescales on the order of tens of ps. This timescale was obtained from experiments employing optical pulses with a temporal width down to tens of picoseconds [29–32], and it corresponded well with the calculated spin-lattice relaxation time in ferromagnetic Gd [33]. The introduction of femtosecond laser pulses in the nineties allowed the study of magnetization dynamics with much higher temporal resolution.

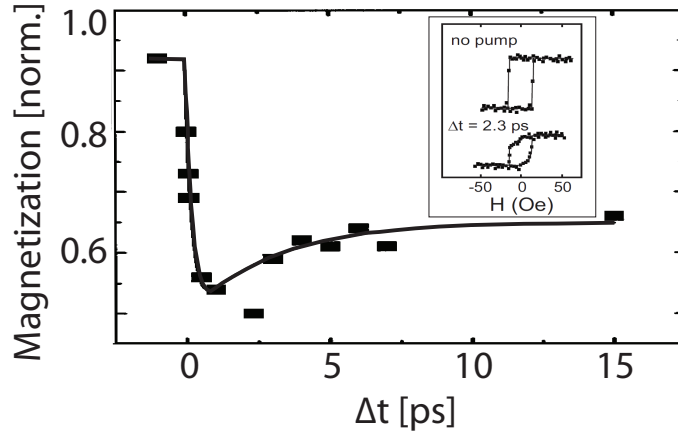


**Figure 1.3:** The first demonstration of ultrafast manipulation of magnetization with light by Beaurepaire *et al.* in 1996 [5]. The magneto-optical contrast of a thin nickel film was measured as a function of time delay with respect to an intense and ultrashort excitation pulse, with a temporal resolution of 60 femtoseconds. These results show an ultrafast drop of the magnetization within a picosecond timescale.

Beaurepaire *et al.* reported in 1996 striking results on laser-induced demagnetization employing 60 fs laser pulses [5]. They demonstrated that the magnetic order of Ni was quenched on a sub-ps timescale when excited with an ultrashort laser-pulse.

The first results of this pioneering work are shown in figure 1.3. It can be seen that the net magnetic moment was quenched to less than 60% of its initial value within one picosecond after excitation. Their work showed that readily available ultrashort electromagnetic pulses could serve as a great alternative to the rather unpractical magnetic field pulses to control magnetic order on sub-picosecond timescales. This opened a new field in magnetism called “femtomagnetism”, partly fueled by the demands from industry for higher speeds, but also driven by curiosity and the fundamental challenge to understand such ultrafast magnetization dynamics. The ultimate goal is to understand, control, and reverse magnetism on the (sub)picosecond time-scales with ultrashort laser pulses.

There were no models which could explain ultrafast magnetization dynamics. The conventional models for magnetization dynamics (based on the Landau-Lifshitz equation) were initially derived for “slow” motion of the magnetization with a conserved magnitude (see Eq. 1.2). Therefore, these models are not and have never supposed to be adequate for ultrafast phenomena. Soon, the experimental results were reproduced by different groups [6–9], and other novel and ultrafast phenomena in magnets were reported such as spin-reorientation [11, 17, 34], modification of magnetic structure [12, 13], and the ultrafast inverse Faraday effect [14–16, 35].

## 1.4 Ultrafast All-Optical Magnetic Recording

Although it was demonstrated that using femtosecond laser pulses one may trigger magnetization dynamics at ultrashort timescales, all these phenomena lead to a small or temporary change of the magnetic order. Full reversal of the magnetization induced by an ultrashort laser pulse remained a fundamental and technological challenge. Further adding to this problem was the fact that the total angular momentum of a laser pulse is far from enough to induce full magnetization reversal through direct transfer of angular momentum from the excitation pulse to the magnetic system [7].

Nevertheless, Stanciu *et al.* demonstrated in 2007 that in GdFeCo, a material originally used for magneto-optical (MO) data storage, a single light pulse can trigger full reversal of the magnetization without the aid of an external magnetic field [18]. The discovery of the so-called “all-optical magnetic recording” or “all optical switching” (AOS) unavoidably revived the discussion about the mechanisms of light-matter interaction in optical control of magnetism. In the following, a brief overview of experiments are given which shaped our understanding of all-optical magnetic recording.

### 1.4.1 Multiple Shot Switching

The first experiments were performed by placing GdFeCo under a MO microscope which could resolve magnetic domains as a black region for magnetization “down” and

a white region for magnetization “up”. The optical excitation pulses were generated by an amplified Ti:Sapphire laser at a wavelength  $\lambda = 800$  nm, a temporal width of typically 60 fs, and a repetition rate of 1000 pulses per second. Initially, GdFeCo was in a multi-domain state. The material was excited by sweeping polarized laser pulses relatively slowly over the surface from left to right. In figure 1.4a it can be seen that right-handed circularly polarized (RC, top), linearly polarized (LP, middle), and left-handed circularly polarized (LC, bottom) laser pulses affect the magnetization of the material in dramatically different ways. First of all, LP pulses create small magnetic domains in “up” and “down” directions. In striking contrast, circularly polarized (CP) pulses deterministically reverse the magnetization of the material. The final direction is fully defined by the light-helicity: RC pulses reverse the magnetization in the “up” direction, whereas LC pulses reverse the magnetization in the “down” direction. This demonstrates unambiguously that optical laser pulses can reverse the magnetization of GdFeCo without any aid of an external magnetic field, and that the final magnetic state can be fully controlled by the helicity of the excitation pulse. We call this phenomenon “helicity dependent all optical switching” (HD-AOS).

### 1.4.2 Single Shot Switching

In order to determine whether a single femtosecond pulse is sufficient to induce AOS, a similar experiment was repeated but this time the sweeping speed was very high so that each subsequent pulse landed on a different spot on the magnetic surface. The results for LC and RC excitation pulses are shown in figure 1.4b. It can be seen that RC laser pulses switch the magnetization of the black region only, and leave the magnetization in the white region unaffected. The exact opposite is observed for LC laser pulses. Thus, single laser pulses can unambiguously switch the magnetization, and the final direction of the magnetic state can be controlled by the helicity of the laser pulse.

Although these experiments showed the intriguing possibility of triggering magnetization reversal with a femtosecond stimulus, the relevant reversal time scales of AOS had yet to be revealed. This was done by Vahaplar *et al.*, who used a technique which allowed MO imaging with femtosecond temporal resolution [19, 36]. An intense CP pulse excited the magnetic system, and a weak LP pulse captured the magnetic state at a well defined time after the excitation. They found that the reversal does not involve precession, but instead has a linear character, proceeding via a strongly nonequilibrium state. In figure 1.4c images of magnetic domains are presented at different delays after excitation by CP pulses [19]. In the first picosecond, pump pulses of both helicities bring the originally magnetized medium into a strongly nonequilibrium and demagnetized state, imaged as a grey region. In the following few tens of picoseconds the magnetization of the excited region relaxes either back to the initial direction or to a reversed direction, depending on the helicity and intensity of the

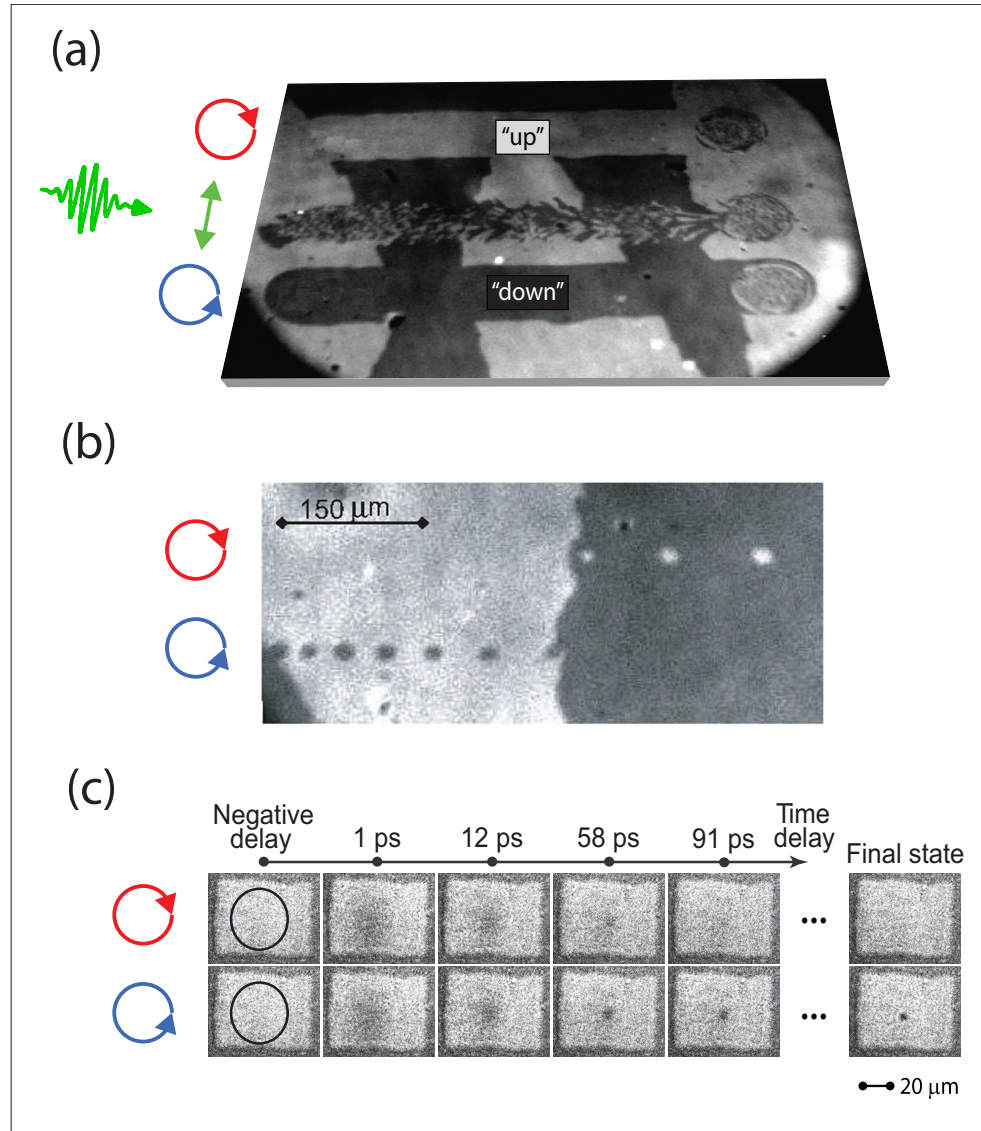


**Figure 1.4:** All-optical magnetic recording studied with MO imaging, where magnetization "up" and "down" are imaged as "white" and "black" regions [18, 19]. (a) Ultrashort and intense excitation pulses at a repetition rate of 1 kHz are swept over the surface of the magnet with different polarizations: RC (top), LP (middle), and LC (bottom). It can be seen that deterministic switching is obtained for circularly polarized light, and that the magnetization can be fully controlled by the helicity of the excitation pulse only. (b) The effect of a single excitation pulse on the magnetization by sweeping the laser pulses at a high speed over the surface. (c) Switching dynamics using time-resolved MO imaging [19]: first there is ultrafast demagnetization (c.q. small MO contrast), leading to full recovery (top) or full reversal (down).

excitation pulse. The switching time was determined to be tens of picosecond, which translates to an unmatched write-read speed of the order of 100 GHz. Moreover, it was demonstrated that HD-AOS occurs only in a certain intensity regime. At higher intensities, both helicities induce deterministic reversal of the magnetization, whereas at lower intensities the magnetization always relaxes back to the initial direction.

### Phenomenological Explanation for AOS

All-optical magnetic recording was believed to originate from the “inverse Faraday effect” (IFE), a phenomenon through which a CP laser pulse can act as a strong effective magnetic field pulse on the spins of the medium, and the direction of this field is defined by the helicity of the light [37, 38]. The existence of such effective magnetic field on fs timescales was demonstrated by experiments on dielectrics [14–16, 35], and served as the main explanation of AOS in GdFeCo [18, 19, 36, 39, 40].

The phenomenological explanation is as follows. The absorption of the optical pulse causes an ultrafast heating of GdFeCo which makes it highly susceptible to the simultaneously generated effective magnetic field pulse. The combination of these two effects leads to magnetization reversal with a CP pulse. The dependence of the direction of the effective magnetic field to the helicity of the light, explains why deterministic magnetization reversal in figure 1.4 is helicity dependent. Simulations under the assumption that there is a 20 T effective magnetic field pulse during exposure due to the IFE, were able to qualitatively explain the switching dynamics for laser-induced magnetization reversal [19].

Although the IFE can explain qualitatively some key features of AOS, a quantitative agreement between models and experiments is still missing. This is partly because the equations describing the IFE were derived in a non-dissipative approximation and thus the microscopical origin of the IFE-field in metallic GdFeCo is still a subject of research. Furthermore, the existence of an “intensity window” discussed in Section 1.4.2, and specifically, the possibility to reverse the magnetization independent of the light helicity, is not explained with the current model for IFE. Hence, there is still a great gap in the microscopic understanding of AOS, and specifically, in the role of light in this phenomenon.

#### 1.4.3 Multisublattice Dynamics

Further adding to the complexity of the magnetization dynamics of GdFeCo at the sub-picosecond timescales, is the fact that the magnetization in this material is built up of two magnetic sublattices. However, so far the experiments were analyzed using a macrospin approximation, where it was assumed that the two sublattices are in equilibrium with each other at any timescale. In contrast to optical techniques, where the collective response of the magnetization can be measured, recent advances in x-ray techniques allow to track magnetization dynamics with element sensitivity and



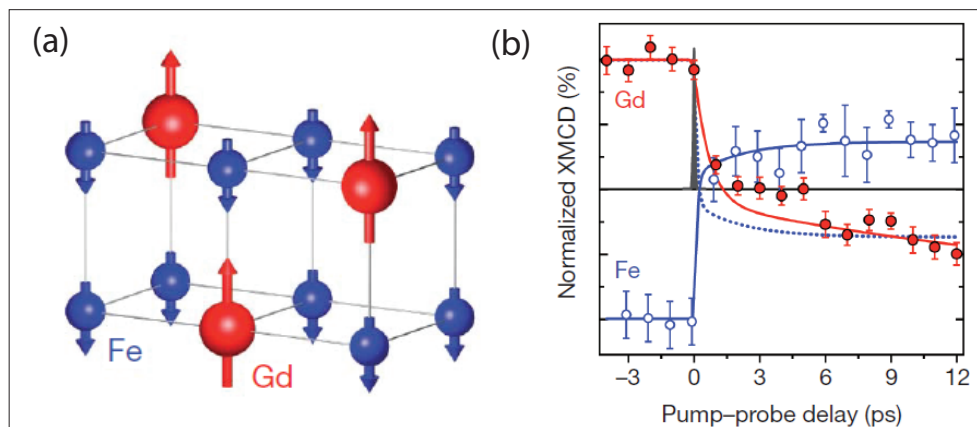


**Figure 1.5:** (a) Illustration of the alignment of the Gd and Fe sublattices in the ground state. (b) Element specific magnetization dynamics of Gd and Fe, when excited with a 60 fs pump pulse with a fluence of  $4.4 \text{ mJ/cm}^2$  [20].

100 fs temporal resolution [41], using x-ray magnetic circular dichroism (XMCD) [42]. The application of such a technique to GdFeCo showed that, in striking contrast to the models, in the first few picoseconds the spins of Gd and Fe are strongly out-of-equilibrium [20]. In fact, their magnetizations evolve against their exchange interaction and turn the originally anti-ferromagnetic material (see figure 1.5a) into a ferromagnetically aligned magnet for about one picosecond. The subsequent relaxation of the system results in a net reversal of the magnetization. These results are presented in figure 1.5b. Recently, it was proposed that this “counter-intuitive” path for magnetization reversal could be explained phenomenologically with ultrafast exchange of angular momentum between the Gd and Fe sublattices [43]. A direct experimental evidence of such ultrafast angular momentum transfer *within* the magnetic system, however, has not been revealed yet. Experimentally, a great limitation is the relatively low signal-to-noise ratio of element-specific x-ray techniques, and the relatively time-consuming measurements. Furthermore, there are only a few fs x-ray sources in the world, strongly limiting the amount of element specific studies which can be performed.

## 1.5 Contribution and Scope of this Thesis

The feasibility of full magnetization reversal with a single ultrashort light pulse has given great practical prospects for ultrafast magnetic recording with possible record-

ing rates exceeding 100 GHz, and approaching the THz regime. At the moment, however, the application of this ultrafast phenomenon in actual devices is hindered by fundamental problems. The ultrafast processes which are involved in AOS are only partly understood. This makes it difficult to optimize this process and use, for example, materials which are economical attractive and have properties which allow maximum reliability. Furthermore, so far AOS has been demonstrated at relatively large domain sizes of at least a few microns, which is one to two orders of magnitude larger than in state-of-the-art magnetic hard drives. It is therefore, apart from the curiosity of scientists to improve our understanding of the nature, of utmost industrial interest to gain a better understanding of the physical processes involved in AOS. This thesis contributes to a better understanding of AOS through an experimental investigation of laser-induced magnetization reversal, in which spectroscopy has played a central role. In particular, the following fundamental issues are addressed:

- What is the role of light and its polarization in all-optical magnetic recording?
- Is it feasible to study the magnetization dynamics of each sublattice individually with visible light?
- Between which reservoirs does angular momentum flow at the picosecond timescale, allowing full magnetization reversal?
- What are the requirements to downsize the area of a switched domain, and is it feasible to reach the nanometer regime?

This thesis is structured as follows. After this introductory chapter, the material properties of the samples under study are explained in chapter 2. First, a general overview of the magnetic properties of rare-earths (RE), and transition metals (TM) is given. Subsequently, the unique properties of RE-TM alloys, which are the most favorable MO recording media, are discussed.

Chapter 3 presents a detailed overview of the experimental techniques which have been used to obtain the results presented in this thesis. Firstly, a brief explanation of the interaction of light with magnetism is given, which allows us to use light as a probe of the magnetic state. Next, different experimental schemes are explained with which static properties of magnetic materials can be measured. In order to measure ultrafast magnetic phenomena we used a stroboscopic pump-probe technique explained in Section 3.3.2. As the heart of all studies in this thesis is the excitation of magnets with light, it is of great importance to have an accurate understanding of the absorption of light in matter. Therefore, absorption and refraction of light in matter is discussed at the end of chapter 3, and a comprehensive explanation of absorption profile calculations in multilayers is given.

Such calculations are used extensively in this work, and form the basis for the quantitative understanding of the role of light in AOS, discussed in chapter 4. We

performed a spectroscopic study of AOS, where the excitation wavelength was varied in the range of 500 to 800 nm. In striking contrast to the phenomenological model described above, we demonstrate that the only role of light in AOS is ultrafast heating of the magnetic system: switching always takes place if the absorbed intensity in GdFeCo reaches a threshold value, when the material is excited with an ultrashort laser pulse. Helicity dependent switching is described as a natural consequence of helicity dependent absorption. It is demonstrated that our new understanding of the role of light in AOS is in qualitative *and* quantitative agreement with all observed phenomena varying from single shot to multiple shot experiments, which were discussed in preceding Sections. Furthermore, it is calculated that relatively small modifications of the magnetic materials may significantly enhance certain properties relevant for magnetic recording. Finally, using a magnetic material with higher anisotropy, we demonstrate the feasibility of reaching the sub-micron scale with AOS with the prospect of achieving bit-sizes of only a few tens of nanometers.

Subsequently, in chapter 5 a new approach is proposed for studying magnetization dynamics with element sensitivity, femtosecond temporal resolution, and a superior signal-to-noise ratio compared to conventional element specific techniques. In particular, we demonstrate through a spectroscopic study of the MO response of a TbFe alloy that the magnetization dynamics of the Tb and Fe sublattices can be studied individually when a probe is used at a wavelength of 500 and 800 nm, respectively. The different wavelength dependencies of the MO responses of the Tb and Fe sublattices originate from the fact that the magnetic moments of the Tb and Fe sublattices are carried by electrons at different energy levels. The presented method for element specific magnetization measurements could eventually play a role not only in the investigation of AOS, but in the study of ultrafast phenomena of coupled magnetic systems in general. Furthermore, the unique advantages of element specific studies with visible light compared to conventional techniques based on x-rays, allowed us to observe novel magnetization dynamics of the antiferromagnetically coupled RE and TM species at the (sub)picosecond timescale. These observations are experimental evidences of an ultrafast angular momentum transfer within the magnetic system, allowing the system to evolve against their exchange interaction and result in a transient state where the sublattices are coupled ferromagnetically. Furthermore, we find that the demagnetization of Tb becomes more efficient in this meta-stable state.

In chapter 6, possible applications of this work in industry are discussed. In particular, a comparison is drawn between the state-of-the-art information technology and our approach to write data with a light pulse. Finally, this thesis is concluded with a summary of the presented work and an outlook.

## References

- [1] R. Wood, *Journal of Magnetism and Magnetic Materials* **321**, 555 (2009).
- [2] L. Landau and E. Lifshitz, *Phys. Z. Sowjetunion* **8**, 153 (1935).
- [3] T. L. Gilbert, *Physical Review* **100**, 1243 (1955).
- [4] J. Stohr and H. Siegmann, *Magnetism, From Fundamentals to Nanoscale Dynamics* (Springer-Verlag, Berlin, 2006).
- [5] E. Beaurepaire, J. C. Merle, A. Daunois, and J. Y. Bigot, *Physical Review Letters* **76**, 4250 (1996).
- [6] J. Hohlfeld, E. Matthias, R. Knorren, and K. H. Bennemann, *Physical Review Letters* **78**, 4861 (1997).
- [7] B. Koopmans, M. van Kampen, J. T. Kohlhepp, and W. J. M. de Jonge, *Physical Review Letters* **85**, 844 (2000).
- [8] L. Guidoni, E. Beaurepaire, and J. Y. Bigot, *Physical Review Letters* **89**, 017401 (2002).
- [9] J. Y. Bigot, L. Guidoni, E. Beaurepaire, and P. N. Saeta, *Physical Review Letters* **93**, 077401 (2004).
- [10] I. Tudosa, C. Stamm, A. B. Kashuba, F. King, H. C. Siegmann, J. Stohr, G. Ju, B. Lu, and D. Weller, *Nature* **428**, 831 (2004).
- [11] A. V. Kimel, A. Kirilyuk, A. Tsvetkov, R. V. Pisarev, and T. Rasing, *Nature* **429**, 850 (2004).
- [12] G. P. Ju, J. Hohlfeld, B. Bergman, R. J. M. van de Veerdonk, O. N. Mryasov, J. Y. Kim, X. W. Wu, D. Weller, and B. Koopmans, *Physical Review Letters* **93**, 197403 (2004).
- [13] J. U. Thiele, M. Buess, and C. H. Back, *Applied Physics Letters* **85**, 2857 (2004).
- [14] A. V. Kimel, A. Kirilyuk, P. A. Usachev, R. V. Pisarev, A. M. Balbashov, and T. Rasing, *Nature* **435**, 655 (2005).
- [15] F. Hansteen, A. Kimel, A. Kirilyuk, and T. Rasing, *Physical Review Letters* **95**, 047402 (2005).
- [16] F. Hansteen, A. Kimel, A. Kirilyuk, and T. Rasing, *Physical Review B* **73**, 014421 (2006).

- 
- [17] M. Vomir, L. H. F. Andrade, L. Guidoni, E. Beaurepaire, and J. Y. Bigot, *Physical Review Letters* **94**, 237601 (2005).
- [18] C. D. Stanciu, F. Hansteen, A. V. Kimel, A. Kirilyuk, A. Tsukamoto, A. Itoh, and T. Rasing, *Physical Review Letters* **99**, 047601 (2007).
- [19] K. Vahaplar, A. M. Kalashnikova, A. V. Kimel, D. Hinzke, U. Nowak, R. Chantrell, A. Tsukamoto, A. Itoh, A. Kirilyuk, and T. Rasing, *Physical Review Letters* **103**, 117201 (2009).
- [20] I. Radu, K. Vahaplar, C. Stamm, T. Kachel, N. Pontius, H. A. Durr, T. A. Ostler, J. Barker, R. F. L. Evans, R. W. Chantrell, et al., *Nature* **472**, 205 (2011).
- [21] W. K. Hiebert, G. E. Ballentine, and M. R. Freeman, *Physical Review B* **65**, 140404 (2002).
- [22] C. H. Back, R. Allenspach, W. Weber, S. S. P. Parkin, D. Weller, E. L. Garwin, and H. C. Siegmann, *Science* **285**, 864 (1999).
- [23] T. Gerrits, H. A. M. van den Berg, J. Hohlfeld, L. Bar, and T. Rasing, *Nature* **418**, 509 (2002).
- [24] H. W. Schumacher, C. Chappert, P. Crozat, R. C. Sousa, P. P. Freitas, J. Militat, J. Fassbender, and B. Hillebrands, *Physical Review Letters* **90**, 017201 (2003).
- [25] H. W. Schumacher, C. Chappert, R. C. Sousa, P. P. Freitas, and J. Militat, *Physical Review Letters* **90**, 017204 (2003).
- [26] M. Hentschel, R. Kienberger, C. Spielmann, G. A. Reider, N. Milosevic, T. Brabec, P. Corkum, U. Heinzmann, M. Drescher, and F. Krausz, *Nature* **414**, 509 (2001).
- [27] T. Popmintchev, M. C. Chen, D. Popmintchev, P. Arpin, S. Brown, S. Alisauskas, G. Andriukaitis, T. Balciunas, O. D. Mucke, A. Pugzlys, et al., *Science* **336**, 1287 (2012).
- [28] P. B. Corkum, N. H. Burnett, and M. Y. Ivanov, *Optics Letters* **19**, 1870 (1994).
- [29] M. Agranat, S. Ashitkov, A. Granovskii, and G. Rukman, *Sov. Phys. JETP* **59**, 804 (1984).
- [30] A. Vaterlaus, D. Guarisco, M. Lutz, M. Aeschlimann, M. Stampanoni, and F. Meier, *Journal of Applied Physics* **67**, 5661 (1990).
- [31] A. Vaterlaus, T. Beutler, and F. Meier, *Physical Review Letters* **67**, 3314 (1991).

- 
- [32] A. Vaterlaus, T. Beutler, and F. Meier, *Journal of Magnetism and Magnetic Materials* **104**, 1693 (1992).
- [33] W. Hubner and K. H. Bennemann, *Physical Review B* **53**, 3422 (1996).
- [34] J. A. de Jong, I. Razdolski, A. M. Kalashnikova, R. V. Pisarev, A. M. Balbashov, A. Kirilyuk, T. Rasing, and A. V. Kimel, *Physical Review Letters* **108**, 157601 (2012).
- [35] T. Satoh, S. J. Cho, R. Iida, T. Shimura, K. Kuroda, H. Ueda, Y. Ueda, B. A. Ivanov, F. Nori, and M. Fiebig, *Physical Review Letters* **105**, 077402 (2010).
- [36] K. Vahaplar, A. M. Kalashnikova, A. V. Kimel, S. Gerlach, D. Hinzke, U. Nowak, R. Chantrell, A. Tsukamoto, A. Itoh, A. Kirilyuk, et al., *Physical Review B* **85**, 104402 (2012).
- [37] J. van der Ziel and P. Pershan, *Physical Review Letters* **15**, 190 (1965).
- [38] P. S. Pershan, J. P. van der Ziel, and L. D. Malmstro, *Physical Review* **143**, 574 (1966).
- [39] A. V. Kimel, A. Kirilyuk, and T. Rasing, *Laser and Photonics Reviews* **1**, 275 (2007).
- [40] A. Kirilyuk, A. V. Kimel, and T. Rasing, *Reviews of Modern Physics* **82**, 2731 (2010).
- [41] C. Stamm, T. Kachel, N. Pontius, R. Mitzner, T. Quast, K. Holldack, S. Khan, C. Lupulescu, E. F. Aziz, M. Wietstruk, et al., *Nature Materials* **6**, 740 (2007).
- [42] B. T. Thole, P. Carra, F. Sette, and G. van der Laan, *Physical Review Letters* **68**, 1943 (1992).
- [43] J. H. Mentink, J. Hellsvik, D. V. Afanasiev, B. A. Ivanov, A. Kirilyuk, A. V. Kimel, O. Eriksson, M. I. Katsnelson, and T. Rasing, *Physical Review Letters* **108**, 057202 (2012).

## CHAPTER 2

---

### Rare-Earth Transition-Metal Alloys

---

*“Gold is for the mistress, silver for the maid, copper for the  
craftsman cunning at his trade. “Good!” said the Baron,  
sitting in his hall, “But Iron - Cold Iron - is master of them  
all.””*

RUDYARD KIPLING, ENGLISH POET, 1910

## 2.1 Introduction

Rare-earth transition-metal (RE-TM) alloys are known for their unique magnetic properties, and are extensively studied since the seventies [1–20]. The introduction of the first commercial hard-disk drive in 1956 with 5 Mb memory, the IBM 305, triggered the search and development of materials which can be used in hard drive devices. This motivated partly the first pioneering studies on RE-TM alloys years later. A group of scientists in IBM discovered in 1972 that RE-TM alloys possess unique magnetic properties which could be very useful for data storage [2]. Amongst these properties is the possibility to have a very high coercive field at room temperature, which is essential for avoiding unwanted switching of magnetic bits. Furthermore, they demonstrated the possibility to read and write magnetic bits with “a remarkably good signal-to-noise ratio” [2]. Their discovery would eventually lead to the first magneto-optical hard disc drives years later. Nowadays, magnetic hard disc drives are widely used and the areal density is approaching 1 Tb/in<sup>2</sup> [16]. Furthermore, RE-TM alloys are also used in numerous other commercial products, such as actuators, microvalves and micropumps [21–23].

RE-TM alloys have also unique properties which make them suitable for ultrafast magnetic recording in the absence of a magnetic field. This phenomenon is called all-optical magnetic recording, and is currently only observed in alloys which consist of RE and TM elements. This chapter provides an overview of this kind of materials and their properties. First, the properties of transition metals and rare-earth metals are discussed in Sections 2.2 and 2.3, respectively. Next, it is explained in Section 2.4 that RE-TM alloys are more versatile than most other magnetic materials, being able to control many key magnetic properties simply by changing the compositions of RE and TM. Finally, in Section 2.5 a brief overview is given of the samples which are studied in this work.

## 2.2 3d Transition Metals

The best known ferromagnetic materials are the 3d transition metals: Fe, Ni, and Co. That is because these materials are the only elements which are ferromagnetic at room temperature. The magnetic moments of these materials are mainly carried by the spins of the conduction electrons in the 3d band. The band width of the 3d electrons is typically 3 eV, and the exchange splitting is of the order of 1 eV. Conduction electrons have a large spatial wavefunction spread over multiple atomic radii. As a consequence of the overlapping wavefunctions of neighboring electrons, the exchange interaction is strong. This property gives rise to *high Curie temperatures* ( $T_C$ ) far above room temperature, which makes these materials of a great practical use. In Table 2.1 the Curie temperatures and the magnetic moments of Fe, Ni, and Co are shown.



**Table 2.1:** The Curie temperatures ( $T_C$ ) [24], spin and orbital moments [25] of Fe, Co, and Ni. Because of the strong exchange interaction, these materials have relatively high Curie temperatures. Furthermore, the magnetic moments are given mainly by the spin moments as the orbital moments are nearly quenched.

material	$T_C$ [K]	spin moment [ $\mu_B$ /atom]	orbital moment [ $\mu_B$ /atom]
Fe	1043	2.25	0.05
Co	1388	1.69	0.08
Ni	631	0.68	0.05

Because the spin-polarized states of 3d TM are in the conduction band and therefore near the Fermi energy, these materials show a strong magneto-optical (MO) response even at low photon energies in the near-infrared regime. A MO response is typically a change of the plane of polarization of incoming light when propagating through a magnetic material. The origin of MO phenomena is explained in detail in Section 3.2. A change in polarization in reflectance is called the Kerr rotation, and in transmittance is called the Faraday rotation. In figure 2.1 the spectral dependencies of the Kerr rotations of Fe [26], Co [27], and Ni [28, 29] are presented. Note that for all three materials the Kerr rotations are relatively large in the near infrared regime, and, in general, tend to decrease towards shorter wavelengths. This MO property of 3d transition metals allows one to probe their magnetic states with infrared light. Furthermore, it is of great importance for the feasibility of element specific probing of ultrafast spin dynamics in the (near-)visible spectral range, discussed in chapter 5.

## 2.3 4f Rare Earth Metals

Another class of magnetic materials are the rare earth (RE) metals. Here, “RE metals” are synonymous to “lanthanides”, covering all elements with atomic number 57 (lanthanum) to 71 (lutetium). The magnetic moments of these materials are mainly carried by the electrons in the localized 4f shell at a few eV below the Fermi level (see Table 2.2), and not the conduction electrons as in TMs. The 4f shell is increasingly filled across the series from La (N=0) to Lu (N=14), while the conduction band remains quite similar. As a consequence, the chemical properties of all rare-earths are fairly identical. This chemical similarity can be of a great advantage as it leads to more or less uniform behavior when the rare-earth metals are combined with other materials. Roughly speaking, one can say that if one member of the group forms an intermetallic compound of a given composition and crystal structure, all other members will act in the same way [25].

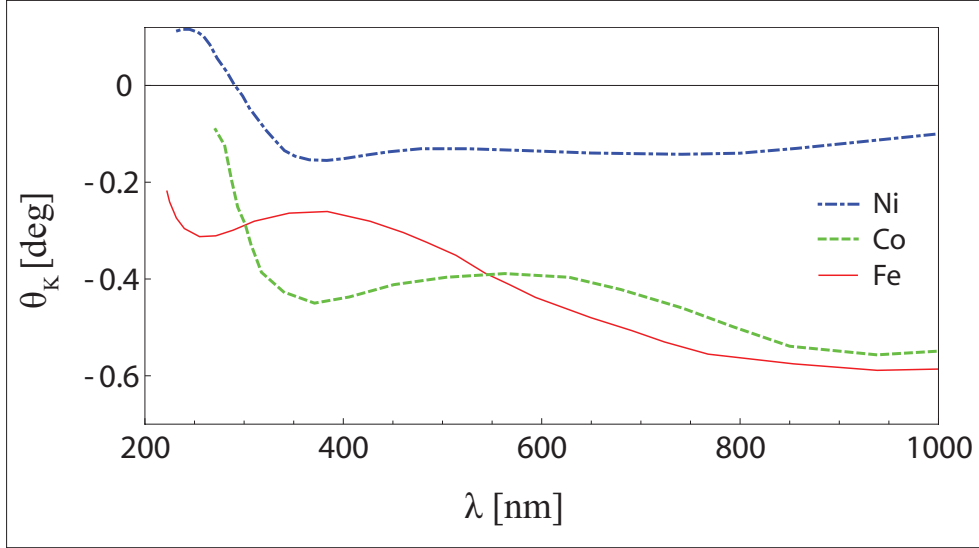


**Figure 2.1:** Spectral dependence of the Kerr rotation of thin films of (bcc) Fe [26], (fcc) Co [27], and (fcc) Ni [28, 29].

Contrary to the chemical properties, the magnetic properties vary markedly. Due to the filling up of the 4f electron shell, the net spin and orbital moments will show a large variation from one element to another. This can be seen from Table 2.2 where the net spin and orbital moments of the RE metals are tabulated. Most of these elements are known for their *very large net magnetic moment*, which is the largest for Ho at  $10.3 \mu_B/\text{atom}$  (where the excess from the integer value is attributed to spin polarization of the 5d6s valence electrons), and for their large spin-orbit coupling. A special element here is Gd, which has an exactly half-filled shell. Therefore, according to Hund's rule, the spin polarization in Gd is maximum (all spins in the 4f shell are aligned parallel), whereas the orbital moment is approximately zero. This leads to a very weak spin-orbit coupling, which leads to a weak magnetocrystalline anisotropy. Therefore, the coercive field of Gd(-alloys) is generally small and of the order of 0.01 T, which is typically two orders of magnitude smaller than for other RE metals.

Due to the localized spin states, the exchange interaction is relatively weak in RE's. This leads to Curie temperatures below room temperature for all compounds (except Gd, which is around room temperature), which has been the main obstacle for their application. The main contribution to the exchange interaction which couples the spins of adjacent atoms comes from the small overlap of the spatial wavefunctions of the 5d and the 4f electrons. This overlap allows the 4f spins to polarize the 5d electrons

**Table 2.2:** Magnetic properties of RE elements. The given energy states are the highest 4f states of RE elements, and are obtained from x-ray photoemission measurements [30–32]. The “S”, “L”, and “J”, are the quantum numbers for the spin, orbital and angular moments in the 4f shell, respectively. The values are for the ground state according to Hund’s rules. The “g-factors” are taken from ref. [24], from which the magnetic moment of the 4f shell can be obtained through  $m = g\mu_B J$ . Note that the elements La (atomic number = 57) and Lu (atomic number = 71), which have an empty and full 4f shell, respectively, have a net magnetic moment of zero and are omitted in this table.

at. n.	RE metal	4f states [eV]	S	L	J	g-factor	$m$ [ $\mu_B$ /atom]
58	Ce	-1	0.5	3	2.5	6/7	2.1
59	Pr	-3.4	1	5	4	4/5	3.2
60	Nd	-4.8	1.5	6	4.5	8/11	3.3
61	Pm	not available	2	6	4	3/5	2.4
62	Sm	-5.1	2.5	5	2.5	2/7	0.8
63	Eu	-1.5	3	3	0	-	0
64	Gd	-7.6	3.5	0	3.5	2	7
65	Tb	-2.4	3	3	6	3/2	9
66	Dy	-4.0	2.5	5	7.5	4/3	10
67	Ho	-4.9	2	6	8	5/4	10
68	Er	-4.7	1.5	6	7.5	6/5	9
69	Tm	-4.5	1	5	6	7/6	7
70	Yb	-1.3	0.5	3	3.5	8/7	4

which assume a small magnetic splitting and magnetic moment. For Gd and Tb, the magnetic moments of the 5d electrons are 0.55 and 0.34  $\mu_B$ /atom, respectively [33]. The 5d electrons can now give rise to a direct exchange contribution, and allowing a long range order of the localized 4f spins.

## 2.4 Amorphous RE-TM Alloys

The class of compounds formed by mixing rare-earths and transition-metals (RE-TM) is of particular interest. The RE and TM have each their unique intrinsic properties giving rise to different advantages and disadvantages, and RE-TM alloys allow to bring the best of two worlds together. On the one hand, one can benefit from the high magnetic moment per atom and the strong single-ion magnetocrystalline anisotropy of the rare-earth, and, on the other hand, from the strong exchange interaction of the 3d transition-metal. The RE-TM alloys thus consist of two magnetic sublattices which are strongly coupled, leading to a common Curie temperature. Because of the

high coupling strength of the TM, the common  $T_C$  of RE-TM alloys is significantly enhanced compared to the  $T_C$  of the RE and can be well above room temperature [14]. Simultaneously, the magnetic properties of the RE metal is retained when mixed with other materials as the 4f electrons are shielded from the environment by the conduction electrons.

### 2.4.1 Light and Heavy RE-TM Alloys

The RE-TM alloys can be classified into two classes: (i) light RE-TM alloys with a less than half-filled 4f shell, and (ii) heavy RE-TM alloys with at least a half-filled 4f shell. The magnetic moments of the former alloys are aligned parallel and therefore these alloys are effectively *ferromagnetic*. Conversely, the magnetic moments of the heavy RE and the TM sublattices are aligned antiparallel and therefore these alloys are effectively *anti-ferromagnetic*.

This can be understood from Hund's rules and the exchange interaction between the 4f and the 3d spins. First of all, Hund's rules state that for less than half-filled shells the orbital and the spin moments couple antiparallel ( $J=L-S$ ), whereas they couple parallel ( $J=L+S$ ) when the shell is at least half-filled [34], as shown in Table 2.2. Since the orbital moment of the light RE is always at least two times larger than the spin moment, the net magnetic moment  $\mathbf{m} \propto -(\mathbf{L}+2\mathbf{S})$  ends up anti-parallel to  $\mathbf{L}$  and *parallel* to  $\mathbf{S}$ . Conversely, in the case of the heavy RE, the magnetic moment is *anti-parallel* to  $\mathbf{L}$  and  $\mathbf{S}$ . The magnetic moment of the TM is almost fully built up by its spin moment, and therefore  $\mathbf{m}$  is *anti-parallel* to  $\mathbf{S}$ . Secondly, the coupling between the 4f spins of the RE and the 3d spins of the TM is mediated through a negative interatomic 4f-5d-3d exchange [35]. As a consequence, in the ground state the spins of the RE are coupled antiparallel to the spins of the TM for all RE-TM alloys. Therefore, the magnetic moments of the RE and the TM align parallel for light RE-TM alloys, and antiparallel for heavy RE-TM alloys.

Along with several other properties, the antiferromagnetic coupling of heavy RE-TM alloys is one of the essential properties allowing all-optical magnetic recording [18, 36–40], and at the same time is the source for a wide variety of other interesting magnetic phenomena [13, 17, 34]. This is one of the reasons why in this thesis heavy RE-TM alloys have been studied.

### 2.4.2 Magnetic Properties of Heavy RE-TM Alloys

The heavy RE-TM amorphous alloys consist of two magnetic sublattices which are anti-ferromagnetically aligned. In general, the two sublattices have different magnitudes of magnetic moments and, therefore, the magnetic moments of the two sublattices do not completely cancel each other. Such antiferromagnetically coupled materials with a net magnetic moment are called "ferrimagnets". Because of the different

strength of the exchange interaction of each sublattice, the temperature dependencies of the magnetic moments of the RE and the TM are different. In general, the net magnetic moment of the RE elements is large at low temperatures but decreases rapidly as a function of temperature, while the net magnetic moment of the TM is relatively small at low temperatures and decreases slowly with temperature. Due to the strong coupling of the two sublattices, however, they have a common  $T_C$ . The Curie temperature of RE-TM alloys is typically 500-700 K [12]. At this temperature, the material undergoes a transition from ferrimagnetic to paramagnetic. These temperature dependencies are illustrated in figure 2.2a.

The different temperature dependencies of  $\mathbf{M}_{\text{RE}}$  and  $\mathbf{M}_{\text{TM}}$  may, at a certain temperature, lead to a state at which the magnitude of the magnetic moments of the two sublattices are equivalent, i.e.,

$$\mathbf{M}_{\text{net}}(T_M) = \mathbf{M}_{\text{RE}}(T_M) + \mathbf{M}_{\text{TM}}(T_M) = 0. \quad (2.1)$$

The temperature at which this condition is met is called the *magnetization compensation temperature*  $T_M$ . Below  $T_M$ , the net magnetic moment of the system points along  $\mathbf{M}_{\text{RE}}$ , while above  $T_M$  the net magnetic moment points along  $\mathbf{M}_{\text{TM}}$ . Nevertheless, the difference in the temperature dependencies of the magnetic moments of the RE and TM are typically small, and results in a small net magnetization at any temperature for the composition ranges at which a  $T_M$  exists. The demagnetizing field, which tends to pull the magnetization in-plane, is therefore very weak in such compositions. The uniaxial anisotropy [25], tending to pull the magnetization out-of-plane, becomes dominant. Therefore, RE-TM alloys of which the net magnetic moment is close to zero exhibit an out-of-plane anisotropy and have almost perfectly square magnetization loops.

Furthermore, the coercive field  $H_C$ , i.e., the field strength to reverse the magnetization, diverges near  $T_M$ . The strength of the coercive field is given by  $H_C \propto K_u/M_{\text{sat}}$  [24], where  $K_u$  is the magnetic anisotropy which is only weakly temperature dependent near  $T_M$  while the saturation magnetization  $M_{\text{sat}}$  is strongly reduced around  $T_M$ . This behavior can be understood from the consideration of the energy of the system:  $E \propto \mathbf{M}_{\text{sat}} \cdot \mathbf{H}$ . The smaller  $M_{\text{sat}}$  the larger the required field in order to overcome the same energy barrier. Therefore, near  $T_M$  a very large field is needed to achieve a moderate energy gain for parallel alignment. In the limit of  $M_{\text{sat}}$  to zero at  $T=T_M$ , there is no magnetization to be reversed and therefore the coercive field diverges.

Thus, an important magnetic property of RE-TM alloys is the value of  $T_M$ . First of all, this value is crucial for magnetic recording. By tuning  $T_M$  close to room-temperature, the large coercive field protects a magnetic bit from unwanted reversal due to stray fields. The magnetic bit can be reversed by simultaneously heating the material close to  $T_C$  at which the coercive field is very small, and applying a moderate field antiparallel to the magnetization [11, 13, 16, 41]. Furthermore, there is evidence that the magnetization compensation temperature plays an important

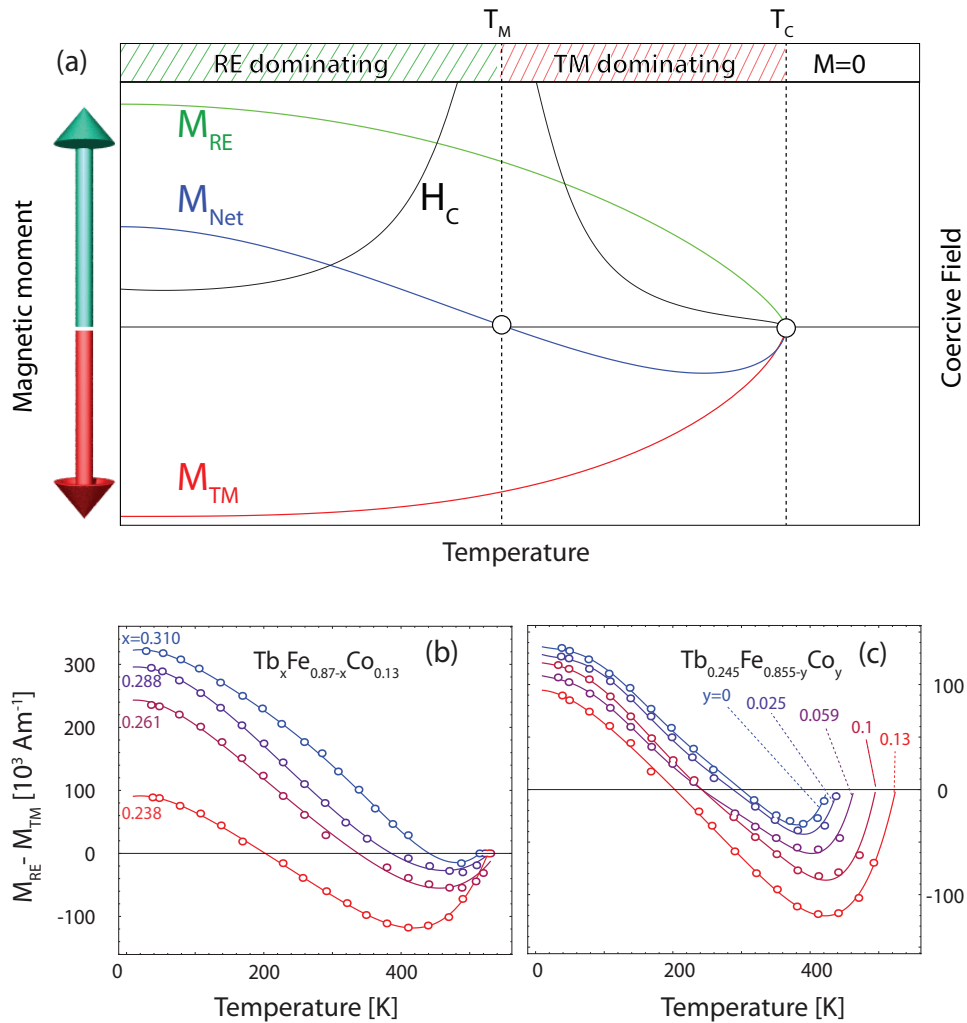


**Figure 2.2:** (a) Illustration of the temperature dependencies of the  $M_{RE}$  (top),  $M_{TM}$  (bottom), and  $M_{net}=M_{RE}-M_{TM}$ . The temperature at which the sublattices completely cancel out each others magnetization is defined as the *magnetization compensation temperature*  $T_M$ . The thin solid line represents the coercive field  $H_C$ , which diverges near  $T_M$  because  $H_C \propto 1/M_{sat}$ . (b,c) The net saturation magnetization of TbFeCo plotted against the temperature. (b) The Tb content  $x$  is varied from 23.8% to 31.0%, whereas the Co content is fixed at 13%. (c) The Tb content is nearly fixed around 24.5% while the Co content  $y$  is varied from 0% to 13%. These experimental data are adapted from ref. [12].

role in ultrafast magnetization reversal [13, 36, 42]. Therefore, the possibility to tune and alter  $T_M$  is of great importance. The facts that RE and TM alloys mix very well, and that their concentrations can be controlled with high accuracy, give a relatively easy and powerful method to control  $T_M$ . As already explained in this Section, the magnetization temperature dependencies of the RE and TM sublattices are different due to the different strength of their exchange coupling. The RE material is characterized by a weaker coupling and therefore the magnetic moment of the RE sublattice drops faster with temperature than the one of the TM. As a consequence,  $T_M$  can be controlled by varying the concentration of the RE in the RE-TM alloys. In general,  $T_M$  is enhanced by increasing the concentration of the RE metal [3, 4, 6, 8, 9, 12]. This is shown in figure 2.2b where the net saturation magnetization of a TbFeCo system was measured as a function the temperature for various Tb concentrations and at a fixed Co content of 13% [12]. It is clear from this figure that a small change of the Tb content has a significant influence on  $T_M$ . In these measurements,  $T_M$  is increased by 200 K when the Tb content is increased from approximately 24% to 31%.

Furthermore, the Curie temperature of these alloys can be enhanced by the addition of Co. Cobalt is characterized by its strong exchange, even compared to other TMs such as Fe and Ni. Therefore, the  $T_C$  of RE-TM alloys can be controlled by the Co content. In figure 2.2c the magnetization curves are shown for different TbFeCo alloys. These alloys have a nearly fixed Tb content of 23.8 – 24.7%, whereas the contents of Fe and Co are varied. It can be seen that  $T_C$  can be increased by nearly 100 K by replacing 13% of Fe with Co.

### 2.4.3 Magnetic Structure: Sperrimagnetism

Collinear arrangements of magnetic moments lead to the familiar forms of magnetic order like ferromagnetism, antiferromagnetism and ferrimagnetism. This is often the case for nicely arranged atoms in crystalline structures. In addition to these familiar types of magnetic order, non-collinear structures occur in amorphous alloys. The presence of chemical and structural disorder in amorphous materials produces an inequivalence of sites that leads to a distribution (i) in magnitude of magnetic moments, (ii) in exchange interactions and (iii) induces large randomly varying electrostatic fields and magnetocrystalline anisotropies [1, 14]. These structures involve a competing random anisotropy and exchange interaction. The exchange interaction favors collinear alignment of the magnetic moments, whereas the local anisotropy aligns the magnetic moments along the locally varying crystalline field axis. When the local anisotropies are negligible as compared to the exchange interactions, there will be a collinear alignment. Specifically, the heavy RE-TM alloys then show a ferrimagnetic alignment consisting of two antiparallel and collinear magnetic sublattices. In general, this is the case for GdCo amorphous films [7, 14].

Conversely, when the local anisotropy is not negligible compared to the exchange

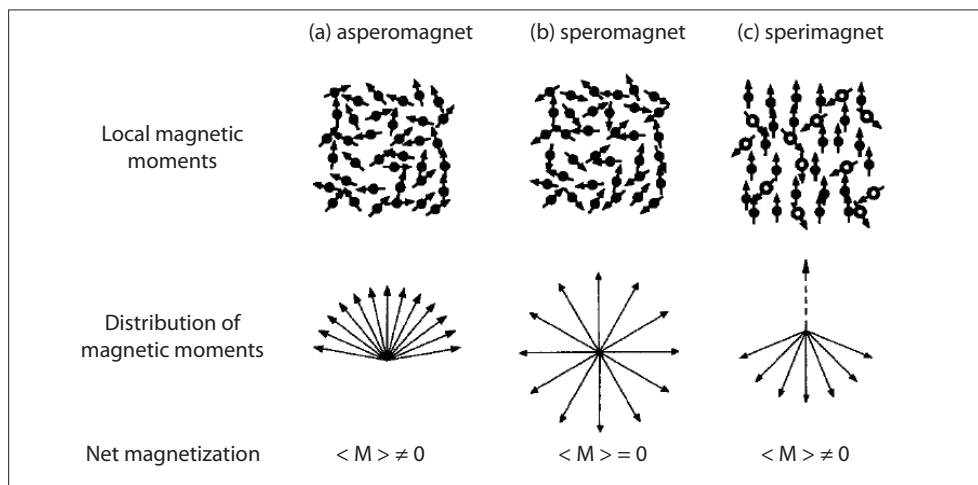


**Figure 2.3:** Non-collinear magnetic structures in amorphous materials [5, 12]: (a) asperomagnetic, (b) speromagnetic, and (c) sperimagnetic. The net magnetization of the system is zero only for speromagnets, in analogy with antiferromagnets. Asperomagnets and sperimagnets are analogous to ferromagnets and ferrimagnets, respectively, with the difference that for the former structures the magnetic moments at each site are not fully collinear but are randomly distributed over a cone.

interaction of a magnetic sublattice, there will be a quasi-random distribution of the magnetic moments due to the locally varying anisotropy. Although the net magnetic moments of the two sublattices are aligned collinearly, the magnetic moment of each site points in a random direction within a cone (see 2.3c). Such non-collinear antiparallel alignment is called “sperimagnetism”, where the prefix “speri” is Greek for “scatter” [1]. Most heavy RE-TM alloys have a sperimagnetic alignment. Usually, both the RE and TM sublattices have locally varying magnetization vectors. Gd and Co, however, are the two exceptions. Thus, GdFe is characterized by one collinear magnetic sublattice (Gd), and one sublattice of which the direction of the magnetic moment varies (Fe). Such magnetic alignment is illustrated in figure 2.3c. In a TbFe alloy, both magnetic moments point locally in a random direction within a cone. In general, the addition of Co improves the alignment of both magnetic sublattices to a more collinear alignment. Therefore, RE-TM alloys are often doped with Co.

Apart from sperimagnets, there are also speromagnets (randomly aligned antiferromagnets) and asperomagnets (randomly aligned ferromagnets) [5, 12]. These non-collinear magnetic structures are illustrated in figure 2.3.

Strictly speaking, ferrimagnets are defined as materials which (i) consist of at least



two magnetic sublattices which are anti-ferromagnetically coupled, (ii) the magnetic moments are collinearly aligned, and (iii) have a net magnetic moment at  $T \neq T_M$ . In literature, however, the second requirement is often omitted, which makes sperimagnets a subclass of ferrimagnets. This broader definition is especially useful if the random nature of the spin distribution is not under study, as in this thesis. Therefore, we make no distinction between structures with locally non-collinear (sperimagnets) and collinear magnetic alignment and call both magnetic structures “ferrimagnets”.

#### 2.4.4 Magneto-Optical Properties

The MO response of a material is given by the MO susceptibility  $K$  which is dependent on the photon-energy. This value is determined by the magnetic transitions of a material, i.e., transitions from or to spin-polarized states with an energy equal to the photon-energy [14]. For a material consisting of a single magnetic sublattice, the Kerr rotation of light with wave vector  $\mathbf{k}$  is given by (see Section 3.2.1)

$$\theta_K(\lambda) = K(\lambda)\mathbf{M} \cdot \mathbf{k}. \quad (2.2)$$

In a material with more than one magnetic sublattices, the Kerr rotation consists of the collective response of all magnetic species. In first order approximation, it is given by:

$$\theta_K(\lambda) = \sum_i K_i(\lambda)\mathbf{M}_i \cdot \mathbf{k}, \quad (2.3)$$

where the summation is over all sublattices.

In 4f RE materials, electronic states carrying most of the magnetic moment are contained at a few eV below  $E_F$ . Therefore,  $K_{RE}$  is typically small in the IR regime [10, 12]. The spins of the TM, on the other hand, are easily accessible as they are carried by electrons in the conduction band near  $E_F$ . For example, at 800 nm the Kerr rotation of a 20 nm thin Fe layer is 300 mdeg, compared to 10 mdeg for a 20 nm Tb film (see chapter 5). Conversely, at higher photon energies, the Kerr rotation of RE materials tends to increase as more magnetic states are accessible. This difference in spectral dependencies of the Kerr rotations of RE and TM, is exploited in chapter 5 in order to investigate distinct magnetization dynamics of RE and TM sublattices.

## 2.5 Materials under Study

In this work we study thin film amorphous GdFeCo and TbFeCo compounds with out-of-plane anisotropy. A small content of Co is added because it enhances the Curie temperatures of these alloys and consequently also the MO response due to its strong exchange interaction, as explained in Section 2.4. The GdFeCo and TbFeCo

samples investigated in this work have Curie temperature of 500-600 K. The structure of these RE-TM alloys is: glass-AlTi(10)-Si<sub>3</sub>N<sub>4</sub>(5)-RE-FeCo(20)-Si<sub>3</sub>N<sub>4</sub>(60) where the number between parentheses indicates the layer thickness in nanometer, as illustrated in figure 2.4a. The metallic magnetic films are protected from oxidization by a 60 nm thick SiN capping layer. This layer is highly transparent in the optical and near infrared regime. Furthermore, below the magnetic film there is a thin AlTi layer which serves as a mirror in order to enhance the MO response of this material. In this way, the transmitted beam from the RE-FeCo layer is partly reflected from the AlTi layer due to its strong optical contrast with the SiN layer on top of it. The reflected beam goes again through the magnetic film and enhances both the reflectivity and the Kerr rotation of the material. These samples are grown on top of a 0.3 mm thick glass substrate. The fact that the substrate is transparent gives extra freedom in our measurements, as it allows to pump or probe the materials from either side of the sample.

### 2.5.1 Growth

Our films are grown by our close collaborators dr. A. Tsukamoto and prof. A. Itoh from the Nihon University, Japan. The films are deposited by magnetron sputtering. A gas is ionized and accelerated through a potential difference to the target material, where it sputters atoms of the target material which move to the substrate. This process is illustrated in figure 2.4b. The film properties (e.g., density, homogeneity, lattice structure, and magnetic properties) strongly depend on the deposition conditions such the inert gas, the pressure of the gas, and voltage over the target material and the shield. These conditions are optimized for each layer separately and are computer controlled, which makes our films highly reproducible. Furthermore, the homogeneity of the deposition is optimized to more than 99% over 15mm×15mm, which is typically the sample dimension.

### 2.5.2 GdFeCo

GdFeCo alloys belong to a unique class of RE-TM alloys with intriguing magnetic properties. First of all, Gd has an exactly half-filled 4f shell, and, therefore, it has a maximum spin moment and no orbital moment (see Table 2.2). This leads to a very weak spin-orbit coupling, and therefore only a small field is needed to saturate the magnetization ( $\mu_0 H_C \approx 0.01 - 0.1 T$ ). This is very convenient when performing experiments as one can easily apply external magnetic fields higher than this coercive field, which is a requirement for performing stroboscopic measurements (see Section 3.3). We have studied samples with a varying Gd content  $x$ : 22%, 24%, and 26%. The cobalt content is always low and fixed to approximately 9%. The magnetization compensation temperatures  $T_M$  of these alloys are deduced from temperature-dependent measurements of the coercive fields  $\mu_0 H_C$  [43]. These measurements are

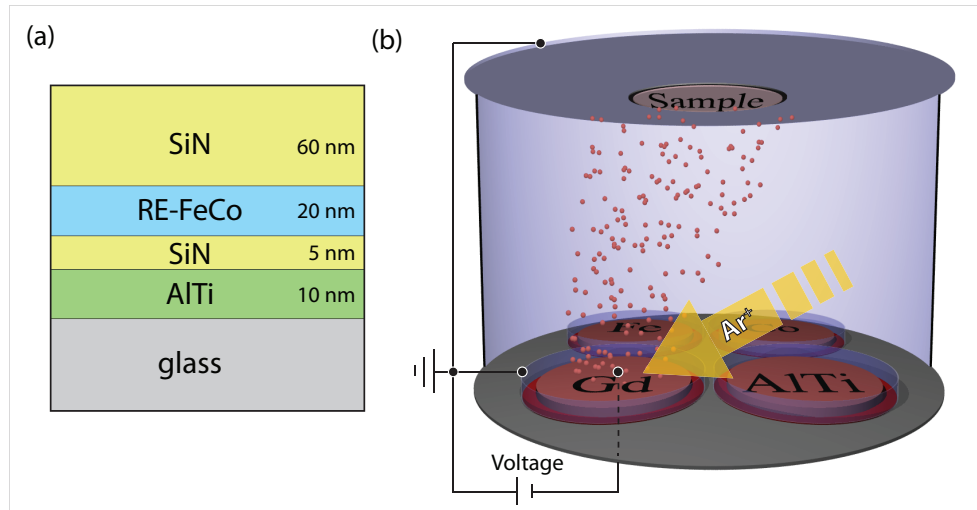


**Figure 2.4:** (a) Schematic view of the multilayer structure of our samples, consisting of a 60 nm thick SiN capping layer to prevent oxidation of the 20 nm thick RE-FeCo film. The AlTi layer serves as a mirror in order to enhance the magneto-optical effects. (a) Illustration of the sputtering technique to grow our samples. There are multiple target materials which can individually be sputtered with a partly ionized argon gas. Ar atoms are ionized due to the high electric field near the target surface, which is controlled by the application of a DC voltage over the grounded shields and the target. The sputtered atoms attach to the substrate which rotates 60 round-trips per second in order to improve homogeneous growth.

shown in figure 2.5a, b. It can be seen that  $T_M$  is strongly dependent on the Gd content.

### 2.5.3 TbFeCo

Another RE-TM alloy which is studied in this thesis is  $Tb_xFe_{0.91-x}Co_{0.09}$ . The Tb content  $x$  varies from 14% to 22%. In many ways TbFeCo films are similar to GdFeCo films. The atomic number of Tb is one higher than Gd, and, therefore, Tb has an extra electron in the 4f shell compared to Gd. The conduction band of both elements are almost identical, which makes them chemically almost identical. This means that Tb mixes the same way with FeCo as Gd. Both have an out-of-plane anisotropy which gives rise to perfect rectangular hysteresis loops, as can be seen from figure 2.6a.

The Kerr rotation of both TbFeCo and GdFeCo samples is in the range of 0.1-1 degrees in the optical range. Furthermore, their Curie temperatures are very similar as they are mainly determined by the TM sublattice.

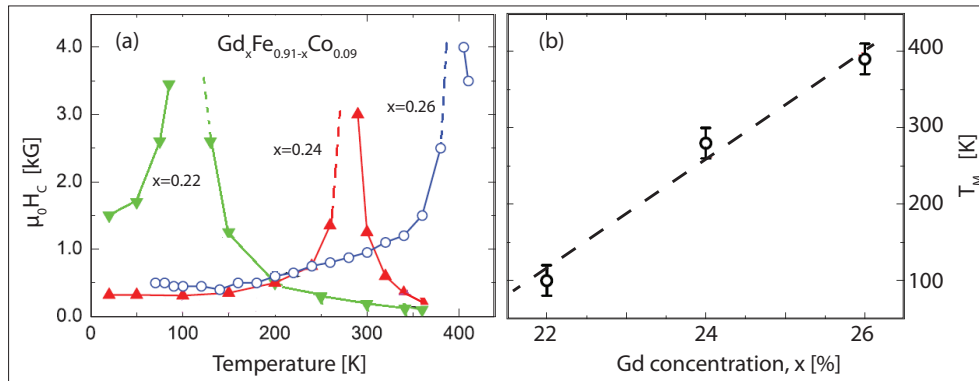


**Figure 2.5:** (a) The temperature dependence of the coercive fields of GdFeCo for three different Gd concentrations. The magnetization compensation temperature  $T_M$  is strongly affected by a small variation of the Gd content, and is plotted in (b). These measurements are from ref. [43].

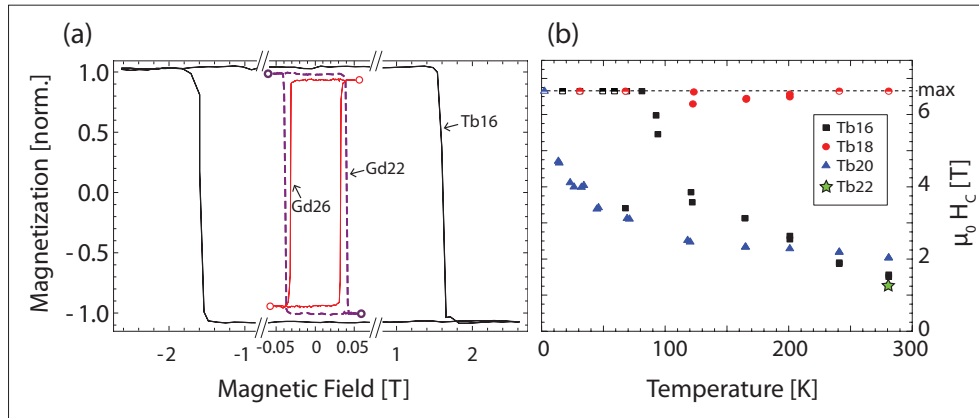


**Figure 2.6:** (a) Normalized hysteresis loops of  $Tb_{16}Fe_{75}Co_9$ ,  $Gd_{22}Fe_{69}Co_9$ , and  $Gd_{26}Fe_{65}Co_9$  at room temperature. The coercive field of  $Tb_{16}$  is 2 orders of magnitude larger than those of  $Gd_{22}$  and  $Gd_{26}$ . Because  $T_M < T_{Room}$  for  $Gd_{26}$  and  $T_M > T_{Room}$  for  $Gd_{22}$  and  $Tb_{16}$ , there is a sign difference in the hysteresis loops. (b) Temperature dependence of the coercive fields of  $Tb_{16}Fe_{75}Co_9$ ,  $Tb_{18}Fe_{73}Co_9$ ,  $Tb_{20}Fe_{71}Co_9$  [44]. The maximum field which could be applied was 7 T, and was not enough to saturate the magnetization of  $Tb_{16}$  and  $Tb_{18}$  at certain temperatures.

The main difference between the two materials is the spin-orbit (SO) coupling. Gd has a very weak SO coupling due to its zero orbital moment in the 4f shell, whereas Tb has a very strong coupling as the additional electron in the 4f shell gives rise to a large orbital moment ( $3 \mu_B/\text{atom}$ ). As a consequence, the magnetic anisotropy of Tb is very large compared to Gd. Typically, the coercive field of TbFeCo is two orders of magnitude larger than the one of GdFeCo, as shown in figure 2.6a. This gives unique opportunities to TbFeCo compared to GdFeCo samples. For example, the size of the smallest magnetic domain of a material is limited by the size of the domain wall, which is inversely proportional to the magnetic anisotropy. Thus, in order to achieve a smaller bit size, the anisotropy should be increased. In GdFeCo the size of the domain wall is typically  $1 \mu\text{m}$ , and therefore, a magnetic bit is significantly larger in GdFeCo films compared to sub-100 nm bit sizes in state-of-the-art magnetic hard drive technology. In TbFeCo, however, the strong anisotropy can lead to domain walls smaller than 16 nm [45]. Using this material, we have achieved the smallest bit size in two-dimensional films with all optical magnetic recording, reported so far: the diameter of the smallest switched domain with a 40 fs laser pulse was measured to be smaller than 250 nm [46]. This is discussed in Section 4.6.

In figure 2.6b is shown the temperature dependence of the coercive fields of TbFeCo samples with different Tb content [44]. At certain temperatures, the maximum external magnetic field of 7 T was not enough to saturate the magnetization of Tb16 and Tb18, due to their high anisotropies. At room temperature, Tb16, Tb20, and Tb22 (not shown here) have a coercive field of 1-2 T, and their magnetization compensation temperatures lies below room temperature.

## 2.6 Summary

Summarizing, rare-earth transition-metal alloys are a class of magnetic materials which combine the best of two worlds, leading to unique magnetic properties suitable for all-optical magnetic recording:

- The strong exchange interaction of transition metals, enhances the Curie temperature of RE-TM alloys with the right TM content to far above room temperature.
- The high magnetic moment of the RE is contained within the f-shell and is protected from the environment by the conduction electrons. As a consequence, the RE alloys keep their magnetic properties when mixed with other materials.
- Due to their ferrimagnetic arrangement and different temperature behavior of the sublattices, there exists a magnetization compensation point at which the coercive field diverges.

- The amorphous structure of these films provides a freedom to accurately control the composition of these films with high homogeneity. By varying the composition one can tune key parameters such as the Curie temperature, magnetization compensation temperature, coercive field, in-plane or out-of-plane magnetic anisotropy, and magnitude of magneto-optical effects.
- Although the net magnetic moment can be close to zero around room temperature, there is still a high magneto-optical signal because the sensitivity of light to each sublattice is different. This is one of the reasons why light is an ideal probe to investigate the magnetization (dynamics) of such alloys.
- The RE-TM alloys which are being studied in this work are GdFeCo and TbFeCo. These materials are identical in many ways, but the magnitudes of their magnetic anisotropies are very different. Gd has an exactly half-filled f-shell leading to a maximum spin-polarization and a minimum orbital moment. The weak spin-orbit coupling leads to a low anisotropy and a small coercive field. Conversely, Tb has an additional electron in the 4f shell which has a large orbital moment. This leads to a strong spin-orbit coupling and a coercive field which is typically two orders of magnitude larger compared to Gd.

## References

- [1] J. M. D. Coey and P. W. Readman, *Nature* **246**, 476 (1973).
- [2] P. Chaudhari, J. J. Cuomo, and R. J. Gambino, *Applied Physics Letters* **22**, 337 (1973).
- [3] R. C. Taylor, *Journal of Applied Physics* **47**, 1164 (1976).
- [4] R. C. Taylor and A. Gangulee, *Journal of Applied Physics* **47**, 4666 (1976).
- [5] J. M. D. Coey, *Journal of Applied Physics* **49**, 1646 (1978).
- [6] Y. Mimura, N. Imamura, T. Kobayashi, A. Okada, and Y. Kushiro, *Journal of Applied Physics* **49**, 1208 (1978).
- [7] J. M. D. Coey, *Journal of Applied Physics* **49**, 1646 (1978).
- [8] P. Hansen, C. P. Klages, J. Schuldt, and K. Witter, *Physical Review B* **31**, 5858 (1985).
- [9] S. R. Lee, A. E. Miller, and H. A. Blackstead, *Journal of Applied Physics* **60**, 3982 (1986).
- [10] D. Weller, W. Reim, and P. Schrijner, *Ieee Transactions on Magnetism* **24**, 2554 (1988).
- [11] J. H. Crasemann and P. Hansen, *Thin Solid Films* **175**, 261 (1989).
- [12] P. Hansen, C. Clausen, G. Much, M. Rosenkranz, and K. Witter, *Journal of Applied Physics* **66**, 756 (1989).
- [13] M. Aeschlimann, A. Vaterlaus, M. Lutz, M. Stampanoni, F. Meier, H. C. Siegmann, S. Klahn, and P. Hansen, *Applied Physics Letters* **59**, 2189 (1991).
- [14] P. Hansen, *Handbook of Magnetic Materials*, vol. 6 (Elsevier, 1991).
- [15] E. Quandt, A. Ludwig, J. Betz, K. Mackay, and D. Givord, *Journal of Applied Physics* **81**, 5420 (1997).
- [16] H. F. Hamann, Y. C. Martin, and H. K. Wickramasinghe, *Applied Physics Letters* **84**, 810 (2004).
- [17] X. Jiang, L. Gao, J. Z. Sun, and S. S. P. Parkin, *Physical Review Letters* **97**, 217202 (2006).
- [18] C. D. Stanciu, F. Hansteen, A. V. Kimel, A. Kirilyuk, A. Tsukamoto, A. Itoh, and T. Rasing, *Physical Review Letters* **99**, 047601 (2007).

- [19] C. D. Xu, Z. F. Chen, D. X. Chen, S. M. Zhou, and T. S. Lai, *Applied Physics Letters* **96**, 092514 (2010).
- [20] I. Radu, K. Vahaplar, C. Stamm, T. Kachel, N. Pontius, H. A. Durr, T. A. Ostler, J. Barker, R. F. L. Evans, R. W. Chantrell, et al., *Nature* **472**, 205 (2011).
- [21] E. Quandt, *Journal of Alloys and Compounds* **258**, 126 (1997).
- [22] C. Body, G. Reyne, G. Meunier, E. Quandt, and K. Seemann, *Ieee Transactions on Magnetism* **33**, 2163 (1997).
- [23] E. Quandt and A. Ludwig, *Sensors and Actuators a-Physical* **81**, 275 (2000).
- [24] R. Skomski, *Simple Models of Magnetism* (Oxford University Press Inc., New York, 2008).
- [25] J. Stohr and H. Siegmann, *Magnetism, From Fundamentals to Nanoscale Dynamics* (Springer-Verlag, Berlin, 2006).
- [26] A. Delin, O. Eriksson, B. Johansson, S. Auluck, and J. M. Wills, *Physical Review B* **60**, 14105 (1999).
- [27] D. Weller, G. R. Harp, R. F. C. Farrow, A. Cebollada, and J. Sticht, *Physical Review Letters* **72**, 2097 (1994).
- [28] K. Nakajima, H. Sawada, T. Katayama, and T. Miyazaki, *Physical Review B* **54**, 15950 (1996).
- [29] S. Visnovsky, V. Parizek, M. Nyvlt, P. Kielar, V. Prosser, and R. Krishnan, *Journal of Magnetism and Magnetic Materials* **127**, 135 (1993).
- [30] S. Hufner, F. Schumann, E. Rotenberg, J. Tobin, S. H. Yang, B. S. Mun, S. Morton, J. Schafer, and D. Ehm, *Physical Review B* **63**, 085106 (2001).
- [31] E. Arenholz, E. Navas, K. Starke, L. Baumgarten, and G. Kaindl, *Physical Review B* **51**, 8211 (1995).
- [32] J. K. Lang, Y. Baer, and P. A. Cox, *Journal of Physics F-Metal Physics* **11**, 121 (1981).
- [33] W. C. Koehler, *Journal of Applied Physics* **36**, 1078 (1965).
- [34] M. Mansuripur, *The Physical Principles of Magneto-Optical Recording* (Cambridge University Press, Cambridge, 1995).
- [35] J. A. Fernandez-Baca and W.-Y. Ching, *The Magnetism of Amorphous Metals and Alloys* (World Scientific Publishing Co. Pte. Ltd, Singapore, 1995).



- 
- [36] K. Vahaplar, A. M. Kalashnikova, A. V. Kimel, D. Hinzke, U. Nowak, R. Chantrell, A. Tsukamoto, A. Itoh, A. Kirilyuk, and T. Rasing, *Physical Review Letters* **103**, 117201 (2009).
- [37] T. A. Ostler, J. Barker, R. F. L. Evans, R. W. Chantrell, U. Atxitia, O. Chubykalo-Fesenko, S. El Moussaoui, L. Le Guyader, E. Mengotti, L. J. Heyderman, et al., *Nature Communications* **3**, 666 (2012).
- [38] A. R. Khorsand, M. Savoini, A. Kirilyuk, A. V. Kimel, A. Tsukamoto, A. Itoh, and T. Rasing, *Physical Review Letters* **108**, 127205 (2012).
- [39] R. Medapalli, I. Razdolski, M. Savoini, A. R. Khorsand, A. Kirilyuk, A. V. Kimel, T. Rasing, A. M. Kalashnikova, A. Tsukamoto, and A. Itoh, *Physical Review B* **86**, 054442 (2012).
- [40] M. Savoini, R. Medapalli, B. Koene, A. R. Khorsand, L. Le Guyader, L. Duo, M. Finazzi, A. Tsukamoto, A. Itoh, F. Nolting, et al., *Physical Review B* **86**, 140404 (2012).
- [41] Z. F. Chen, R. X. Gao, Z. X. Wang, C. D. Xu, D. X. Chen, and T. S. Laia, *Journal of Applied Physics* **108**, 023902 (2010).
- [42] C. D. Stanciu, A. Tsukamoto, A. V. Kimel, F. Hansteen, A. Kirilyuk, A. Itoh, and T. Rasing, *Physical Review Letters* **99**, 217204 (2007).
- [43] K. Vahaplar, A. M. Kalashnikova, A. V. Kimel, S. Gerlach, D. Hinzke, U. Nowak, R. Chantrell, A. Tsukamoto, A. Itoh, A. Kirilyuk, et al., *Physical Review B* **85**, 104402 (2012).
- [44] A. Reid, *private communication* (2011).
- [45] M. Savoini, *private communication* (2012).
- [46] M. Finazzi, M. Savoini, A. R. Khorsand, A. Tsukamoto, A. Itoh, L. Duo, A. Kirilyuk, A. Kimel, T. Rasing, and M. Ezawa, submitted (2012).



## CHAPTER 3

---

### Experimental Methods

---

*“Measure what is measurable, and make measurable what is not so.”*

GALILEO GALILEI, 17TH CENTURIE

## 3.1 Introduction

In the past decades many methods have been developed and improved for measuring magnetism. Each technique has its own advantages and disadvantages. Widely used techniques for measuring the global magnetic moment of a material are Vibrating Sample Magnetometry [1], Superconducting Quantum Interference Device [2], and Nuclear Magnetic Resonance spectroscopy [3, 4]. If one is not interested in the magnetic moment of a material but in other magnetic properties such as the coercive field or the Curie temperature, magneto-optical techniques can be utilized as well, employing the Faraday effect [5] or magneto-optical Kerr effect (MOKE) [6]. In order to study local (submicron) magnetic properties, microscopy techniques are used such as Magnetic Force Microscopy [7], Transmission Electron Microscopy [8], Spin Polarized Scanning Tunneling Microscopy [9], and Scanning Near Field (Magneto-)Optical Microscopy [10, 11].

Most of these techniques are only suited for static characterization of a material, and they do not allow to study ultrafast magnetic phenomena. Ultrafast phenomena can be measured with a probe which is ultrashort, i.e., shorter than a picosecond ( $10^{-12}$  s). This means that any technique which relies on, for example, electronic currents is unsuitable for our studies, as electronic currents in electronic devices cannot be made shorter than typically hundreds of ps due to induction and capacitance. Light on the other hand, could be an ideal probe as current state-of-the-art laser sources can easily deliver optical pulses with a duration of only tens of femtoseconds. Furthermore, these devices can deliver laser pulses with high intensity and with reproducible pulses which are necessary requirements for obtaining a high signal-to-noise ratio. Even the feasibility of attosecond laser pulses has been successfully demonstrated [12, 13]. Another important advantage of using light as a probe is the non-destructive nature of low energy photons.

This chapter presents a detailed overview of the experimental techniques which have been used to obtain the results presented in this thesis. Firstly, it is explained how light interacts with magnetism, allowing to use it as a probe of the magnetic state. Furthermore, different experimental schemes are explained with which static properties of magnetic materials can be measured. Subsequently, the stroboscopic pump-probe technique is explained which allows us to measure magnetic phenomena with a temporal resolution of 50 femtosecond. As ultrashort laser pulses are also used as almost instantaneous stimuli of magnetic systems, a good understanding of light-absorption in a material is essential. This is discussed in detail at the end of this chapter.

## 3.2 Measuring Magnetism with Light

Magneto-optics deals with phenomena arising from the interaction between light and magnetically ordered matter. Such interactions can result in various changes in the frequency or the polarization state of light. Most magneto-optical (MO) phenomena are the direct or indirect outcome of the splitting of energy levels in an external magnetic field due to the Zeeman effect [14], and are usually associated with visible light. In general, however, MO effects may be seen in the whole spectral range of electromagnetic radiation. They are often classified into two types: (i) linear MO, and (ii) non-linear MO. Generally, the frequency of the light is changed only due to non-linear MO phenomena, whereas it is not affected in linear MO. In all the experiments presented in this thesis, the detection of the magnetic state is based on linear MO with visible or near-infrared light. Therefore, we focus in the following on linear MO phenomena.

The polarization state of light can change upon interaction with magnetic materials, because of, for example, a differential refraction (magnetic circular birefringence) or absorption (magnetic circular dichroism) of left and right circularly polarized light. Probably the best known MO effect is the “Faraday effect”, discovered by Michael Faraday in 1845 [5]. Its discovery marked the birth of the field of magneto-optics, as it was the first observation of an interaction between light and magnetism. Faraday found that when a piece of lead-borosilicate glass is subjected to a magnetic field, it becomes optically active: the plane of polarization of light passing through the glass is rotated. Historically, this discovery created a lively interest in MO effects. One of the prime fundamental consequences of this discovery was that it prompted to think of light as an electromagnetic entity. Thereby, MO effects played a central role in the development of Maxwell’s theory of electromagnetism [15]. In fact, James Clerk Maxwell regarded Micheal Faraday as the father of his theory of electromagnetism.

The Faraday effect is illustrated in figure 3.1. The rotation is usually in good approximation linear with the thickness of the magnetic material. Thus, the thicker the sample, the larger the Faraday rotation. On the other hand, the total intensity of the transmitted light decreases exponentially with the sample thickness due to light absorption, which is determined by the complex refractive index of the material. For a metallic sample, this means that the thickness should be limited to tens of nanometers for a measurable transmitted intensity. Nevertheless, the optical anisotropy manifests itself also in reflection of light from a magnetic medium. This effect is called the “magneto-optical Kerr effect” (MOKE) after the Scottish physicist John Kerr who discovered this phenomenon 1877 [6]. MOKE allows to study thick opaque materials or thin films on opaque or unpolished substrates.

In the following, magnetic circular birefringence (Faraday Effect, MOKE) and magnetic circular dichroism are explained in more details, in terms of the dielectric tensor of magnetic media.

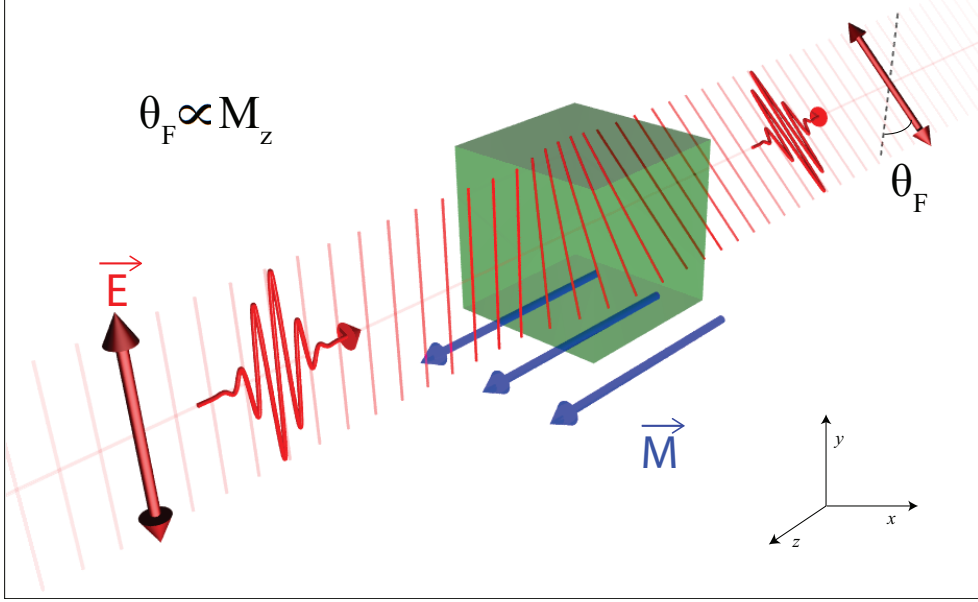


**Figure 3.1:** Illustration of magnetic circular birefringence or the Faraday effect. The plane of the polarization of light is rotated in the magnetized medium. The degree of rotation is a measure of the net out-of-plane magnetic moment of the material.

### 3.2.1 Linear Magneto-Optics

Phenomenologically, linear MO is explained by a difference in refractive index of a magnetic medium for left-handed circularly polarized (LC) and right-handed circularly polarized (RC) light [16, 17]. In other words, the speed and absorption of circularly polarized (CP) light in a magnetic material is dependent on its chirality. For an isotropic medium with an out-of-plane magnetic anisotropy, i.e.,  $M_z \gg M_x, M_y$ , the dielectric tensor is given by [14]

$$\epsilon = \epsilon_0 \begin{pmatrix} 1 & i\tilde{\epsilon}_{xy}(M_z) & 0 \\ -i\tilde{\epsilon}_{xy}(M_z) & 1 & 0 \\ 0 & 0 & 1 \end{pmatrix}, \quad (3.1)$$

where  $\tilde{\epsilon}_{xy} \equiv \epsilon_{xy}/\epsilon_0$ , and in first order approximation  $\tilde{\epsilon}_{xy}(M_z) \propto M_z$ .

Specific polarizations of the light are not changed when it propagates through the magnetic medium along the  $z$ -direction. These polarizations, i.e., the eigenvectors of

the dielectric tensor in Eq. 3.1, are obtained from

$$\epsilon \mathbf{E} = \epsilon_0 \begin{pmatrix} 1 & i\tilde{\epsilon}_{xy}(M_z) & 0 \\ i\tilde{\epsilon}_{yx}(M_z) & 1 & 0 \\ 0 & 0 & 1 \end{pmatrix} \begin{pmatrix} E_x \\ E_y \\ 0 \end{pmatrix} = n^2 \mathbf{E}, \quad (3.2)$$

where  $\mathbf{E} \equiv (E_x, E_y, 0)$  is the initial polarization of the light.

The eigenvectors are readily found to be CP waves, i.e.,  $E_x = \pm iE_y$ , with eigenvalues given by:

$$\begin{vmatrix} \epsilon_0 - n^2 & i\epsilon_{xy} \\ -i\epsilon_{xy} & \epsilon_0 - n^2 \end{vmatrix} = 0 \quad (3.3)$$

$$\Rightarrow n^2 = \epsilon_0 \pm \epsilon_{xy} \quad (3.4)$$

$$\Rightarrow n_{\pm} \approx \sqrt{\epsilon_0} \left( 1 \pm \frac{1}{2} \tilde{\epsilon}_{xy} \right), \quad (3.5)$$

where  $n_+$  and  $n_-$  are the refractive indices for RC and LC light, further noted as  $n_{RC}$  and  $n_{LC}$ , respectively. This means that the polarization of CP light remains unperturbed by the magnetic medium, but that the refractive index it experiences in the medium depends on the chirality of the light. Note that the refractive index is in general a complex number. The asymmetry in the real part of the refractive index, i.e.,  $\text{Re}(n_{RC} - n_{LC})$ , gives rise to the Faraday effect and MOKE, which are both examples of magnetic circular birefringence (MCB). Conversely, the asymmetry in the imaginary part, i.e.,  $\text{Im}(n_{RC} - n_{LC})$ , is the main origin of “magnetic circular dichroism” (MCD).

### 3.2.2 Magnetic Circular Birefringence

A linearly polarized (LP) wave with a given plane of polarization can be represented as a superposition of LC and RC waves with a definite phase difference. As shown above, these two waves propagate with different speeds through a magnetic medium, resulting in a phase difference between the two CP waves. As a consequence, the plane of polarization of LP light rotates in both transmission and reflection. The former is called the Faraday effect, and the latter is called MOKE. The rotation of the plane of polarization of a transmitted LP wave at normal incidence, can be expressed as follows [14]

$$\theta_F = \frac{\omega D}{2c} (n_{LC} - n_{RC}) = K(\lambda) M_z, \quad (3.6)$$

where  $\omega$  and  $c$  are the angular frequency and the speed of light, respectively,  $D$  is the thickness of the material,  $K(\lambda)$  the wavelength dependent magneto-optical

susceptibility and  $M_z$  the out-of-plane magnetization component of the magnetic material.

Although the rotation of the polarization in reflectance arises from the same physical principle as in transmission, its expression in terms of the refractive index and material thickness is more complex. This is mainly because in reflectance, the rotation depends strongly on the absorption depth, and the relative direction of the polarization of the light with respect to the magnetization vector. Nevertheless, both phenomena are in good approximation linearly proportional to the magnetization.

### 3.2.3 Magnetic Circular Dichroism

The asymmetry in the imaginary part of the refractive indices for LC and RC light gives rise to a differential absorption. This MO effect is called “magnetic circular dichroism” or MCD. MCD can be defined with the following expression:

$$\text{MCD} = \frac{A_{LC} - A_{RC}}{0.5(A_{LC} + A_{RC})} \approx \frac{A_{LC} - A_{RC}}{A_{LP}}, \quad (3.7)$$

where  $A_i$  is the fraction of absorbed energy in the magnetic medium for polarization  $i = \text{LC, RC, or LP}$ . In Section 3.4.1 it is explained how to calculate the total absorption  $A_i$  in a material with a given refractive index. Typically, in the visible spectral range MCD is of the order of 1% for 3d magnetic transition metals such as Fe, Co and Ni.

As a consequence of MCD, LP light becomes elliptically polarized. This is because the intensity of LC and RC light is no longer equivalent when the initially LP light propagates through the medium. The degree of ellipticity is proportional to the magnetization. Therefore, both the rotation and the ellipticity of polarized light are a measure of the magnetic moment of a material. In all the work presented here, however, we used the rotation of LP light as a measure of the magnetic moment.

### 3.2.4 Detection Scheme

In order to measure the magnetization hysteresis of our materials, we use the fact that the Faraday rotation changes linearly with the out-of-plane magnetization. As all samples under study have an out-of-plane anisotropy, this means that the Faraday rotation is a measure of the magnetization of our samples. The detection scheme is shown in figure 3.2.

Linearly polarized light with a plane of polarization of  $0^\circ$  propagates through the material, and undergoes a Faraday rotation of  $\theta_F$ . The transmitted light with intensity  $I_0$  goes to a balanced detector which consists of a Wollaston prism and two photodiodes. The prism splits the beam in two beams with planes of polarization at  $+45^\circ$  and  $-45^\circ$ , respectively. The two detectors give a signal  $S_+$  and  $S_-$ , respectively, which scale linearly with the intensity of each of the split beams.



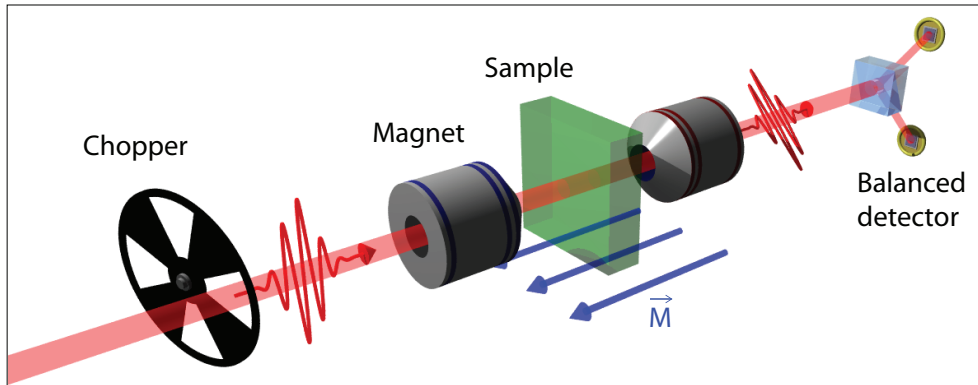


**Figure 3.2:** Experimental setup for Faraday rotation measurements. A LP probe beam is modulated with a chopper at a frequency of typically 500 Hz. It propagates through the magnet which magnetizes the sample parallel or antiparallel to the  $k$ -vector of the light. The probe undergoes a Faraday rotation when propagating through the material. A wollaston prism splits the beam in two orthogonally polarized beams and their intensities are measured with two photodiodes. The difference in the intensity is linear with the total Faraday rotation, as explained in the text.

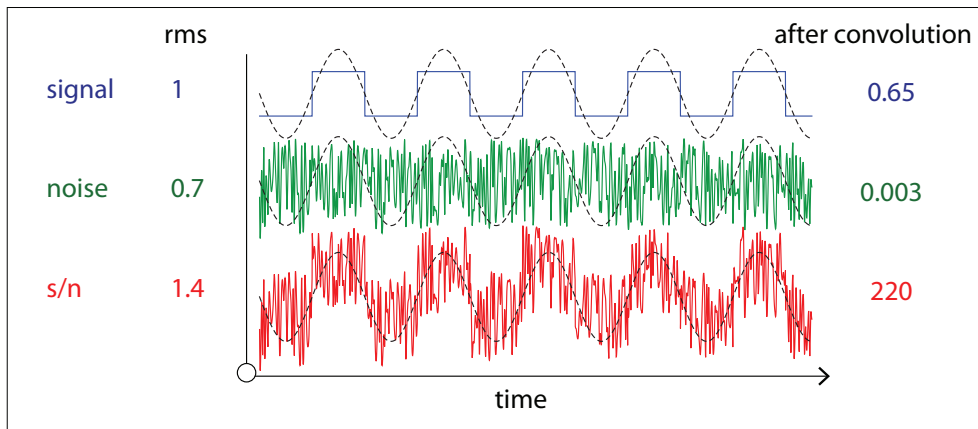


**Figure 3.3:** Illustration of the enhancement of the signal-to-noise (s/n) ratio using probe modulation at frequency  $\Omega$  in combination with a LIA. From top to bottom are shown the actual signal due to Faraday rotation (solid line), the noise, and the difference signal from the photodiodes which is the sum of the noise and the Faraday signal. The root mean square (rms) of these traces are given at left, which result in a s/n ratio of 1.4. This can be significantly enhanced with a LIA, which convolutes the signal to a sine function at frequency  $\Omega$  (dashed line). This process quenches the noise and significantly enhances the s/n ratio (here two orders of magnitude).

The signal of each photodiode can be readily expressed in terms of  $I_0$  and  $\theta_F$ :

$$S_{\pm} \propto I_0 \sin^2(45 \pm \theta_F) \quad (3.8)$$

The difference signal of the two diodes, i.e.,  $\Delta S = S_+ - S_-$ , is linear with the Faraday rotation and the magnetization:

$$\Delta S \propto I_0 (\sin^2(45 + \theta_F) - \sin^2(45 - \theta_F)) \quad (3.9)$$

$$\Delta S \propto I_0 \sin(2\theta_F) \approx 2I_0\theta_F, \quad (3.10)$$

where the latter approximation is accurate for small rotations up to a few degrees. Metallic materials strongly absorb visible light, having an absorption depth of the order of 10 nm. This limits the thickness of our materials to tens of nanometers. The Faraday rotation of magnetic metals is typically 0.01 – 0.1 deg/nm and, thus,  $\theta_F \approx 0.1 - 1$  deg. Therefore, the approximation in Eq. 3.10 is justified for the materials under study.

In practice, one has to deal with noise in the signal. The noise comes mainly from fluctuations in  $I_0$ , which can be due to laser instabilities or stray light from the environment entering the diodes. This noise can be significant and comparable to the difference signal, especially when the Faraday rotation is small as in ferromagnetic metals. In order to resolve such small angles, we use a modulation technique in combination with a lock-in amplifier (LIA).

The probe beam can be modulated with a chopper and, in the case of pulsed lasers, it is also modulated by the repetition rate of the laser. We use a modulation frequency  $\Omega$  of typically 500 Hz (frequency of the chopper) or 1 kHz (repetition rate of our amplified laser). When the chopper is open a signal proportional to the Faraday rotation is measured, and when it is closed, there is no light and therefore the signal is zero. This results in a step function of the actual signal due to the Faraday rotation as illustrated in figure 3.3 (top, solid line). In the middle the noise is illustrated, which is present independent of the chopper and probe light. The detected difference signal from the photodiode is the sum of the signal and the noise, shown in the bottom of figure 3.3.

If we consider the root-mean-square (rms) value of the signal, and compare it with the rms value of the noise, we find a signal-to-noise ratio of  $1 : 0.6 = 1.7$  (see left side of figure 3.3). However, this can be significantly enhanced by exploiting the fact that the actual signal is modulated at  $\Omega$ , whereas the noise is not modulated. This is done with the use of a lock-in amplifier (LIA) which basically convolutes the full difference signal with, for example, a sine function at modulation frequency  $\Omega$  (dashed line in figure 3.3). The actual signal is in phase with the sine function and adds up, whereas the integral over the noise approaches zero, as can be seen from the convoluted values at the right-hand side of figure 3.3. This modulation technique enhances the signal-to-noise ratio significantly, which is in this example by more than 2 orders of magnitude.

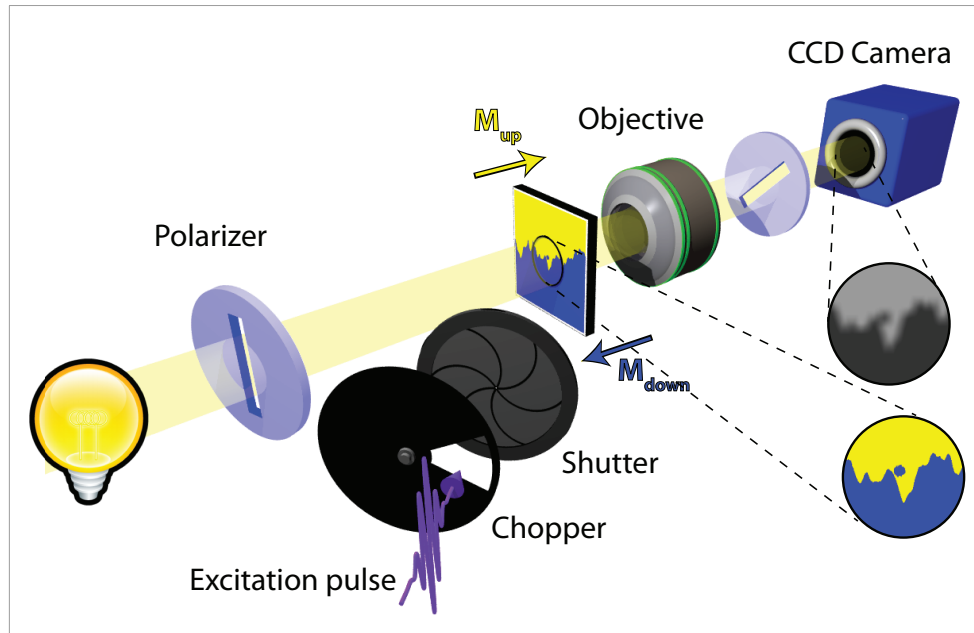


**Figure 3.4:** Magneto-optical imaging setup in combination with femtosecond single shot excitation pulses. Polarized white light undergoes a Faraday rotation, which can be left or right handed depending on the local magnetization. An objective collects the transmitted and rotated light which goes through an analyzer. The transmitted intensity depends on the sign and the magnitude of the Faraday rotation at each specific position. A CCD camera images the intensity of the light, which is a measure of the magnetization of the material, on  $1392 \times 1040$  pixels. The imaged MO image has a nearly diffraction limited resolution of  $1 \mu\text{m}$ .

### 3.2.5 Magneto-Optical Imaging

The method described in Section 3.2.4 is very well suited for measurements of the average magnetic moment of an area of typically  $50 \mu\text{m}$  (typical spot size of the probe). In order to create a two-dimensional map of the magnetic surface of a material to, for example, resolve magnetic domains, one can use a MO imaging setup employing a CCD camera instead of a photodiode, as illustrated in figure 3.4.

Similar to the standard detection scheme of the Faraday rotation explained in Section 3.2.4, MO contrast is imaged with the combined use of a polarized beam and an analyzer. Here, we use a polarized white beam as our probe. The intensity of light which is transmitted through the analyzer depends on both the sign and amplitude

of the Faraday rotation and is therefore a measure of the magnetic state. The CCD camera detects the intensity of the light at each pixel and converts small and high intensities to dark and bright images, respectively. In the scheme in figure 3.4 with incoming plane of polarization at  $0^\circ$  and an analyzer at  $+45^\circ$ , an area which gives rise to a positive rotation (“M-up”) is imaged as a bright area, whereas a negative rotation (“M-down”) is imaged as a dark area. The resolution of the MO image is limited by the diffraction limit  $d$ , given by

$$d \approx 1.21 \frac{\lambda}{2\text{NA}}, \quad (3.11)$$

where NA is the dimensionless numerical aperture of the objective. The given prefactor is for a gaussian beam profile, and is different for other spatial profiles of the probe.

With the CCD camera having 1392x1040 pixels, combined with an objective with 0.4 NA, we are able to image a 1x1 mm surface with almost a diffraction limited resolution of 1  $\mu\text{m}$ . In combination with a pulsed laser system, this technique can be used to study the action of a single excitation pulse to the magnetic state of a material. A chopper reduces the repetition rate of the excitation pulses from 1000 Hz to 10 Hz. Next, we use a shutter which is synchronized to the laser. It can open and close within 100 ms, transmitting a single excitation pulse. This technique is used in Section 4 to study the underlying mechanism of all-optical magnetic recording.

### 3.3 Measuring Ultrafast Magnetization Dynamics

Fundamental studies of ultrafast magnetization dynamics are based on probing the evolution of the magnetization after a sudden perturbation of the magnetic ground state. This can be done by a so-called “pump-probe” technique. The sudden perturbation is triggered by an ultrashort and intense laser pulse, also called the pump pulse. A second and much weaker laser pulse probes the magnetic state. The temporal resolution of the magnetization dynamics is defined by the widths of the pump and probe pulses delivered by the laser system. In the following, a brief overview of the femtosecond laser system employed in this study, and the main properties of the delivered laser pulses is given. Subsequently, the ultrafast MO pump probe technique is explained in detail.

#### 3.3.1 Femtosecond Amplified Laser System

For the ultrafast pump-probe measurements presented in this work, we employ a laser system which can generate ultrashort 55 fs laser pulses at a repetition rate of 1 kHz and with an average energy of roughly 2 mJ/pulse. In order to achieve these

parameters, we use a commercial system of *Spectra-Physics* consisting of five main elements:

- *Millenia Pro*, diode pumped CW laser.
- *Tsunami*, mode-locked Ti:sapphire laser.
- *Empower*, intracavity-doubled, diode-pumped Nd:YLF laser.
- *Spitfire Pro*, Ti:sapphire regenerative amplifier.
- *OPA-800C*, ultrafast optical parametric amplifier.

Our femtosecond laser system is schematically shown in figure 3.5 [18]. The *Millenia Pro* is a diode-pumped continuous wave (CW) laser with neodymium yttrium vanadate (Nd:YVO<sub>4</sub>) as the gain medium. Combined with a lithium triborate crystal (LBO), the *Millenia Pro* generates a laser beam at  $\lambda = 532$  nm with an output power of 5 W. This beam serves as a pump of the Ti:sapphire crystal in the *Tsunami* laser [19]. The excited Ti<sup>3+</sup> ions fluoresce in the range of 600-1000 nm. The *Tsunami* wavelength can be tuned using a prism sequence and a slit. This sequence provides a region in the cavity where the wavelengths are spatially spread, and, by moving the slit, a certain wavelength can be selected. Although the wavelength is tunable from 670-1000 nm, we used a fixed wavelength at  $\lambda = 800 \pm 20$  nm. The typical pulse duration is 50 fs with a repetition rate of 80 MHz and an energy of roughly 1 nJ/pulse.

These pulses are amplified by the *SpitFire Pro* by 6 orders of magnitude [20]. The *SpitFire Pro* is pumped by a 10 W *Empower* laser at a repetition rate of 1 kHz with a pulse duration of typically 100 ns. The heart of the *Empower* system is a rod of neodymium-doped lithium yttrium fluoride (Nd:YLF). This material emits at 1053 nm and is frequency doubled with a LBO crystal to 527 nm, which is absorbed strongly by the Ti:sapphire crystal in the *SpitFire Pro*. Immediately after the excitation of the crystal by a single pump pulse from *Empower*, bringing the system into population inversion, a single seed pulse from the *Tsunami* is selected with two Pockels cells. This single pulse is sent to the excited crystal and is amplified through stimulated emission. A total of twenty round trips result in an amplified pulse from initially 1 nJ/pulse to typically 2 mJ/pulse. In order to avoid damage of the optical elements, the seed pulse is first stretched with the use of gratings prior to amplification, to be recompressed to typically 55 fs with the same gratings after amplification.

Finally, the ultrafast Optical Parametric Amplifier (OPA) allows to vary the output wavelength of the laser from 800 nm to 0.3-3  $\mu\text{m}$  [21]. This is done with the use of a combination of various crystals, depending on the desired output wavelength. During the conversion process, a large part of the pulse energy is lost due to the limited conversion efficiencies of the crystals. The final pulse-energy after the OPA varies from 1-100  $\mu\text{J}$ /pulse, depending on the wavelength.

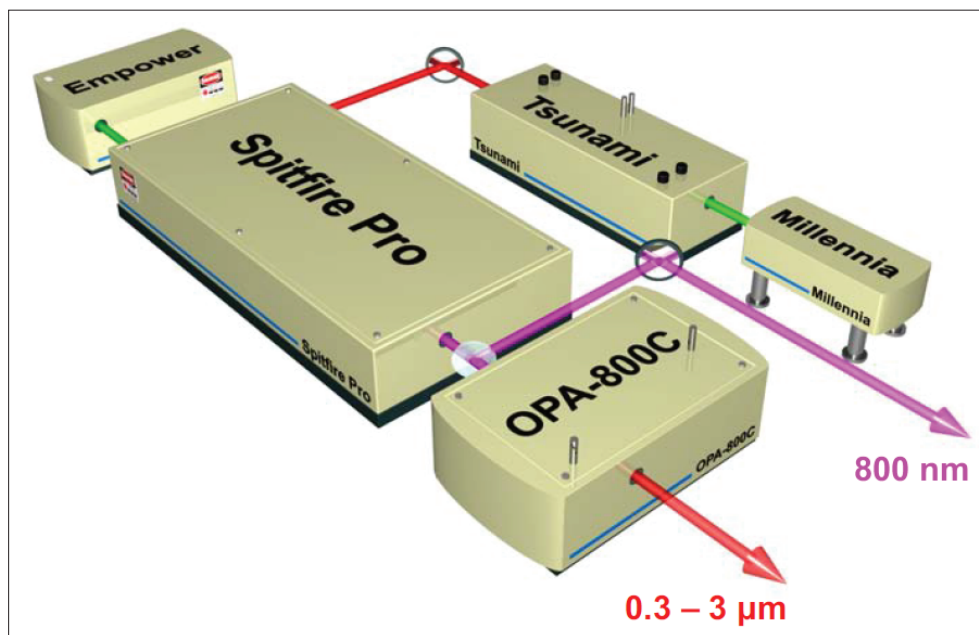


**Figure 3.5:** Sketch of the femtosecond laser system [18], consisting of a Tsunami laser (mode-locked Ti:sapphire) seeded by a Millennia CW laser. This combination gives ultrashort 50 fs laser pulses with  $\lambda = 800$  nm at a repetition rate of 80 MHz. The Spitfire Pro (Regenerative Amplifier) which is seeded by an Empower laser, amplifies the ultrashort pulses to roughly 2 mJ/pulse at a repetition rate of 1 kHz. With the OPA it is possible to change the wavelength of the laser pulses in the range  $\lambda = 0.3\text{-}3$   $\mu\text{m}$ .

### 3.3.2 Ultrafast Magneto-Optical Pump-Probe Setup

With our femtosecond laser system delivering intense and ultrashort pulses, we can ignite ultrafast spin dynamics in magnetic materials. In order to “record” the dynamics induced by a single pump pulse with a fs time resolution, one has to use a clever method to deal with the relatively slow response time of electronic devices such as photodiodes, typically of the order of microseconds. This can be done with a so-called “stroboscopic pump-probe technique” [22]. Instead of trying to track the whole dynamics of a single event, the same event is repeated for many times (here, 1000 times per second). By delaying an ultrashort probe pulse with respect to the pump pulse, one can measure the magnetic state of the material at a certain time delay. The magnetic state can be measured with, for example, the detection scheme employing the Faraday rotation described in Section 3.2.4. Basically, the probe pulse measures

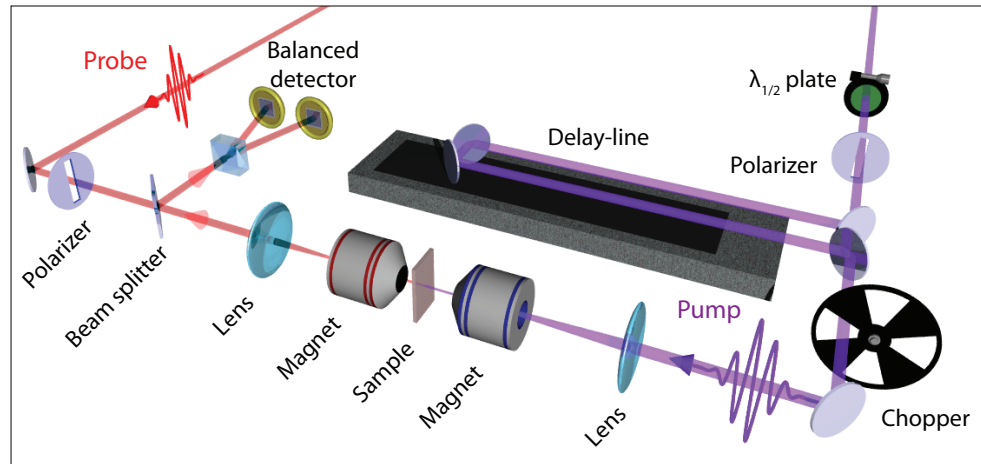


**Figure 3.6:** Sketch of the ultrafast magneto-optical pump-probe setup. The magnetic material is excited by a 50 fs intense pump pulse, which can be delayed with a delay-line. The pump energy is accurately controlled by the sequence of a half-wave plate and a polarizer. The less intense probe pulse arrives at the sample after excitation and undergoes a Kerr rotation upon reflection. Subsequently, a beam splitter directs the probe pulse to a balanced detector, which measures the Kerr rotation of the probe pulse.

the data point  $(t, M(t))$  which captures a single moment in the whole magnetization dynamics. By varying the delay between pump and probe, one can capture the magnetic state at different times after excitation, allowing to record the magnetization dynamics with fs resolution. Note that this technique works only when the sample recovers to the original state after each pump-probe event. This is usually ensured by (i) the application of an external magnetic field which is larger than the coercive of the material, and (ii) a large enough delay between each subsequent pulse (here 1 ms) which gives the system enough time to relax in the external magnetic field. The setup which was used for ultrafast magneto-optical pump probe studies is illustrated in figure 3.6.

The magnetic material is excited by an intense pump pulse, which is taken from the *SpitFire Pro*. The lateral beam diameter on the sample surface is made relatively large, e.g.,  $\approx 300 \mu\text{m}$ . At a delayed time the magnetic state is detected by a much less intense probe pulse ( $I_{\text{probe}}/I_{\text{pump}} < 0.01$ ), taken from the OPA. The lateral beam diameter of the probe beam is made much smaller than the pump spot, e.g.,  $d_{\text{probe}} < 100 \mu\text{m}$ , in order to guarantee homogeneous excitation of the probed area. The time-delay between the pump and probe pulses can be set by delaying (i) the probe or (ii) the pump, employing a delay-line. In practice, the delay line can slightly

affect the beam position on the sample surface. In order to be sure that at any time-delay the same position on the sample is probed, the pump pulse goes through the delay stage and not the probe. Small movements of the pump position on the sample is relatively harmless for the measurements as the lateral diameter of the pump pulse is much larger than the probe pulse.

The probe pulse is first linearly polarized and then focused on the sample surface. The reflected beam is collected by a 50/50 beam splitter which directs the probe to a balanced detector. The difference signal of the balanced detector is a measure of the rotation of the plane of polarization through MOKE, as explained in Section 3.2.4.

The intensity of the pump pulse is accurately controlled by the sequence of a  $\lambda_{1/2}$ -plate and a polarizer. The angle  $\theta$  of the  $\lambda_{1/2}$ -plate, which rotates the plane of polarization by  $2\theta$ , is computer controlled with an accuracy of 0.01 degrees. The pump pulse is delayed with a delay-line with an accuracy of  $0.1 \mu\text{m}$  corresponding to 0.67 fs. It is modulated with a chopper at 500 Hz, in order to optimize the signal-to-noise ratio. Subsequently, the pump beam is focused on the sample and excites the magnetic material, inducing an ultrafast change in the magnetization. Because of the modulated pump-beam, the probed Kerr rotation is also modulated by (i) the Kerr rotation when there is no excitation pulse, to (ii) the Kerr rotation when there is an excitation pulse. By taking the chopper frequency as the reference signal of the LIA, one obtains a signal which is proportional to the difference of signal (i) and signal (ii), i.e., the measured signal is proportional to the *change of the magnetic moment* due to a pump pulse. On the other hand, a signal corresponding to the *absolute magnetic moment* is obtained when the pump, probe, and the reference signal are at the same frequency. In the latter geometry, the sensitivity to the *change* of the magnetization is smaller, and therefore, that geometry should be avoided if there is only a small change of the magnetic moment.

### 3.4 Optical Properties

The total light-absorption in a material can be a crucial quantity if one is, for example, interested in thermal phenomena induced by a laser pulse. On the other hand, the refraction of light plays a major role in non-thermal phenomena. Both absorption and refraction of light are defined by the complex refractive index of a material, which is mainly given by the diagonal part of the permittivity tensor (Eq. 3.1), whereas MO phenomena originate from the off-diagonal components as discussed in Section 3.2. A detailed explanation of light-absorption in thin multilayer films is given in Section 3.4.1. Based on this theory, a code in Wolfram Mathematica [23] was written in order to compute the reflectance, transmittance, and, specifically, the spatial distribution of the deposited photon energy in our multilayered samples. For many materials, the complex refractive indices are well known for a broad spectral range [24, 25]. However, the refractive indices of our magnetic layers consisting of a unique



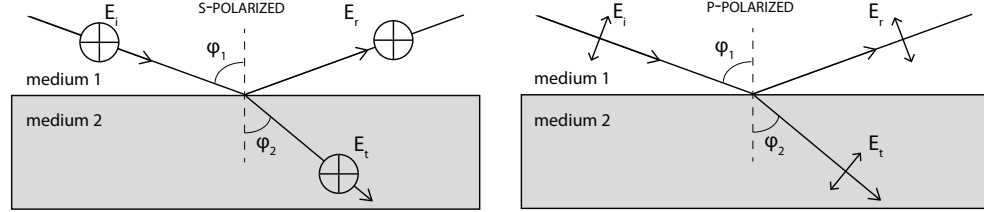


**Figure 3.7:** Reflection and refraction of s- (left) and p- (right) polarized light at an interface between medium 1 and medium 2.  $E_i$ ,  $E_r$  and  $E_t$  are the electric field amplitudes of the incident, reflected and transmitted waves, respectively.

composition of RE-Fe-Co, should be measured by ourselves. For this purpose, we use a “Variable Angle Spectroscopic Ellipsometer” (VASE) described in Section 3.4.2.

### 3.4.1 Optical Response of a Multilayer

#### Fresnel Equations

An electromagnetic plane wave is partly reflected and partly transmitted at each optical interface. An illustration of the reflection and refraction of LP light is shown in figure 3.7. Here, a distinction is made for polarization perpendicular and parallel to the sample normal, defined as s- (from the German word “senkrecht” for perpendicular) and p-polarization, respectively.

$E_i$ ,  $E_r$ , and  $E_t$  are defined as the electric field amplitudes of the incoming, reflected, and transmitted beams, respectively. These values are related to each other by the well-known Fresnel equations. For s- and p-polarized light, respectively, they are:

$$s: r_{1,2} = \frac{E_r}{E_i} = \frac{n_1 \cos \phi_1 - n_2 \cos \phi_2}{n_1 \cos \phi_1 + n_2 \cos \phi_2}, \quad t_{1,2} = \frac{E_t}{E_i} = \frac{2n_1 \cos \phi_1}{n_1 \cos \phi_1 + n_2 \cos \phi_2}, \quad (3.12)$$

$$p: r_{1,2} = \frac{E_r}{E_i} = \frac{n_2 \cos \phi_1 - n_1 \cos \phi_2}{n_2 \cos \phi_1 + n_1 \cos \phi_2}, \quad t_{1,2} = \frac{E_t}{E_i} = \frac{2n_1 \cos \phi_1}{n_1 \cos \phi_2 + n_2 \cos \phi_1}, \quad (3.13)$$

where  $n_i$  denotes the refractive index of medium  $i$ . The angle of the incident beam  $\phi_1$ , and the angle of the refracted beam  $\phi_2$ , are related to each other through Snell’s law:  $\sin \phi_1 / \sin \phi_2 = n_2 / n_1$ . At normal incidence, there is no difference between s- and p-polarization, and the Fresnel equations simplify to

$$r_{1,2} = \frac{n_1 - n_2}{n_1 + n_2}, \quad t_{1,2} = \frac{2n_1}{n_2 + n_1}. \quad (3.14)$$

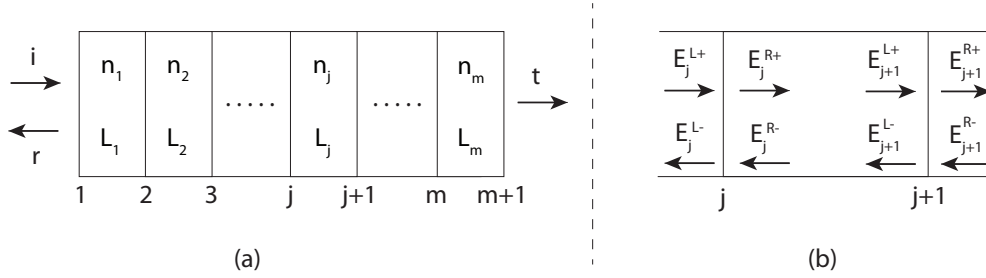


**Figure 3.8:** (a) A sketch of a multilayer with  $m$  layers. The incident, reflected and transmitted electric field amplitudes at an interface are denoted by  $i, r$  and  $t$  respectively. (b) There are four field amplitudes associated with each interface:  $E_j^{L+}, E_j^{R+}, E_j^{L-}, E_j^{R-}$ . The letters R and L stand for the left and the right side of the interface respectively, and the plus and minus signs stand for the direction in which the electromagnetic wave is traveling: to the right or left respectively.

The total reflection  $R$ , and transmission  $T$  of the beam intensity, are given by the square of  $r$  and  $t$ , respectively:

$$R = \frac{|n_1 - n_2|^2}{|n_1 + n_2|^2}, \quad T = \frac{4|n_1|^2}{|n_2 + n_1|^2}. \quad (3.15)$$

### Multiple Reflections

For a multilayer system, involving multiple interfaces, the electric fields at all interfaces can be obtained from a matrix formalism [26, 27]. Consider the multilayer sketched in figure 3.8. The following quantities are defined:  $i, r$  and  $t$  are the amplitudes of the incident, reflected and transmitted electric fields respectively. In a multilayer there are, in general, four electric field amplitudes associated with each interface. These are indicated in figure 3.8b:  $E_j^{L+}$  denotes the amplitude of the electric field that travels in a forward direction (to the right) and is at the left side of the  $j$ th interface,  $E_j^{R+}$  denotes the amplitude of the electric field that travels in a backward direction (to the left) and is at the left side of the  $j$ th interface,  $E_j^{L-}$  denotes the amplitude of the electric field that travels in a forward direction (to the right) and is at the right side of the  $j$ th interface, and  $E_j^{R-}$  denotes the amplitude of the electric field that travels in a backward direction (to the left) and is at the right side of the  $j$ th interface.

The electric field amplitudes at each interface, are related to each other through:

$$E_j^{R+} = t_{(j,j+1)} E_j^{L+} + r_{(j+1,j)} E_j^{R-} \quad (3.16)$$

$$E_j^{L-} = t_{(j+1,j)} E_j^{R-} + r_{(j,j+1)} E_j^{L+}, \quad (3.17)$$

where  $r_{(j,j+1)}$  and  $t_{(j,j+1)}$  stand for the reflection and transmission of the electric field of an electromagnetic-wave traveling from medium  $j$  to medium  $j + 1$ . This can be written as a matrix transformation:

$$\begin{pmatrix} E_j^{L+} \\ E_j^{L-} \end{pmatrix} = \frac{1}{t_{j,j+1}} \begin{pmatrix} 1 & r_{j,1+1} \\ r_{j,j+1} & t_{j+1,j}t_{j,j+1} - r_{j+1,1}r_{j,j+1} \end{pmatrix} \begin{pmatrix} E_j^{R+} \\ E_j^{R-} \end{pmatrix} \quad (3.18)$$

$$\equiv I_j \begin{pmatrix} E_j^{R+} \\ E_j^{R-} \end{pmatrix}, \quad (3.19)$$

where  $I_j$  denotes the “interface matrix” corresponding to the  $j$ th interface.

Moreover, the amplitudes and phases of the electromagnetic (EM) waves change when propagating through a material. The amplitudes  $E_j^{R+}$  and  $E_j^{R-}$  are related to  $E_{j+1}^{L+}$  and  $E_{j+1}^{L-}$  by

$$\begin{pmatrix} E_j^{R+} \\ E_j^{R-} \end{pmatrix} = \begin{pmatrix} \exp(i\frac{2\pi n_j}{\lambda \cos \phi_j} L_j) & 0 \\ 0 & \exp(-i\frac{2\pi n_j}{\lambda \cos \phi_j} L_j) \end{pmatrix} \begin{pmatrix} E_{j+1}^{L+} \\ E_{j+1}^{L-} \end{pmatrix} \quad (3.20)$$

$$\equiv T_j(L_j) \begin{pmatrix} E_{j+1}^{L+} \\ E_{j+1}^{L-} \end{pmatrix}, \quad (3.21)$$

where  $T_j$  denotes the “transport matrix” corresponding to the  $j$ th layer,  $\lambda$  is the wavelength of the radiation,  $L_j$  is the thickness of the  $j$ th layer, and  $n \equiv \tilde{n} + ik$  denotes the complex refractive index.

With a linear combination of the transport and the interface matrices, i.e., Eq. 3.19 and Eq. 3.21, respectively, relations between the electric field amplitudes at different interfaces are found. For the electric field amplitudes at the first and at the second interfaces, for example, this yields:

$$\begin{pmatrix} i \\ r \end{pmatrix} = \begin{pmatrix} E_1^{L+} \\ E_1^{L-} \end{pmatrix} = I_1 \begin{pmatrix} E_1^{R+} \\ E_1^{R-} \end{pmatrix} = I_1 T_1(L_1) \begin{pmatrix} E_2^{L+} \\ E_2^{L-} \end{pmatrix}, \quad (3.22)$$

where  $i$  and  $r$  are defined as the incident and reflected electric fields, respectively.

If this is repeated for all layers, the following relation between the incident, reflected and transmitted field amplitudes can be obtained:

$$\begin{pmatrix} i \\ r \end{pmatrix} = I_1 T_1(L_1) \dots I_m T_m(L_m) I_{m+1} \begin{pmatrix} E_{m+1}^{R+} \\ E_{m+1}^{R-} \end{pmatrix} \equiv \begin{pmatrix} A_{11} & A_{12} \\ A_{21} & A_{22} \end{pmatrix} \begin{pmatrix} t \\ 0 \end{pmatrix}, \quad (3.23)$$

where the identities  $E_{m+1}^{R+} = t$  and  $E_{m+1}^{R-} = 0$  are used. The zero is due to the assumption that there is no wave incident on the back of the multilayer. This equation represents two linear equations and two unknowns, namely  $r$  and  $t$ , for a given incident amplitude  $i$ . Solving this for a normalized incident beam ( $i = 1$ ), the reflection and the transmission of the electric fields can be obtained:

$$r = \left( \frac{A_{21}}{A_{11}} \right) \quad , \quad t = \left( \frac{1}{A_{11}} \right). \quad (3.24)$$

The reflected ( $R$ ) and transmitted ( $T$ ) photon intensities are equal to  $r^*r$  and  $t^*t$ , respectively, where  $*$  denotes the complex conjugate. The absorption in the multilayer can be obtained from  $A = 1 - R - T$ .

### Field Intensity in a Multilayer

By generalizing Eq. 3.23 one can find the field amplitudes at any position in the multilayer. Namely, the electric field amplitudes at a distance  $x < L_j$  above layer  $j + 1$ , is obtained from

$$\begin{pmatrix} E_j^+(x) \\ E_j^-(x) \end{pmatrix} = T_j(x)I_{j+1}T_{j+1}(L_{j+1})\dots I_m T_m(L_m)I_{m+1} \begin{pmatrix} t \\ 0 \end{pmatrix}. \quad (3.25)$$

### Photon-Absorption in a Multilayer

Although we can calculate the total absorption of the multilayer from Eq. 3.24, the exact distribution of the deposited energy in the multilayer remains unknown. In principle, this can be calculated from the field distribution in the multilayer and the absorption coefficient of each layer. Considering the simplest approach for heat dissipation in matter via linear absorption of radiation, the optical flux absorbed at a given point in the stack is proportional to the product of the local field intensity, the real part of the refractive index, and the absorption coefficient [28]:

$$\delta A(x) = \alpha(x)\tilde{n}(x)E^{\text{tot}}(x)^2\delta x, \quad (3.26)$$

where  $x$  is the position in the multilayer,  $\delta A(x)$  the absorption in a small length interval  $\delta x$  around  $x$ ,  $\alpha \equiv 4\pi k/\lambda$  the absorption coefficient,  $\tilde{n}$  the real part of the refractive index, and  $E^{\text{tot}}(x) \equiv E^+(x) + E^-(x)$  the total electric field amplitude at position  $x$ .

Sometimes, absorption profiles and field-intensity profiles are considered the same, apart for a linearity constant between them. Although this is true for bulk materials, it is incorrect for structures consisting of different layers such in figure 3.9. This can be seen from Eq. 3.26;  $A(x) \propto E(x)^2$  only if the refractive index is constant throughout

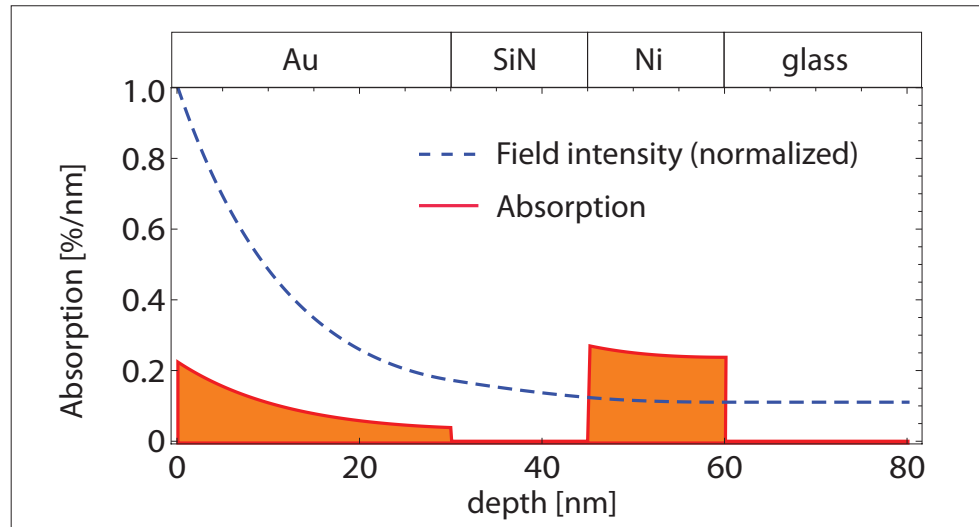


**Figure 3.9:** The absorption profile (solid line) and normalized field intensity (dashed line) of a Au(30)-SiN(15)-Ni(15)-SiO<sub>2</sub> multilayer at 800 nm.

the whole structure. This condition is obviously not met in multilayer structures in which each layer has a different refractive index. An example of an absorption-profile calculation using Eq. 3.26 is given in figure 3.9. The considered sample structure is Au(30)-SiN(15)-Ni(15)-SiO<sub>2</sub>, and the excitation wavelength is 800 nm. The dashed line gives the normalized field intensity within the sample, whereas the solid line gives the absorption per nm in the unit [%/nm]. It can be seen that the absorption and intensity profiles are significantly different in this multilayer structure: Although the light intensity through the transparent SiN layer and glass substrate is non-zero, there is no light absorption in these layers. On the other hand, a similar light intensity in the Fe layer gives rise to a high absorption because metals absorb visible light very well.

Incorrect conclusions can be drawn by not considering the “correct” absorption profile. For example, Eschenlohr *et al.* observed ultrafast demagnetization in a nickel layer with a thick gold layer on top of it (a structure similar to the one in figure 3.9) when the sample was excited with an intense 50 fs laser pulse with  $\lambda = 780$  nm [29]. Because the light intensity in the Ni layer was calculated to be much smaller than in the gold capping layer, it was concluded that the absorption in nickel is negligible. This argument was used to exclude ultrafast heating of the magnetic layer, which is the conventional explanation of ultrafast demagnetization, as a possible origin of

their observations. Instead, a novel “non-thermal” model was used to explain their results [30]. However, it can be clearly seen from figure 3.9 that the absorption in the nickel layer is significant and should not be ignored. In fact, light absorption occurs dominantly in this magnetic layer despite the thick gold capping layer.

Calculations of the absorption of light within multilayer structures play an important role in this work, and therefore, they are always calculated with the procedure explained in Section 3.4.1 and eventually Eq. 3.26. Knowledge of the refractive indices of the layers are crucial in these calculations. Fortunately, the refractive indices of many standard materials are well known in the visible spectral range and were taken from optical constant databases [24, 25]. The refractive indices of our unique magnetic layers (GdFeCo and TbFeCo), however, had to be deduced by ourselves, as explained in the following Section.

### 3.4.2 Variable Angle Spectroscopic Ellipsometer

We use a commercial Variable Angle Spectroscopic Ellipsometer (VASE) of “Woollam Co. Inc.”, sketched in figure 3.10a, to obtain the refractive index of our materials. Light from a monochromator at wavelength  $\lambda$  can be s- or p-polarized. The monochromatic light is incident at an angle  $\phi$  to the normal, and the intensity of the specular reflection is measured with a diode at  $2\phi$ . Alternatively, but not employed in this work, the ellipticity of the light can be measured with which the optical properties of the material can be deduced as well. Both the sample and the detector are at a rotation stage and therefore the reflectivity of the sample can be measured for a wide range of angles, typically  $\alpha = 15 - 75^\circ$ , with an accuracy of  $0.01^\circ$ . The spectral range of the monochromator (250-1700 nm) covers the optical and near-IR regime.

With this method the reflectivity of the sample is measured as a function of the angle of incidence for p- and s-polarized light. A typical measurement is shown in figure 3.10b (dots). For materials which consist of several layers, the reflectivity is a complex function of the optical properties of each layer, as explained in Section 3.4.1. For our samples, the optical properties of all non-magnetic layers are known, and, therefore, only the refractive index ( $n = \tilde{n} + ik$ ) of the RE-FeCo layer is unknown. This refractive index is used as a fitting parameter to the reflectivity measurements: from Eq. 3.24 the angular resolved reflectance of the multilayer is calculated for a variable refractive index of the RE-FeCo layer. Using the least mean square method, the refractive index of the magnetic layer can be obtained with high accuracy. The fits for the refractive index of  $\text{Tb}_{16}\text{Fe}_{75}\text{Co}_9$  at 800 nm are presented in figure 3.10b. By repeating the fitting-procedure for various wavelengths, the spectral dependence of the refractive index can be obtained as shown in figure 3.10c.

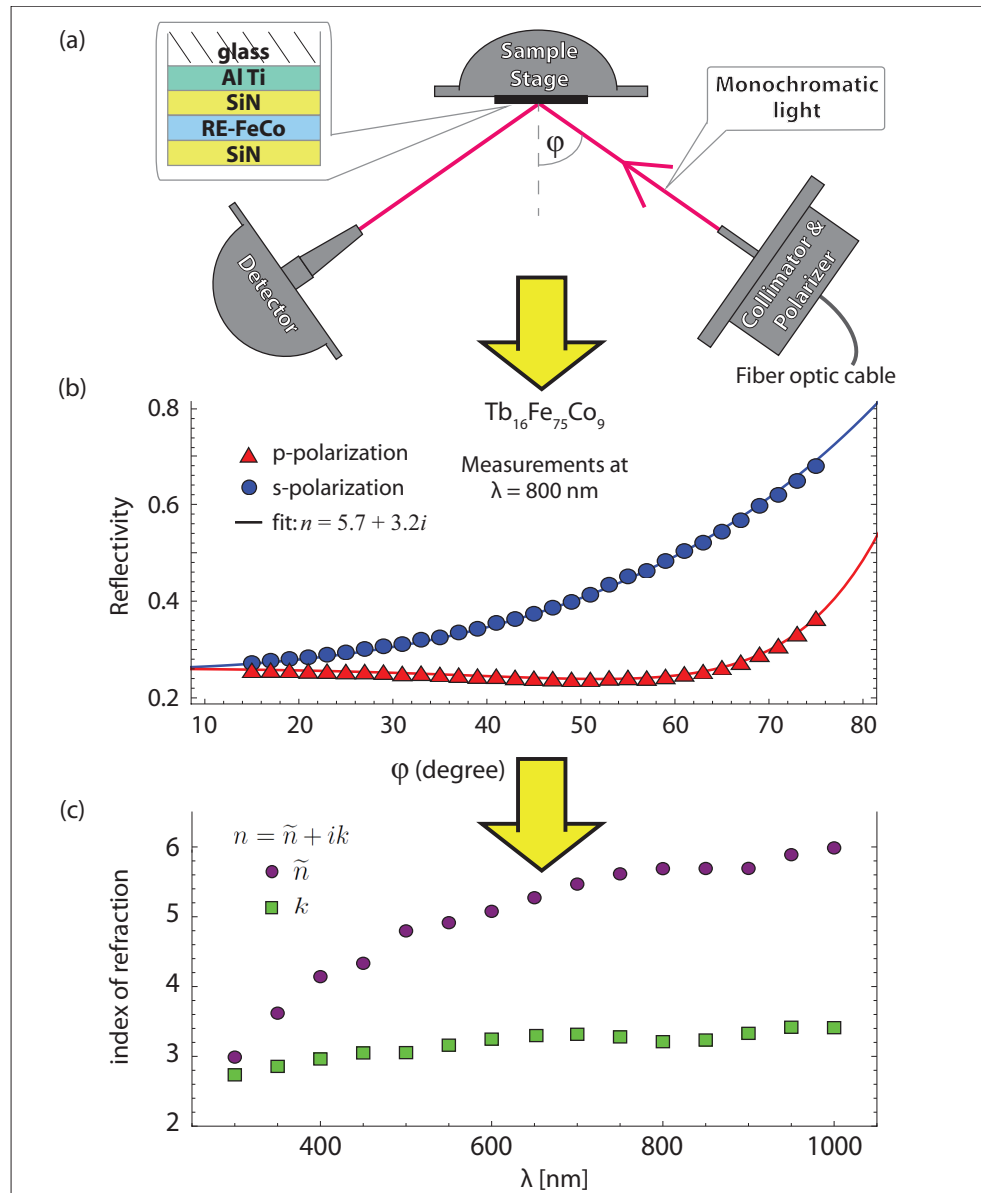


**Figure 3.10:** (a) Sketch of the VASE geometry which is employed for measuring angle-resolved reflectivity of our samples for p- and s-polarized light for a broad spectral range in the visible and near infrared regime. (b) Typical measurement of the reflectivity (magnetic layer:  $Tb_{16}Fe_{75}Co_9$ ) at  $\lambda = 800$  nm (dots), and the fits for obtaining the refractive index of the magnetic layer (solid line), as explained in Section 3.4.1. (c) The spectral dependence of the complex refractive index  $n = \tilde{n} + ik$ , obtained by repeating the procedure for various wavelengths.

### 3.5 Summary

Summarizing, the Faraday and magneto-optical Kerr effects are powerful tools to probe the magnetic state of a material with light. The possibility to create ultrashort laser pulses with commercially available laser systems, however, makes light not only an ideal probe of the magnetic state but also an ideal stimulus to perturb. This allows us to make experimental schemes employing light, for

- measuring static magnetic properties,
- creating a two-dimensional image of the magnetic state of a material, and
- measuring ultrafast magnetization dynamics.

Furthermore, a detailed analysis of light absorption in thin films is given. An ellipsometry (VASE) setup is used for obtaining optical constants of GdFeCo and TbFeCo, which is essential for an accurate calculation of the absorption profile of light in our multilayered samples.



## References

- [1] S. Foner, *Review of Scientific Instruments* **30**, 548 (1959).
- [2] R. H. Koch, C. P. Umbach, G. J. Clark, P. Chaudhari, and R. B. Laibowitz, *Applied Physics Letters* **51**, 200 (1987).
- [3] N. Bloembergen, E. M. Purcell, and R. V. Pound, *Physical Review* **73**, 679 (1948).
- [4] H. Y. Carr and E. M. Purcell, *Physical Review* **94**, 630 (1954).
- [5] M. Faraday, *Phil. Trans. R. Soc.* **136**, 1 (1846).
- [6] J. Kerr, *Philos. Mag.* **3**, 321 (1877).
- [7] U. Hartmann, *Annual Review of Materials Science* **29**, 53 (1999).
- [8] D. B. Williams and C. B. Carter, *Transmission electron microscopy: a textbook for materials science* (Springer, New York, 2009).
- [9] M. Bode, *Reports on Progress in Physics* **66**, 523 (2003).
- [10] P. Biagioni, J. S. Huang, L. Duo, M. Finazzi, and B. Hecht, *Physical Review Letters* **102**, 256801 (2009).
- [11] M. Finazzi, M. Savoini, A. R. Khorsand, A. Tsukamoto, A. Itoh, L. Duo, A. Kirilyuk, A. Kimel, T. Rasing, and M. Ezawa, submitted (2012).
- [12] D. T. Reid, *Science* **291**, 1911 (2001).
- [13] T. Popmintchev, M. C. Chen, D. Popmintchev, P. Arpin, S. Brown, S. Alisauskas, G. Andriukaitis, T. Balciunas, O. D. Mucke, A. Pugzlys, et al., *Science* **336**, 1287 (2012).
- [14] A. Zvezdin and V. Kotov, *Modern Magneto-optics and magneto-optical materials* (IOP Publishing Ltd., 1997).
- [15] P. Oppeneer, in *Handbook of Magnetic Materials*, edited by K. Buschow (Elsevier, Amsterdam, 2001), vol. 13.
- [16] H. Lorentz, *Verslagen en mededeelingen der Koninklijke Akademie van Wetenschappen* **2**, 217 (1883).
- [17] H. Lorentz, *Arch. Neerl.* **19**, 123 (1884).
- [18] K. Vahaplar, Ph.D. thesis (2010).

- 
- [19] Spectra-Physics, *Tsunami: Mode-Locked Ti:Sapphire Laser, User's Manual* (Spectra-Physics, The Solid-State Laser Company, Mountain View, CA, U.S.A., 2002).
- [20] Spectra-Physics, *Spitfire Pro: Ti:Sapphire Regenerative Amplifier Systems, User's Manual* (Spectra-Physics, The Solid-State Laser Company, Mountain View, CA, U.S.A., 2005).
- [21] Spectra-Physics, *OPA-800C: Ultrafast Optical Parametric Amplifier, User's Manual* (Spectra-Physics, The Solid-State Laser Company, Mountain View, CA, U.S.A., 2003).
- [22] B. Koopmans, in *Spin Dynamics in Confined Magnetic Structures II*, edited by B. Hillebrands and K. Ounadjela (Springer-Verlag, Berlin, 2003).
- [23] S. Wolfram, *The Mathematica Book* (Wolfram Media, 2003), 5th ed.
- [24] E. D. Palik, ed., *Handbook of optical constants of solids II* (Academic Press, San Diego, 1998).
- [25] B. L. Henke, E. M. Gullikson, and J. C. Davis, *Atomic Data and Nuclear Data Tables* **54**, 181 (1993).
- [26] M. Born and E. Wolf, *Principles of Optics* (Cambridge University Press, New York, 1999), 7th ed.
- [27] J. S. C. Prentice, *Journal of Physics D-Applied Physics* **33**, 3139 (2000).
- [28] O. Arnon and P. Baumeister, *Applied Optics* **19**, 1853 (1980).
- [29] A. Eschenlohr, M. Battiato, P. Maldonado, N. Pontius, T. Kachel, K. Holdack, R. Mitzner, A. Föhlich, P. M. Oppeneer, and C. Stamm, submitted (2012).
- [30] M. Battiato, K. Carva, and P. M. Oppeneer, *Physical Review Letters* **105**, 027203 (2010).

## CHAPTER 4

---

### All-Optical Magnetic Recording and the Role of Light<sup>1</sup>

---

*“Have patience. All things are difficult before they become easy.”*

SAADI, PERSIAN POET, 13TH CENTURY

---

<sup>1</sup>In part adapted from: A. R. Khorsand, M. Savoini, A. Kirilyuk, A. V. Kimel, A. Tsukamoto, A. Itoh, and Th. Rasing, “Role of magnetic circular dichroism in all-optical magnetic recording”, *Physical Review Letters* **108**, 127205 (2012).

## 4.1 Introduction

Controlling the magnetic state of a medium with the help of femtosecond laser pulses is a recently emerging and rapidly developing research direction in modern magnetism. The interest to the problem of the ultrafast optical control of magnetism was triggered by pioneering work by Beaurepaire *et al.* [1], who found that excitation of magnetic Ni with a femtosecond laser pulse resulted in the quenching of the magnetization within a picosecond. This is much faster than one might expect supposing that the demagnetization is defined by the characteristic time of the spin-lattice interaction in the ground state. Therefore, it was suggested that the ultrafast laser-induced demagnetization was due to ultrafast angular momentum transfer from light to the medium. Soon it was argued however, that such a mechanism is negligible since the total angular momentum of photons in realistic experiments is not large enough to contribute significantly to the observed changes of the magnetization of the media [2].

The discussion about the mechanisms of light-matter interaction in optical control of magnetism was revived after the discovery of *all optical switching* (AOS) with the help of circularly polarized (CP) light [3]. Namely, it was shown that in a certain range of pulse energies  $\mathbf{M}$  is not only quenched, but is fully reversed when the medium is exposed to one light-helicity while it is not affected if the helicity is opposite. This *helicity dependent AOS* (HD-AOS) was observed in ferrimagnetic GdFeCo in the absence of an external magnetic field. The role of light, and in specific its helicity, angular momentum, and energy, in AOS are still open fundamental issues and subject of intense discussions in modern magnetism [4].

Until now, the only hypothesis explaining AOS was the “inverse Faraday effect” (IFE): CP light acts as a strong effective magnetic field pulse  $B_{\text{eff}}$  on the spins of the medium. The direction of  $B_{\text{eff}}$  is defined by the helicity of the light. Atomistic spin simulations performed under the assumption that light acts as  $B_{\text{eff}} = 20$  T were able to describe some key features of AOS, such as the feasibility to reverse the magnetic state with an intense enough circularly polarized pulse [5].

Although the existence of such effective magnetic field was demonstrated by the experiments on dielectrics [6–9], so far this effective field has been described only phenomenologically. The equation describing it was derived in a non-dissipative approximation and thus the microscopical origin of the IFE-field in metallic GdFeCo is still a subject of research. Furthermore, simulations based on the IFE have shown only a qualitative agreement with a few key features of HD-AOS, whereas some other key features are not explained. For example, at high enough light intensities, the magnetization can be reversed with either light-helicity, in striking contrast to simulations where only one helicity could reverse the magnetization [5].

Hence, the microscopic mechanism of the light-matter interaction responsible for AOS has not been revealed yet. It is the aim of the work presented in this chapter to understand the role of light in AOS, and, in specific, which properties of light are

responsible for this phenomenon. In general, the effects of light-matter interaction can be divided into two groups: those that result in an absorption of light and those that lead to a change of the phase of the radiation. Consequently, helicity dependent effects in optics of magnetic media can be seen as magnetic circular dichroism (MCD) or magnetic circular birefringence (MCB), respectively. We reveal which one of these two groups is responsible for HD-AOS by performing systematic measurements of AOS as a function of different light parameters, such as wavelength, intensity and polarization, and comparing them with the spectral dependencies of MCD and MCB.

This chapter is organized as follows. In Section 4.2 the properties of the GdFeCo sample under study are discussed. Next, in Section 4.3 the experimental results are presented and discussed. It is shown that AOS is subjected to a threshold fluence of  $2.6 \pm 0.2$  mJ/cm<sup>2</sup> absorbed in the magnetic medium, independent of the wavelength and polarization of the excitation pulse. Furthermore, it is shown that the helicity dependence of AOS is a natural consequence of MCD. This provides a *quantitatively* explanation of HD-AOS. In Section 4.5, the results of other experiments on AOS are addressed and fully explained with the new understanding of the role of light in this phenomenon. Finally, an outlook of AOS is presented in Section 4.6, and it is demonstrated that decreasing the “bit” to the nanometer scale is feasible.

## 4.2 Sample

The magnetic material which we studied was a 20 nm thick RE-TM alloy Gd<sub>26</sub>Fe<sub>65</sub>Co<sub>9</sub> layer. The sample was grown by magnetron sputtering in the following multilayer structure: SiO<sub>2</sub>-AlTi(10)-SiN(5)-GdFeCo(20)-SiN(60). The values in parentheses represent the layer thicknesses in nm. The thick capping layer protects the magnetic layer from oxidation. The AlTi layer serves as a reflector for enhancing the magneto-optical (MO) signal and as a heat sink. The GdFeCo layer is a ferrimagnetic film with perpendicular magnetic anisotropy and a coercive field of 100 Gauss.

### 4.2.1 Optical Characterization

The complex refractive index of the GdFeCo layer was obtained from reflectometry measurements (see Section 3.4.2) in the wavelength range 400-800 nm. First, we measured angle-resolved reflectivity of the multilayer with polarized light of wavelength  $\lambda$ . The incident angle  $\phi$  is varied from 15° to 70° (see inset figure 4.1). Using a standard fitting procedure, we fixed the refractive indices of all non-magnetic layers and used the complex refractive index ( $n = \tilde{n} + ik$ ) of the GdFeCo layer as a fitting parameter to the reflectivity measurements. The refractive indices of the non-magnetic layers are taken from Palik [10], and shown in Table 4.1. An example of such measurements and corresponding fit is shown in figure 4.1 for  $\lambda = 800$  nm. In these measurements,

s- and p-polarized light are used. From the fit we obtain  $n_{LP} = 2.66+3.60i$  at 800 nm for the GdFeCo layer.

**Table 4.1:** The thickness and the refractive indices for linearly polarized light of each layer in the wavelength regime 500-800 nm. The refractive indices of all non-magnetic layers are from Palik [10]. The refractive index of the GdFeCo layer is obtained from reflectometry measurements (see Section 3.4.2). An example of such measurement on  $\text{Gd}_{26}\text{Fe}_{65}\text{Co}_9$  is shown in figure 4.1.

layer	thickness [nm]	refractive indices for LP light at $\lambda$			
		500 nm	600 nm	700 nm	800 nm
SiN	60	2.04	2.03	2.02	2.01
GdFeCo	20	$1.76+2.51i$	$1.86+2.94i$	$2.41+3.45i$	$2.66+3.60i$
SiN	5	2.04	2.03	2.02	2.01
AlTi	10	$1.28+4.24i$	$1.62+5.03i$	$2.12+5.73i$	$2.83+5.88i$
SiO <sub>2</sub>	substrate	1.55	1.54	1.54	1.54

## 4.2.2 Magneto-Optical Characterization

By using CP light instead of linearly polarized (LP) light, it is possible to obtain the complex refractive indices  $n_{LC}$  and  $n_{RC}$  for left-handed circularly polarized (LC) and right-handed circularly polarized (RC) light, respectively. They can be defined as  $n_{LC}(M) = n_{LP} + \frac{1}{2}\Delta n(M)$  and  $n_{RC}(M) = n_{LP} - \frac{1}{2}\Delta n(M)$ . The first term is the refractive index for LP light, given in Table 4.1. The second term rises from the off-diagonal component of the permittivity tensor of GdFeCo and is antisymmetric in the magnetization, i.e.,  $\Delta n(-M) = -\Delta n(M)$ . Note that this term is of a purely magnetic origin, and by definition vanishes for  $M=0$ . Furthermore, the reversal of light-helicity is symmetrically equivalent to the reversal of the magnetization. The values of  $\Delta n(+M)$  are presented in Table 4.2 for  $\lambda = 500 - 800$  nm (see Section 4.4).

## 4.3 Experimental Details

All-optical switching was studied by exciting the material with a single laser pulse ( $\tau \approx 55$  fs) using MO microscopy to determine the final magnetic state of the exposed area. This was done as a function of three light parameters: polarization, intensity, and wavelength. The result after each exposure was defined as “0” in the case of no switching, and “1” in the case of switching, illustrated in figure 4.2. Subsequently, an external magnetic field pulse was applied to bring the ferrimagnet back to its initial state. The initial magnetization was always in the “up”-direction, while the

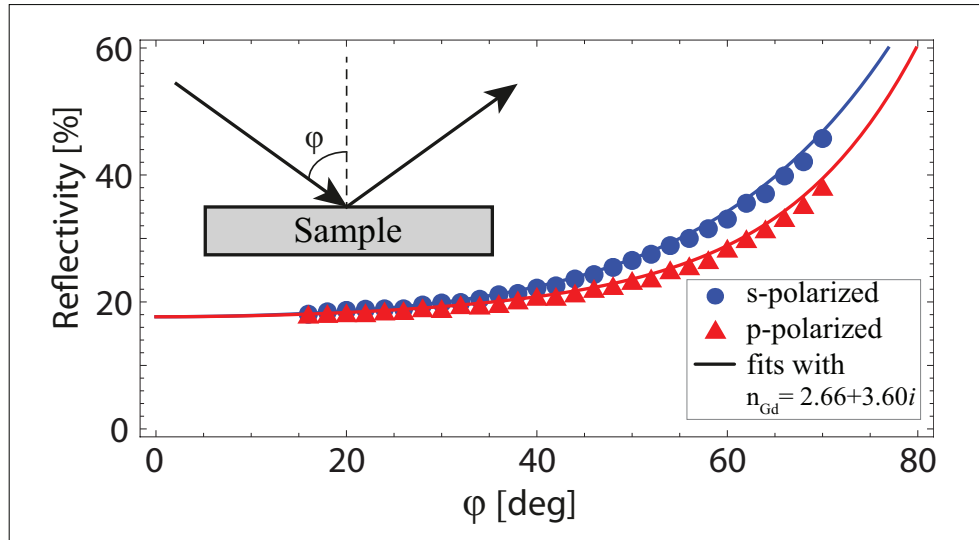


**Figure 4.1:** Angular-resolved reflectivity measurement of the sample with s- and p-polarized light at  $\lambda=800$  nm. The incident angle  $\phi$  is relative to normal as sketched in the geometry shown in the inset, and is varied from  $15^\circ$  to  $70^\circ$ . The solid line gives the fit of the data using the layer properties given in Table 4.1.

polarization was varied from left-, via linear to right-handed circular polarization. It should be noted that it is symmetrically equivalent to fix the helicity and vary the magnetic state from “up” to “down”. For a sketch and more details of the experimental setup, see Section 3.2.5. This procedure was repeated for typically 20 times at every set of light-parameters and resulted into a binary distribution of “1” and “0”. This allowed us to obtain the switching probability  $P_\sigma$ , defined as the mean of the binary distribution, as a function of fluence  $F$  and light-polarization  $\sigma$ . We define the fluence as the pulse energy divided by the beam area (defined as the standard deviation of a Gaussian distribution). The beam area at the sample surface was measured accurately at each wavelength with the so called “Liu-Method”, which is explained in the following.

### Spot Size Characterization

The uncertainties in the beam area and the excitation fluence are quadratically dependent on the uncertainty of the radius the excitation pulse. Therefore, in order to be able to compare fluences at different excitation wavelengths, it is crucial to use an

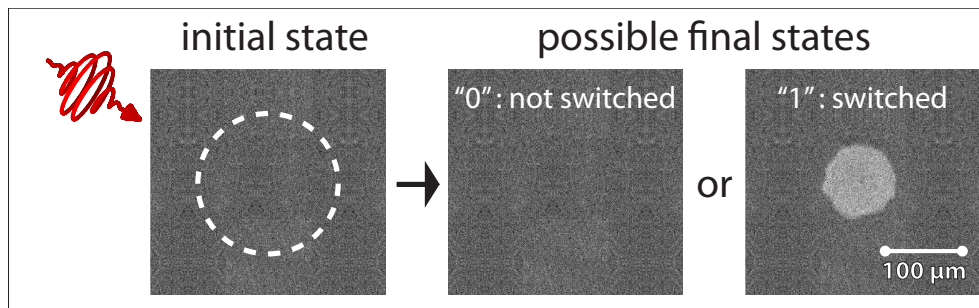


**Figure 4.2:** Magneto-optical images of  $\text{Gd}_{26}\text{Fe}_{65}\text{Co}_9$ , before and after exposure to a single 55 fs laser pulse. The dark and bright regions correspond to magnetization “up” and “down”, respectively. The sample is initially magnetized in the “up” direction. After exposure, the magnetic state of the sample can relax back to its initial state (“0”) or to a switched state (“1”).

accurate method for determining the beam radius, which is wavelength dependent.

One method is the so called “knife-edge” method [11]. A knife is moved in the lateral direction of the beam, and therefore it blocks a part of the light. By measuring the total transmitted energy as a function of the position of the knife, an error function is obtained, from which the radius of the beam can be deduced. Due to its accuracy and simplicity, the “knife-edge” method is widely used for spot size determination. However, this method has some limitations. First of all, one is limited to a circular and Gaussian beam profile in the focus which is not always the case. Secondly, the actual spot size on the sample surface can deviate from the spot size measured with this technique as the knife and the sample are usually not exactly at the same position.

A method which overcomes these limitations is the Liu-method [12–14]. This method can be applied only to samples which have a threshold at which optical properties of the material change, such as an ablation or melting threshold, or, in the case of  $\text{Gd}_{26}\text{Fe}_{65}\text{Co}_9$ , a switching threshold of magnetic domains. We assume that the domain is stable after the reversal. In short, MO images of the surface are taken after excitations with different energies. At the edge of the switched area, the excitation fluence is always equal to the switching threshold. As a consequence, the switched area is proportional to the logarithm of the pulse energy with a proportionality constant equal to the beam area [12–14].

We applied this method for spot size characterization at 500, 600, 700, and 800 nm. The power of this method becomes clear from the accuracy of the fits. As an illustration, we have plotted the spot size measurements at 700 nm in figure 4.3. The polarization was varied from LC (blue), LP (green), to RC (red). It can be seen from the slopes of the fits that the spot size is polarization independent. We obtain a beam radius of  $r_0 = 38.9 \pm 0.9 \mu\text{m}$  at 700 nm. On the other hand, the intersections of



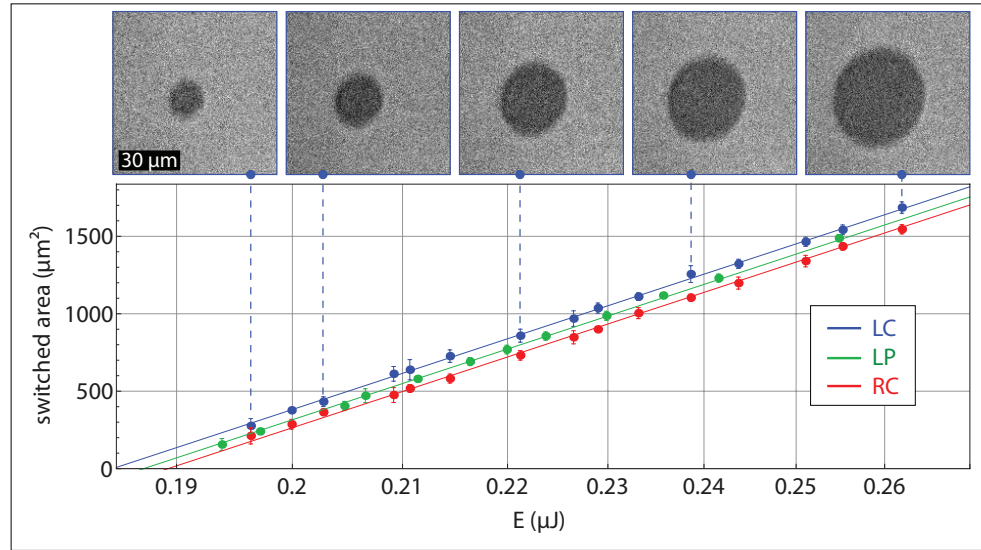


**Figure 4.3:** The switched area is plotted as a function of the pulse energy at  $\lambda = 700$  nm, for LC, LP, and RC polarized pulses. The energy-axis is on a logarithmic scale. The switched area was obtained from 10 measurements at each pulse energy. In the top part images are shown of switched areas for five different pulse energies. The switched area is proportional to the logarithm of the energy. The slope gives the lateral beam area of the excitation pulse, and is independent of the light-polarization.

the fits with the  $x$ -axis are polarization dependent. This is due to helicity dependent switching threshold, which will be discussed in the following Sections.

## 4.4 Results and Discussion

In figure 4.4 the results of the switching probability are presented as a function of the fluence for LC and RC laser pulses for  $\lambda = 500 - 800$  nm. These measurements show that at low fluences there is *no switching* for any light-helicity, whereas at high enough fluences (yet smaller than the damage threshold), there is *always switching* for any helicity. The same holds for LP light, as this is simply a superposition of RC and LC light. Furthermore, there is a small intensity window in which switching is helicity dependent.

In the ideal case of no pulse-to-pulse fluctuations of the laser (e.g., fluctuations in the pulse energy and/or the spatial beam profile),  $P_{\sigma}$  is presumably given by a step function centered at the threshold fluence  $F_{\sigma}$ , as illustrated in the inset of figure 4.4.

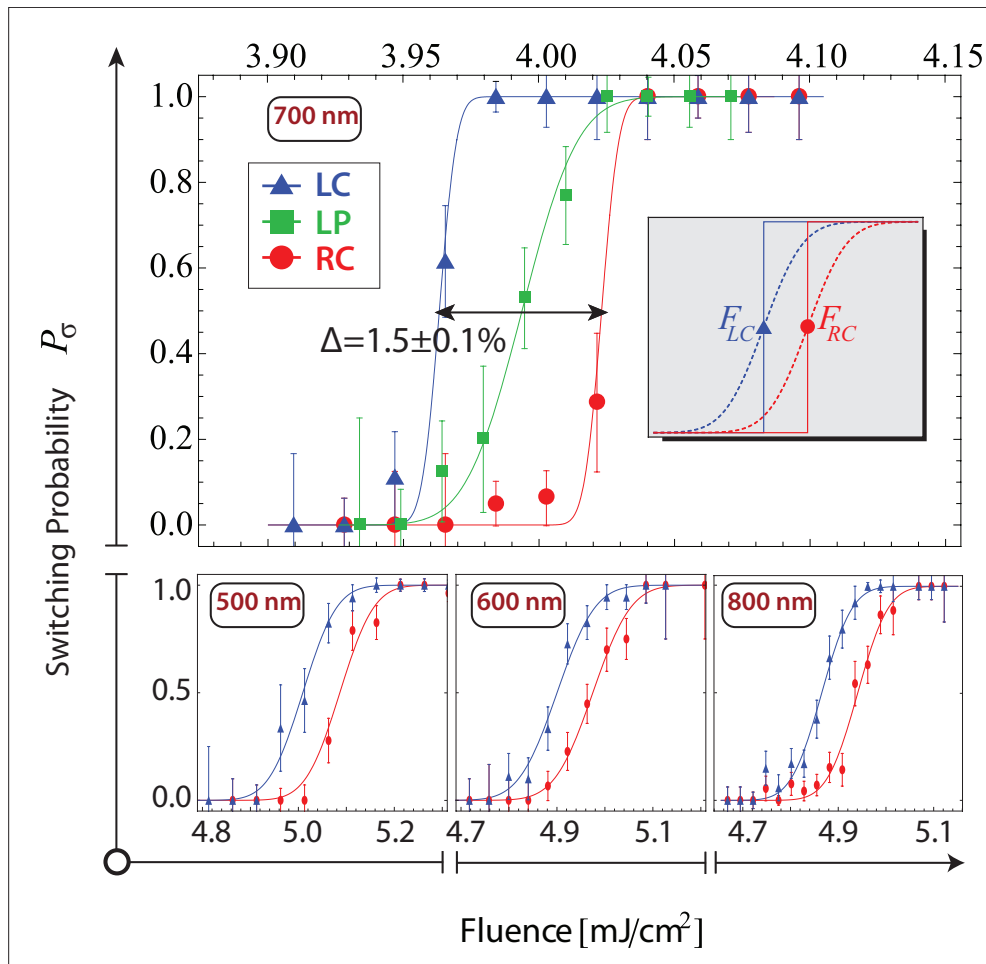


**Figure 4.4:** (top) Switching probability  $P_\sigma$  as a function of the fluence at  $\lambda = 700$  nm for three different polarizations. The measurements with RC, and LC pulses were performed at a different time than the ones with LP pulses, and therefore the laser stability  $\epsilon$  was different. Inset: Illustration of the switching probabilities in case of zero (solid) and nonzero (dashed) laser fluctuations using Eq. 4.1.  $F_{LC}$  and  $F_{RC}$  denote the switching threshold of GdFeCo for LC and RC excitation pulses, respectively. (bottom) Switching probability as a function of the fluence at  $\lambda=500$ , 600, and 800 nm, respectively.

More generally, in the realistic case of finite pulse-to-pulse fluctuations (dashed lines in the inset of figure 4.4),  $P_\sigma$  is given by an error function:

$$P_\sigma(F) = \frac{1}{\sqrt{\pi}\epsilon F_\sigma} \int_0^F dF' e^{-(F'-F_\sigma)^2/(\epsilon F_\sigma)^2}, \quad (4.1)$$

where  $\epsilon$  is a unitless quantity representing the relative magnitude of the pulse-to-pulse laser fluctuation, which varies typically between 0.5% – 2%.

We define the intensity window ( $\Delta$ ) of HD-AOS, as

$$\Delta = \frac{F_{RC} - F_{LC}}{\frac{1}{2}(F_{RC} + F_{LC})}. \quad (4.2)$$

Note that while pulse-to-pulse fluctuations do affect the shape of  $P_\sigma$ , the value  $\Delta$  is not affected by these fluctuations (see inset figure 4.4).

The experimental results of the intensity window and the switching thresholds for  $\lambda = 500 - 800$  nm are summarized in Table 4.2. We notice that the intensity window  $\Delta$  is almost independent of the excitation wavelength, whereas there is a wavelength-dependence in the threshold fluence for switching.

#### 4.4.1 Inverse Faraday Effect

In order to understand the origin of the window it was hypothesized that the latter is due to an effective magnetic field generated by CP light via the IFE [3, 5]. Van der Ziel and Pershan [15, 16] showed using arguments of thermodynamical equilibrium that CP light may act on a medium as an effective magnetic field

$$\mathbf{B}_{\text{eff}} = \epsilon_0 K \mathbf{E}(\omega) \times \mathbf{E}(\omega)^*, \quad (4.3)$$

**Table 4.2:** Results from single-shot MO microscopy measurements, reflectometry measurements and from calculations at four different excitation wavelengths.  $F_{LP}$  denotes the switching threshold fluence using LP light. The errors originate from the uncertainties in the spot sizes, which were accurately measured with the Liu method [12–14]. The window  $\Delta$  is defined in Eq. 4.2. From ellipsometry measurements the refractive index of GdFeCo for LP light  $n_{LP}$ , and  $\Delta n$  were obtained.  $A_{LP}$  denotes the total absorption of LP light in the GdFeCo layer, and MCD the calculated magnetic circular dichroism in GdFeCo.

$\lambda$ (nm)	<i>single-shot imaging</i>		<i>reflectometry</i>	<i>calculations</i>	
	$F_{LP}$ (mJ/cm <sup>2</sup> )	$\Delta$ (%)	$\Delta n(+M)$	$A_{LP}$ (%)	MCD (%)
500	5.04±0.75	1.50±0.21	0.024 + 0.052 <i>i</i>	53.0	1.46 ± 0.26
600	4.84±0.96	1.65±0.08	0.040 + 0.044 <i>i</i>	59.5	1.51 ± 0.21
700	3.99±0.38	1.49±0.10	0.082 + 0.056 <i>i</i>	62.0	1.45 ± 0.15
800	4.90±1.05	1.54±0.10	0.088 + 0.050 <i>i</i>	51.8	1.33 ± 0.13

where  $K$  denotes the MO susceptibility (see Section 3.2.2), and  $\mathbf{E}$  the electric field of the incoming pulse. Note that the effective magnetic field is maximum for CP light, while it vanishes for LP light. In a non-dissipative approximation, the strength of this field for CP light is given by [4]

$$B_{\text{eff}} = \frac{\theta_F \lambda \tilde{n} F}{\pi M_0 c \tau d}, \quad (4.4)$$

where  $\theta_F$  is the Faraday rotation at saturated magnetization,  $\tilde{n}$  is the real part of the refractive index,  $d$  is the thickness of the GdFeCo layer,  $F \approx 5 \text{ mJ/cm}^2$  the fluence of the excitation pulse,  $M_0 \approx 10^5 \text{ A/m}$  [3] the static magnetization,  $c$  the speed of light and  $\tau \approx 55 \text{ fs}$  the temporal pulse length.

We would like to stress that although the existence of  $B_{\text{eff}}$  has been demonstrated experimentally [6–9], there is no experimental evidence that Eq. 4.4 is an adequate representation of the effective magnetic field generated by CP light in GdFeCo. This equation intrinsically neglects effects of absorption, taking into account only those effects of light-matter interaction that are related to a phase change of the light waves. Consequently, this approach accounts for MCB and neglects MCD in a medium. Note that these two effects have different spectral dependencies.

From spectral measurements of  $\theta_F$  (inset figure 4.5) and  $n$  (Table 4.2), we calculated  $B_{\text{eff}}$  as a function of the wavelength. This is plotted in figure 4.5a (open dots) together with the switching window  $\Delta$  (closed dots). It can be seen that the calculated  $B_{\text{eff}}$  has a strong wavelength dependence, whereas the switching window is almost constant in this spectral range.

#### 4.4.2 Magnetic Circular Dichroism

Alternatively, we will consider MCD as the possible origin of HD-AOS. GdFeCo is well known for its strong MO effect in the (near-)visible spectral range. Therefore, RC and LC pulses experience different refractive indices in this material and, consequently, a difference in absorption of RC and LC pulses is expected.

The total absorption in the GdFeCo layer  $A_\sigma$  is calculated as a function of light-polarization  $\sigma$ , and -wavelength  $\lambda$ . The algorithm which was used for this purpose is explained in Section 3.4.1. For the refractive index of the layers we used the values in Table 4.1 and Table 4.2, which are helicity-dependent. First, the absorption profile in the sample was calculated with Eq. 3.26. An example of the absorption profile is presented in figure 4.6 for LP light and  $\lambda = 800 \text{ nm}$ .

The total absorption  $A_\sigma$  in the GdFeCo layer at polarization  $\sigma$  can now be deduced from the absorption profile by integrating it over the whole GdFeCo layer, i.e., from  $x = 60 \text{ nm}$  to  $x = 80 \text{ nm}$  in figure 4.6. Subsequently, we can calculate the MCD from

$$\text{MCD} = \frac{A_{LC} - A_{RC}}{A_{LP}}. \quad (4.5)$$

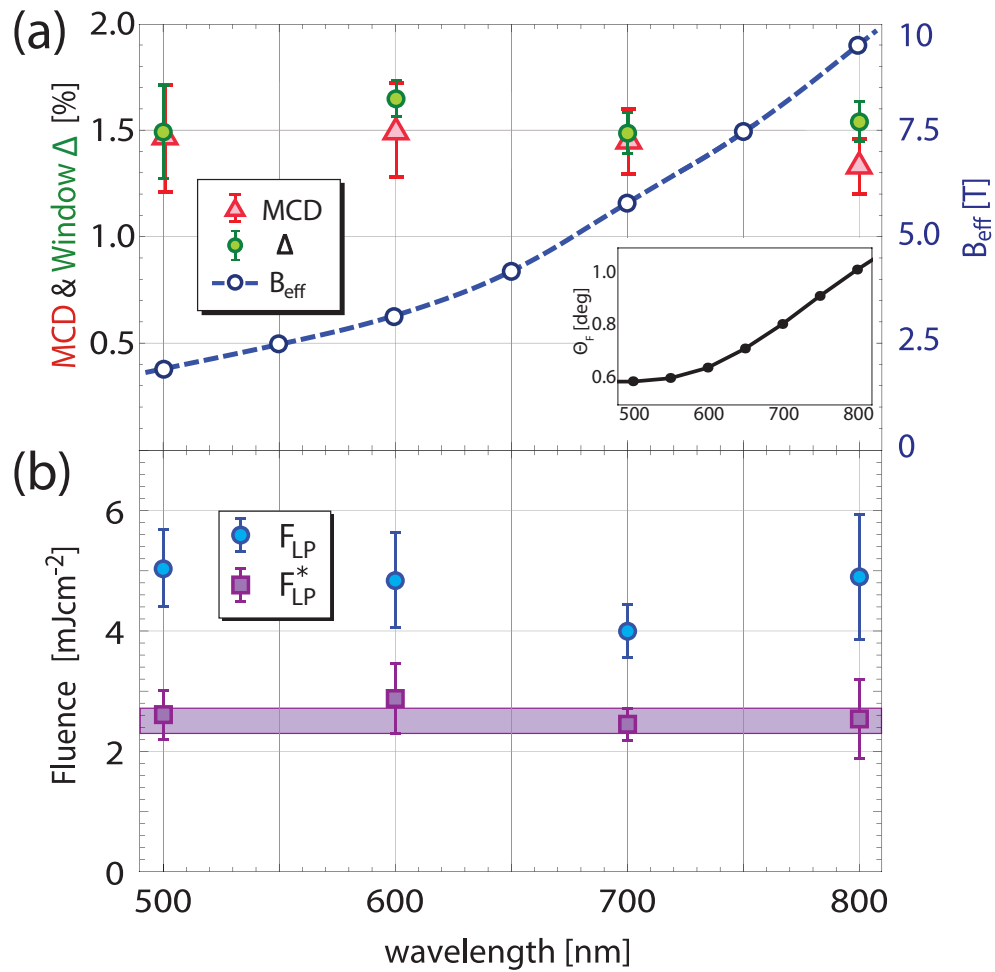


**Figure 4.5:** (a) The spectral dependence of the window  $\Delta$ , IFE field  $B_{\text{eff}}$ , and MCD in GdFeCo. In the inset the spectral dependence of the Faraday rotation  $\theta_F$  is shown. (b) The switching threshold fluence  $F_{LP}$  and the effective threshold fluence  $F_{LP}^*$  plotted against  $\lambda$ . The solid line gives the intersection of the different values of  $F_{LP}^*$  and is equal to  $2.6 \pm 0.2 \text{ mJ}/\text{cm}^2$ .

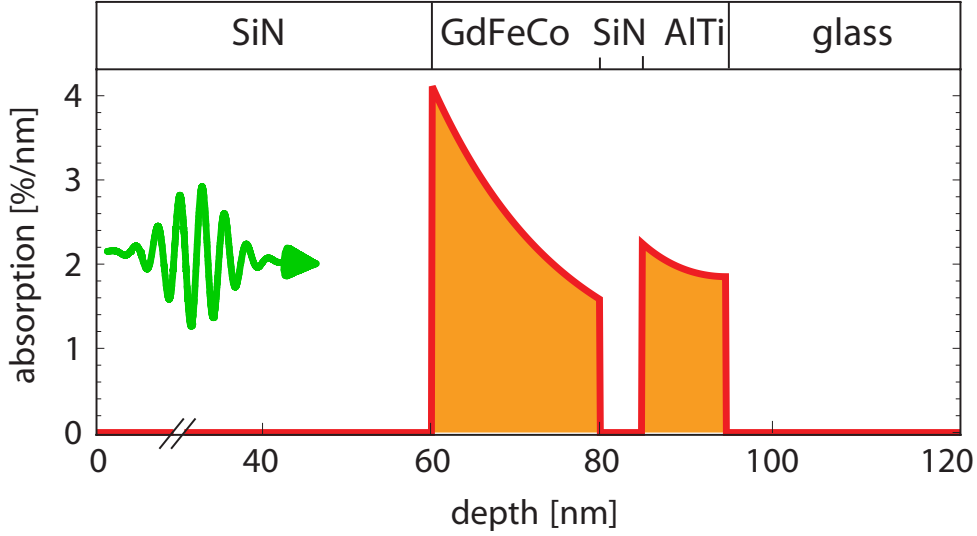


**Figure 4.6:** Absorption profile of the multilayer stack for LP light at  $\lambda=800$  nm calculated with the method described in Section 3.4.1.

The absorption of LP light is equal to  $A_{LP} = \frac{1}{2}(A_{RC} + A_{LC})$ . The thus obtained values for MCD in GdFeCo are given in Table 4.2. These values show that the switching window in GdFeCo, expressed in terms of relative fluence  $\Delta$ , exactly corresponds to the relative absorption of RC and LC light, given by the MCD values. This correspondence can also be seen clearly from figure 4.5a, where the spectral dependencies of MCD and the window  $\Delta$  are plotted together.

#### 4.4.3 Switching Threshold

Note that the correlation of  $\Delta$  and MCD indicates that the switching thresholds for LC and RC light are different by exactly the same amount as the difference between the total absorption in the GdFeCo layer for LC and RC light, respectively. The effective switching threshold  $F_{\sigma}^*(\lambda) = F_{\sigma}(\lambda)A_{\sigma}(\lambda)$ , i.e., the actual absorbed energy density in the GdFeCo layer at which switching occurs, is therefore independent of the polarization:  $F_{RC}^*(\lambda) = F_{LP}^*(\lambda) = F_{LC}^*(\lambda)$ . In fact, the effective switching threshold is also independent of the wavelength and is equal to  $F^* = 2.6 \pm 0.2$  mJ/cm<sup>2</sup>, as can be seen in figure 4.5b.

These results demonstrate that given a 55 fs excitation pulse, AOS depends only on the amount of energy absorbed by the magnetic system, independent of the wave-

length or helicity of the laser pulse. Because of different absorption coefficients for RC and LC light in GdFeCo, however, the switching threshold is helicity-dependent. We can conclude that the role of light in AOS is ultrafast heating of the magnetic material, and that HD-AOS originates from MCD. Considering the errors in our measurements, possible contributions of other mechanisms (such as the inverse Faraday effect) to HD-AOS are at least 10 times smaller than MCD.

The demonstration that AOS relies on absorption only, supports recent simulations showing that a heat pulse can be sufficient to switch the magnetic state of GdFeCo [17, 18]. It was shown that strongly nonequilibrium conditions induced by an ultrashort heating pulse in multisublattice magnetic systems such as GdFeCo, can lead to sublattices that evolve temporarily against their intersublattice exchange interaction. This results in a transient ferromagnetic-like state within a picosecond after excitation [19]. On a longer time scale, the sublattices will align antiparallel again due to their intersublattice exchange interaction. This results in an overall reversal of the net magnetization due to heating, i.e., absorption of the laser light.

## 4.5 Explaining Observations in other Work with MCD

In this paragraph the validity of the new understanding of AOS is tested against the experimental results of other work, which were until now only partly understood [3]. In principle, there were several different experiments in which GdFeCo was exposed to laser pulses at a repetition rate of 1 kHz. Although until now *some* features of the results were explained with IFE, we show that *all* observations can be explained rather easily with MCD.

### 4.5.1 Sweeping over the Surface

Interestingly, it has been observed that with multiple-shot exposures it is possible to obtain helicity dependent switching of large areas, even for intensities much higher than the regime where HD-AOS occurs with a single pulse [3]. This observation is illustrated in figure 4.7, and the experimental results are presented in the inset. CP pulses are swept over the surface (from left to right in figure 4.7) with a 1 kHz repetition rate. For the given helicity, more energy is absorbed in the black (“M up”) than the white domain (“M down”) due to MCD. In the center of the excited area, the absorbed intensity is always higher than the switching threshold, and, therefore, both magnetic states switch after each pulse. Near the edge of the excited area, however, there is a small ring-shaped region where only black domains switch to white. Although for a black domain, the absorbed intensity is just enough to switch to white, the white domain will not switch back to black because the absorbed intensity is smaller than the switching threshold. Hence, the beam will leave a trail of white domain when moving over the surface of the magnet. This trail is visible when

the underlying  $M$  is “up” (black) but invisible when it is “down” (white), in exact agreement with observations in ref. [3] (see inset figure 4.7).

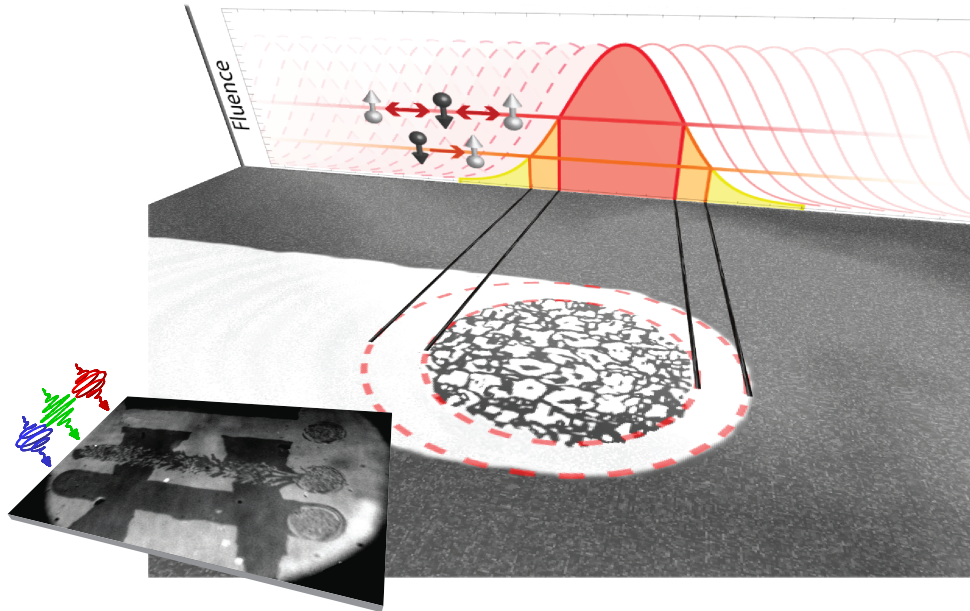


**Figure 4.7:** Illustration of multiple-shot switching through MCD with CP excitation pulses. In the center of the excited area, both magnetic states can switch because of the high fluence. Conversely, at the edges (i.e., between the dashed borders) helicity dependent switching occurs, and, therefore, a single domain state is formed. Hence, by sweeping multiple CP excitation pulses over the surface, a large area can be switched. Inset: Experimental data from ref. [3] showing a MO image of GdFeCo after sweeping LC, LP, and RC polarized laser pulses with 1 kHz over the surface.

#### 4.5.2 Exposing a Domain Wall

In another experiment a beam with CP pulses was fixed at a position near a domain wall with a repetition rate of 1 kHz. In figure 4.8a a MO image is shown, which is taken during the exposure [3]. It can be seen that in the upper (white) domain, a switched black ring is formed around a grey area. In the bottom (black) domain, only a grey area is formed.

In order to understand these results with MCD, we have illustrated in figure 4.8b the effect of each excitation pulse on the magnetic material for five subsequent pulses.



The initial state consists of two domains, separated by a domain wall (first image of figure 4.8b). When a CP pulse excites the material near the domain-wall, the magnetic state switches at any place where the absorbed intensity reaches the switching threshold. As the white domain absorbs better than the black domain for the chosen helicity, the switched areas in each domain have different radii (second image of figure 4.8b). The second pulse is absorbed efficiently in the white half-circle, and therefore the bottom domain turns fully black. However, the absorption in the black half-circle is less efficient and therefore only a part of it switches back. As a consequence, there remains a trail of a black ring in the white domain (third image of figure 4.8b). Similarly, it can be shown that the second and third state are reproduced for each subsequent pulse. As the shutter speed of a typical camera is much longer than 1 ms, i.e., the time difference between each subsequent excitation pulse, it takes basically the superimposed image of the second and third state of figure 4.8b. This state is shown in figure 4.8c, which is almost identical to the experimental observation.

## 4.6 Outlook

The results in this chapter may give rise to new opportunities, and allows to alter certain material properties to improve switching characteristics. First of all, from the demonstration that AOS originates from light absorption and not from an intense effective magnetic field pulse which is strongly dependent on the pulse duration, one could assume that the AOS is not limited to sub 100 fs pulses, but may also be feasible for longer pulses (at least a few ps) which are more economical and cheaper to produce. Indeed, it has been demonstrated recently that also picosecond pulses

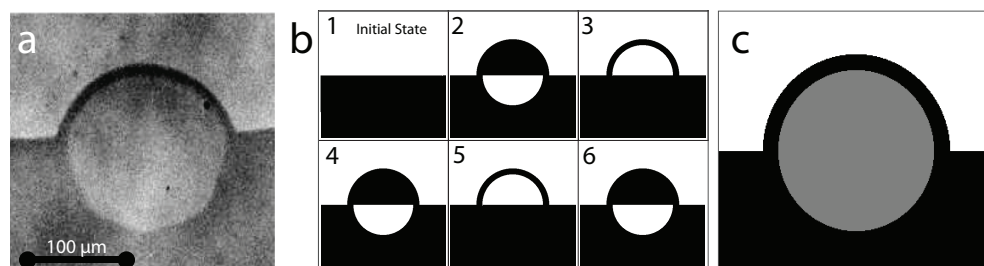


**Figure 4.8:** (a) A MO image from ref. [3] during the exposure with CP pulses at a repetition rate of 1 kHz near a domain wall of GdFeCo. (b) A schematic representation of the magnetic state after each subsequent pulse based on single shot switching over the switching threshold. (c) An illustration of the superimposed magnetic state, as would be seen in a MO image during exposure.

are sufficient to trigger AOS, however, at a cost of energy efficiency [20].

The switching reproducibility and the size of the switched domains are important characteristics for a possible application of all-optical magnetic recording. The reproducibility is defined by the size of the switching window and the signal-to-noise ratio, and will be discussed in the following paragraph. Furthermore, the switched domains in the experiments discussed so far have a size of typically a few microns, compared to only tens of nanometers in current state-of-the-art hard disc drive technology. Entering the nanometer regime with all-optical magnetic recording is crucial from an industrial point of view, and simultaneously challenging from a scientific point of view. This issue will be discussed in Section 4.6.2.

#### 4.6.1 Enhanced Control of Magnetic Recording

Good control and reproducibility of magnetization reversal with a femtosecond laser pulse is essential in any possible application. The intensity window at which HD-AOS occurs is the most relevant parameter for possible applications of all-optical magnetic recording, as in this regime the final magnetic state is completely determined by the helicity of the excitation pulse, independent of its initial state. For such applications, however, it is necessary to overcome pulse-to-pulse fluctuations of the laser intensity to have fully controllable switching. Therefore, it is essential that the size of the intensity window, being equivalent to the MCD value, becomes much larger than the fluctuations of the laser intensity, which are currently more or less similar in value. The former could be readily enhanced by optimizing the design of the multilayer structure, even without changing the properties of the magnetic layer. As an example, we calculated the MCD in GdFeCo for different structures of the capping layer, see figure 4.9. In the calculations, the 60 nm thick SiN capping layer was replaced by SiN( $y$ )/amorphous-Si( $x$ )/SiN(5), where the values between parentheses represent the layer-thicknesses in nm. For  $y = 5$  and  $x = 40$  the window is more than doubled, i.e., from 1.5% to roughly 3.5%. Adjusting the material and/or thickness of other layers, including the magnetic layer, could enhance the intensity window even further.

#### 4.6.2 Towards the Nanoscale

The effective switching threshold  $F^* \approx 3 \text{ mJ/cm}^2$ , compares favorably with the  $2 \times 10^4 \text{ mJ/cm}^2$  of writing fluence per bit in current hard-disc drives and FLASH solid state memories [21]. The present switching area, however, is on the order of micrometers compared to tens of nanometers of bit size in state-of-the-art technology. Smaller switched areas can be obtained by reducing the spot size and (i) patterning the magnetic material [22, 23], or (ii) using a material with higher magnetic anisotropy [24]. Using the former technique, switched sizes of down to 200 nm were demonstrated [22] and we showed that due to interference the absorption is increased, making switching more energy efficient [23]. The patterned structures were realized

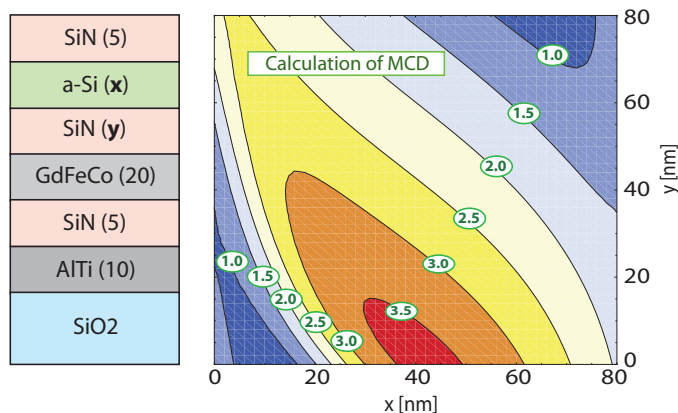


**Figure 4.9:** Calculation of the MCD in the GdFeCo layer (in percentages) at 700 nm for as a function of the thickness of the amorphous-Si (“x”) and SiN (“y”) layers. The complete multilayer structure with corresponding layer thicknesses is shown left.

via electron beam lithography in combination with a lift-off process, resulting in isolated magnetic structures with sizes ranging from  $1 \times 1 \mu\text{m}^2$  to  $100 \times 100 \text{ nm}^2$  [25]. This process, however, is very time consuming and the bit size is limited by the accuracy of the lift-off technique.

One way to circumvent this problem is by using a magnetic material with a high magnetic anisotropy which allows very small, but stable magnetic domains. For this purpose, we used TbFeCo because it has in many ways similar properties as GdFeCo, but it has a magnetic anisotropy which is two orders of magnitude larger. This property comes from the non-zero orbital moment of TbFeCo due to an additional electron in the 4f shell, giving rise to a large spin-orbit coupling.

As a proof of principle we used a  $\text{Tb}_{22}\text{Fe}_{69}\text{Co}_9$  thin film, with a coercive field of 1 T at room temperature (see Section 2.5.3). It was prepared in a state with large regions with magnetization “up” or “down”. These domains were irradiated with 800 nm laser pulses with a temporal width of 150 fs (FWHM) and a repetition rate of 60 Hz. Using confocal microscopy, the excitation pulses were focused on the sample surface to a typical size of  $2 \mu\text{m}$  in diameter. During the exposure, the sample was moved in the lateral direction across a domain wall so that each subsequent excitation pulse landed on a different spot on the sample surface.

Finally, we mapped the out-of-plane component of the local magnetization with sub-diffraction resolution ( $\approx 150 - 300 \text{ nm}$ ) by using “scanning near-field optical microscopy” (SNOM) [26] with magnetic sensitivity: the Faraday rotation of LP light transmitted through the film from a polarization-conserving hollow pyramid tip with

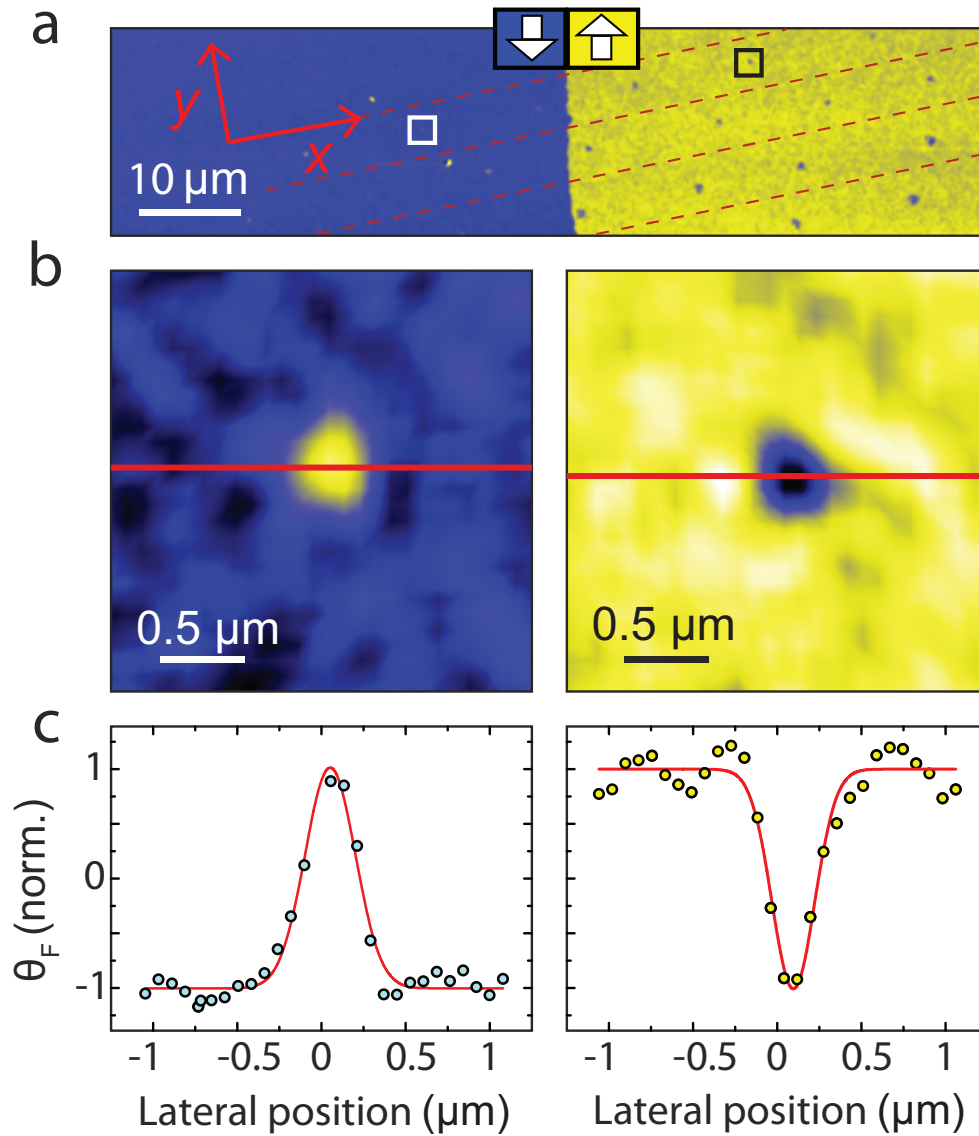


**Figure 4.10:** (a) Magneto-optical map of TbFeCo after exposure to laser pulses with a temporal width of 150 fs. Domains with magnetization “up” or “down” correspond to yellow or blue regions, respectively. Excitation pulses were swept along the x-direction with a spatial separation of  $10\ \mu\text{m}$ , and the excitation intensity was decreased along the y-direction. At intensities higher than  $5\ \text{mJ}/\text{cm}^2$ , a clear change of the magnetic state is observed. (b) High resolution scans of the areas indicated by the square frames in (a). (c) Lateral profile of the Faraday rotation ( $\theta_F$ ) measured along the lines in (b). The diameter of the switched domains is resolution-limited to 250 nm.

an aperture diameter of 100 nm was measured locally, and scanned over the sample surface. The MO-image of a large region is presented in figure 4.10a. The yellow and blue regions indicate magnetization “up” and “down”, respectively. The pulses were swept across the  $x$ -direction with a spatial separation of 10  $\mu\text{m}$ , and the excitation intensity was decreased along the  $y$ -direction. At intensities higher than 5  $\text{mJ}/\text{cm}^2$ , a clear change of the magnetic state is observed. A higher resolution of two selected regions for magnetization “up” and “down”, are presented in figure 4.10b. It can be seen that the magnetization of these spots is fully reversed by a single laser pulse. The size of the switched domains can be extracted from the lateral profile of the MO contrast along the red lines in figure 4.10b, as presented in figure 4.10c. From these profiles we estimate a size of 250 nm (FWHM) in diameter. This value corresponds to the spatial resolution of our technique, and therefore, the switched domain could be smaller. Furthermore, we found that at higher excitation intensities, not only the size of the perturbed magnetic region is changed. Instead, also the topological structure changes as a function of the fluence from a single domain (as in figure 4.10b), to a ring shaped domain, and even a single domain within a ring shaped domain [24]. The origin of these topological magnetic structures remains an intriguing issue, and goes beyond the scope of this thesis.

A higher spatial resolution is necessary to find the actual minimum size of the switched domains with AOS, and can be achieved by using x-rays instead of visible light to probe the magnetic domains. The minimum feasible magnetic bit size is defined by the width of the domain walls in the magnet. Using x-rays from the Linac Coherent Light Source at Stanford, it has been measured that the domain wall width of TbFeCo is smaller than 16 nm, which was the spatial resolution of the technique [27]. This gives the prospect of all-optical magnetic recording with competing bit sizes to today’s hard-disc drive technology. Therefore, together with the ultrafast switching time and low energy density per bit, all-optical magnetic recording could be a promising alternative to conventional recording technologies.

## 4.7 Summary

Summarizing, all-optical switching (AOS) with a single 55 fs laser pulse was studied as a function of light-polarization, -intensity, and -wavelength, in order to determine the role of light in this phenomenon. We come to the following conclusions:

- AOS in GdFeCo is subjected to a threshold fluence of  $2.6 \pm 0.2 \text{ mJ}/\text{cm}^2$  absorbed by the magnetic layer when excited with an ultrashort optical laser pulse, independent of either the wavelength or the polarization of the excitation pulse. This reveals that the role of light in AOS is ultrafast heating of the magnetic material.

- Helicity dependent AOS, formerly assigned to the inverse Faraday effect, is a natural consequence of magnetic circular dichroism. This explanation is in *quantitative* agreement with our experiments, and is shown to be consistent with all experimental findings on helicity dependent AOS so far, varying from single- to multiple-shot experiments.
- This new understanding enables the possibility to design multilayer structures with an enhanced intensity window in which helicity dependent AOS occurs, which could be relevant for the application of all-optical magnetic recording.
- We have successfully decreased the switched domain size from a few microns to less than 250 nm, with the prospect of achieving sub-100 nm domains. This is achieved by replacing GdFeCo by TbFeCo, a material which is known for its high anisotropy, and confining the excitation pulse with a confocal microscope.

## References

- [1] E. Beaurepaire, J. C. Merle, A. Daunois, and J. Y. Bigot, *Physical Review Letters* **76**, 4250 (1996).
- [2] B. Koopmans, M. van Kampen, J. T. Kohlhepp, and W. J. M. de Jonge, *Physical Review Letters* **85**, 844 (2000).
- [3] C. D. Stanciu, F. Hansteen, A. V. Kimel, A. Kirilyuk, A. Tsukamoto, A. Itoh, and T. Rasing, *Physical Review Letters* **99**, 047601 (2007).
- [4] A. Kirilyuk, A. V. Kimel, and T. Rasing, *Reviews of Modern Physics* **82**, 2731 (2010).
- [5] K. Vahaplar, A. M. Kalashnikova, A. V. Kimel, D. Hinzke, U. Nowak, R. Chantrell, A. Tsukamoto, A. Itoh, A. Kirilyuk, and T. Rasing, *Physical Review Letters* **103**, 117201 (2009).
- [6] A. V. Kimel, A. Kirilyuk, P. A. Usachev, R. V. Pisarev, A. M. Balbashov, and T. Rasing, *Nature* **435**, 655 (2005).
- [7] F. Hansteen, A. Kimel, A. Kirilyuk, and T. Rasing, *Physical Review Letters* **95**, 047402 (2005).
- [8] F. Hansteen, A. Kimel, A. Kirilyuk, and T. Rasing, *Physical Review B* **73**, 014421 (2006).
- [9] T. Satoh, S. J. Cho, R. Iida, T. Shimura, K. Kuroda, H. Ueda, Y. Ueda, B. A. Ivanov, F. Nori, and M. Fiebig, *Physical Review Letters* **105**, 077402 (2010).
- [10] E. D. Palik, ed., *Handbook of optical constants of solids II* (Academic Press, San Diego, 1998).
- [11] J. A. Arnaud, W. M. Hubbard, Mandevil.Gd, B. D. Claviere, E. A. Franke, and J. M. Franke, *Applied Optics* **10**, 2775 (1971).
- [12] J. M. Liu, *Optics Letters* **7**, 196 (1982).
- [13] J. Chalupsky, L. Juha, J. Kuba, J. Cihelka, V. Hajkova, S. Koptyaev, J. Krasa, A. Velyhan, M. Bergh, C. Coleman, et al., *Optics Express* **15**, 6036 (2007).
- [14] A. R. Khorsand, R. Sobierajski, E. Louis, S. Bruijn, E. D. van Hattum, R. W. E. van de Kruijs, M. Jurek, D. Klinger, J. B. Pelka, L. Juha, et al., *Optics Express* **18**, 700 (2010).
- [15] J. van der Ziel and P. Pershan, *Physical Review Letters* **15**, 190 (1965).

- 
- [16] P. S. Pershan, J. P. van der Ziel, and L. D. Malmstro, *Physical Review* **143**, 574 (1966).
- [17] J. H. Mentink, J. Hellsvik, D. V. Afanasiev, B. A. Ivanov, A. Kirilyuk, A. V. Kimel, O. Eriksson, M. I. Katsnelson, and T. Rasing, *Physical Review Letters* **108**, 057202 (2012).
- [18] T. A. Ostler, J. Barker, R. F. L. Evans, R. W. Chantrell, U. Atxitia, O. Chubykalo-Fesenko, S. El Moussaoui, L. Le Guyader, E. Mengotti, L. J. Heyderman, et al., *Nature Communications* **3**, 666 (2012).
- [19] I. Radu, K. Vahaplar, C. Stamm, T. Kachel, N. Pontius, H. A. Durr, T. A. Ostler, J. Barker, R. F. L. Evans, R. W. Chantrell, et al., *Nature* **472**, 205 (2011).
- [20] D. Steil, S. Alebrand, A. Hassdenteufel, M. Cinchetti, and M. Aeschlimann, *Physical Review B* **84**, 224408 (2011).
- [21] J. P. Liu, E. Fullerton, O. Gutfleisch, and D. Sellmyer, *Nanoscale Magnetic Materials and Applications* (Springer-Verlag, New York, 2009).
- [22] L. Le Guyader, S. El Moussaoui, M. Buzzi, R. V. Chopdekar, L. J. Heyderman, A. Tsukamoto, A. Itoh, A. Kirilyuk, T. Rasing, A. V. Kimel, et al., *Applied Physics Letters* **101**, 022410 (2012).
- [23] M. Savoini, R. Medapalli, B. Koene, A. R. Khorsand, L. Le Guyader, L. Duo, M. Finazzi, A. Tsukamoto, A. Itoh, F. Nolting, et al., *Physical Review B* **86**, 140404 (2012).
- [24] M. Finazzi, M. Savoini, A. R. Khorsand, A. Tsukamoto, A. Itoh, L. Duo, A. Kirilyuk, A. Kimel, T. Rasing, and M. Ezawa, submitted (2012).
- [25] L. Le Guyader, S. El Moussaoui, E. Mengotti, L. J. Heyderman, F. Nolting, A. Tsukamoto, A. Itoh, A. Kirilyuk, T. Rasing, and A. V. Kimel, *Journal of the Magnetism Society of Japan* **36**, 21 (2012).
- [26] P. Biagioni, J. S. Huang, L. Duo, M. Finazzi, and B. Hecht, *Physical Review Letters* **102**, 256801 (2009).
- [27] M. Savoini, *private communication* (2012).



## CHAPTER 5

---

### Element Specific Probing of Ultrafast Spin Dynamics in Multi-Sublattice Magnets with Visible Light<sup>1</sup>

---

*“X-rays will turn out to be a hoax.”*

LORD KELVIN, 1897

---

<sup>1</sup>In part adapted from: A. R. Khorsand, M. Savoini, A. Kirilyuk, A. V. Kimel, A. Tsukamoto, A. Itoh, and Th. Rasing, “Element Specific Probing of Ultrafast Spin Dynamics in Multi-Sublattice Magnets with Visible Light,” (submitted).

## 5.1 Introduction

Femtosecond laser excitation of multi-sublattice magnets opens the way to trigger ultrafast spin dynamics and even magnetization reversal driven by the strong exchange interaction between the sublattices [1, 2]. To explore and exploit these intriguing possibilities requires femtosecond time-resolved and element specific studies of the spin dynamics in multi-sublattice systems.

The wavefunctions of the magnetic states in metals probed in the visible spectral range have, in general, a substantial overlap. This fact has been a serious obstacle for experimental studies of element specific ultrafast magnetization dynamics. Until now it has been a conventionally accepted wisdom that ultrafast and element specific probing of magnetism in the visible spectral range is hardly possible and only photons in the soft x-ray [2, 3] and EUV [4] regimes were used for such studies, probing transitions of strongly localized electrons of which their exchange split core levels serve as the fingerprint of the element.

Techniques utilizing high energy photons have, however, considerable limitations, in particular in combination with sub-picosecond time resolution. For instance, the number of photons per pulse is small and subject to fluctuations, giving rise to an extremely low signal-to-noise ratio and time-consuming measurements. Furthermore, the generation of soft x-ray fs pulses requires rather unique and demanding sources, and the access to such facilities is very limited. Therefore, despite all the interest in ultrafast magnetization dynamics, very few element specific studies have been published so far.

In this chapter, we formulate requirements which allow element specific probing in the visible spectral range. We study ultrafast laser-induced magnetization dynamics of a TbFe alloy, and find that one can selectively study the dynamics of Tb- and Fe-spins choosing the wavelength of light below and above 610 nm, respectively. Furthermore, we find that at high excitation intensities the antiferromagnetically coupled spins temporarily align ferromagnetically. The magnetization of the Tb sublattice demagnetizes at an accelerated rate in this meta-stable state, and becomes almost fully quenched. The antiparallel alignment of Tb and Fe is, however, restored by the fast recovery of the magnetization of Fe. Therefore, TbFe relaxes back to its initial state. Finally, it is discussed how element specific probing in the visible range can be generalized to other two-sublattice magnets.

An ideal sample for the study of element specific probing with visible light, is a magnet which consist of two elements of which their magneto-optical (MO) responses have very different spectral dependencies in the (near-)visible spectral range. This makes RE-TM alloys in general an interesting group of magnetic samples for this study: The magnetic moment of TM is carried by conduction near the Fermi level, whereas most magnetic moment of the RE is carried by localized 4f electrons at typically a few eV below Fermi level. Because the magnetic moments of the TM and

RE metal are carried by electrons at very different energies, the MO responses of the TM and RE have different spectral dependencies. Transition metals are characterized by a relatively large Kerr rotation in the infrared regime, whereas for the RE elements a large Kerr rotation is expected at energies allowing transitions from the 4f shell to the conduction band. It can be seen from Table 2.2 that the 4f energy level of many RE are lower than several eV. Therefore, with the exception of Gd, they can be probed with an optical or near-UV probe. In particular, terbium appears to be a good candidate to be used for an optical study, as the 4f shell is at 2.4 eV (corresponding to light with  $\lambda = 500$  nm).

## 5.2 Sample Properties

The feasibility of element specific spin dynamics with visible light is investigated on a TbFe based alloy. The sample structure is glass-ALTi(10)-Si<sub>3</sub>N<sub>4</sub>(5)-TbFeCo(20)-Si<sub>3</sub>N<sub>4</sub>(60). The magnetic material is an amorphous, thin ferrimagnetic film of 20 nm. The composition is 16% Tb, 75% Fe, and 9% Co, with an out-of-plane anisotropy and a coercive field of 1 T. The magnetic moments of Tb and Fe(Co) form two anti-ferromagnetically coupled sublattices with similar, though non-equivalent, magnetic moments (see Tables 2.1 and 2.2). The most part of the magnetic moment of Tb is carried by electrons in the 4f shell at 2.4 eV below the Fermi energy (corresponding to  $\lambda = 500$  nm), whereas the magnetic moment of Fe(Co) is carried by the conduction electrons near the Fermi energy and can be accessed with infrared light. The spectral dependence of the refractive index of TbFeCo, extracted from ellipsometry measurements, is presented in figure 3.10. The sample was excited with an ultrashort pulse at a wavelength of 400 nm from either the front or back side of the sample, which will be further discussed in the next Section. The absorption profile in the sample for these two geometries is presented in figure 5.1. It can be seen that a large fraction of the photon energy is absorbed in the ALTi layer when the excitation pulse is incident to the back side of the sample. If a maximum excitation of the magnetic layer is desired, the pump beam should be incident to the front side of the material.

In the following, we focus on the behavior of Tb and Fe and ignore the small contribution of angular momentum of Co.

## 5.3 Experimental Details

Both static- and time resolved (TR) MOKE measurements [5–9] are performed at room temperature. We use regeneratively amplified pulses from a Ti:sapphire laser at a repetition rate of 1 kHz as explained in Section 3.3.1. A polar geometry is employed, i.e., the probe is at normal incidence, and the rotation of the plane of polarization of the reflected beam is measured. A constant external magnetic field of  $\pm 1.2$  T (larger

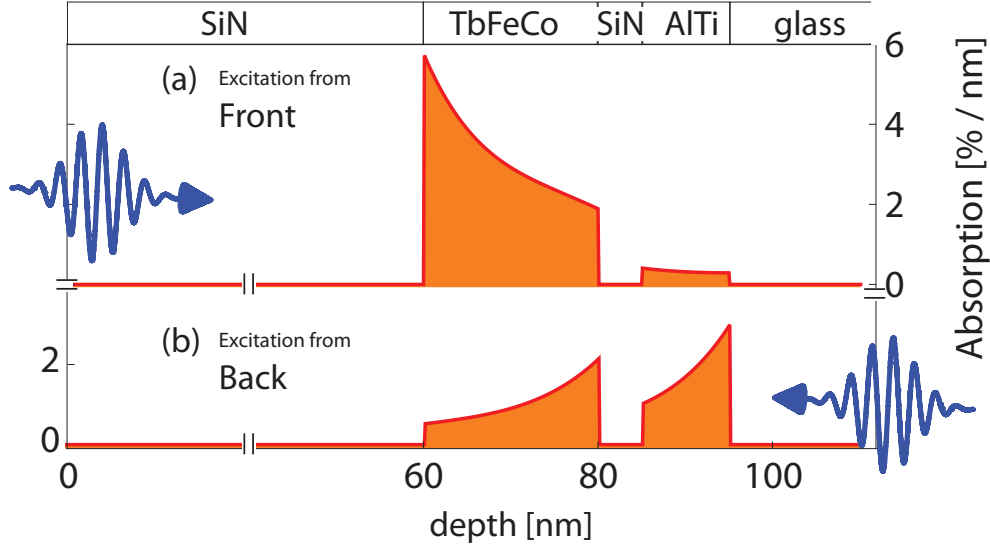


**Figure 5.1:** Absorption profile of the TbFeCo sample for linearly polarized 400 nm light at normal incidence to the (a) front-, and (b) backside of the sample. It can be seen that the absorption in the AlTi layer becomes significant when the sample is excited from the backside.

than the coercive field) was applied during the TR-MOKE measurements. This field brings the magnetic material back to its initial state before the next excitation pulse arrives. We define the Kerr rotation as the difference in rotation of linearly polarized light for positive and negative magnetization, i.e.,  $\theta_K = \theta_{+M} - \theta_{-M}$ . This ensures that  $\theta_K$  is of a purely magnetic origin. The radius of the pump and probe pulses are 140 and 45  $\mu\text{m}$ , respectively. Due to the large difference in the pump and probe dimensions the probed area is homogeneously heated. The pump wavelength was fixed at 400 nm. Due to space limitations at this relatively high magnetic field, the pump and probe beams are incident to opposite sides of the sample (see Section 3.3.2).

Two sets of TR-MOKE measurements are performed. The probe-wavelength is varied ( $\lambda = 400 - 950$  nm) at a fixed pump intensity in the first series. In order to achieve maximum signal-to-noise ratio, the probe is incident from the front of the sample, and the pump from the back (substrate) side. From these measurements we demonstrate the feasibility of TR-MOKE with element specificity at 500 and 800 nm for the Tb and Fe sublattices, respectively.

Subsequently, the sublattice dynamics of Tb and Fe are studied in more detail as a function of the excitation intensity in the second series of TR-MOKE measurements. The probe wavelength is set to 500 or 800 nm, depending on the sublattice under

study. The pump pulse is incident to the front side of the sample in order to achieve maximum excitation of the magnetic material (see figure 5.1). The excitation intensity is varied up to 7 mJ/cm<sup>2</sup>. Permanent structural changes of the magnetic layer occur at intensities higher than 8 mJ/cm<sup>2</sup>.

## 5.4 Spectroscopic Measurements

The spectral dependence of the static Kerr rotation  $\theta_{K,0}$ , i.e., the Kerr rotation of TbFe in the absence of an excitation pulse, is shown in figure 5.2a. The spectrum contains three important features: (i) a small but positive signal in the (infra)red regime, (ii) a sign change around 610 nm, and (iii) a large and relatively sharp peak around 500 nm.

In a material with two magnetic sublattices, the Kerr rotation consists of the collective response of both magnetic species. In an isotropic medium in a polar geometry (see inset of figure 5.3b) the Kerr rotation is in first order approximation given by [11, 12]:

$$\theta_K(\lambda) = \theta_1(\lambda) + \theta_2(\lambda) = K_1(\lambda)M_1 + K_2(\lambda)M_2, \quad (5.1)$$

where  $\theta_i$ ,  $M_i$  and  $K_i$  are the Kerr rotation, out-of-plane component of the magnetization, and MO susceptibility of sublattice  $i$ , respectively. The probe-sensitivity  $\alpha_i$  to sublattice  $i$  is defined with

$$\alpha_i(\lambda) = \frac{|\theta_i(\lambda)|}{|\theta_{\text{Tb}}(\lambda)| + |\theta_{\text{Fe}}(\lambda)|}. \quad (5.2)$$

$K_{\text{Fe}}$  and  $K_{\text{Tb}}$  have the same sign and do not reverse at  $\lambda = 400 - 950$  nm [11, 12], whereas  $M_{\text{Fe}}$  and  $M_{\text{Tb}}$  have opposite signs due to the antiferromagnetic coupling. Therefore, the Kerr rotations of the Tb and Fe sublattices ( $\theta_i = K_i M_i$ ) are opposite to each other. When their magnitudes are equivalent, i.e.,  $\alpha_{\text{Fe}} = \alpha_{\text{Tb}} = 0.5$ , the net Kerr rotation of TbFe goes to zero. This is the case around 610 nm. Above and below this wavelength, the sign of the net Kerr rotation is given by the sublattice with the dominant contribution to the MO contrast, i.e., the sublattice for which  $\alpha_i > 0.5$ . We identify the wavelength regimes above and below 610 nm as the Fe and Tb dominated regimes, respectively.

In magnetic TM's (e.g., Fe, Ni, and Co), the magnetic moment is carried by itinerant 3d electrons near the Fermi energy ( $E_{\text{F}}$ ). Due to the many possible low-energy transitions within the conduction band of these ferromagnets, their Kerr rotations are significant in the infrared (IR) regime. For example,  $K_{\text{Fe}}(\lambda)$  is non-zero in the optical regime and increases towards the near-IR [13]. On the other hand, the largest part of the magnetic moment of RE metals (about 97% for Tb) is carried by the localized 4f electrons [10, 14, 15]. The other 3% is carried by 5d conduction electrons. Spin-polarized XPS data of Tb is shown in figure 5.2a (adapted from [10]), from which we

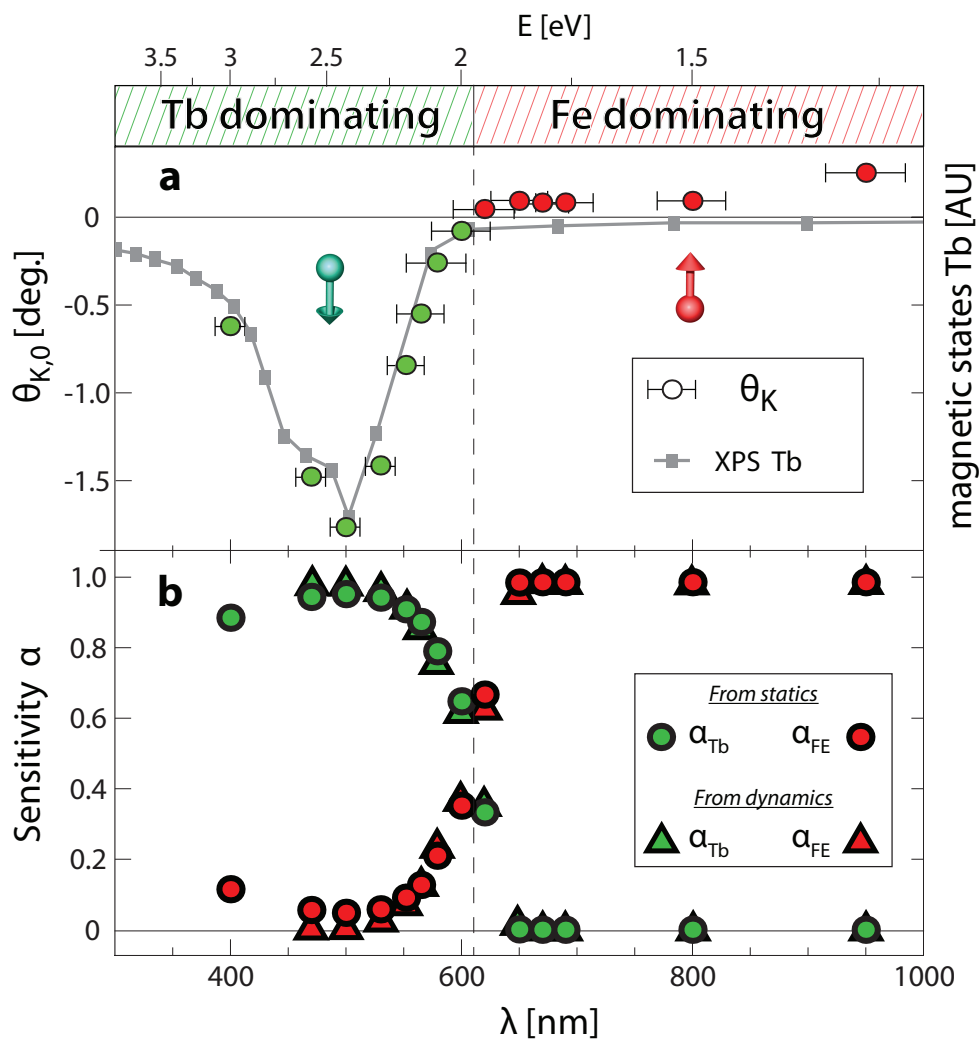


**Figure 5.2:** Magneto-optical response of the TbFe-alloy as a function of the probe wavelength (bottom axis) and photon energy (top axis). (a) The static Kerr rotation (dots), and the magnetic states in the 4f shell of Tb (connected squares). The latter was measured with spin polarized X-ray photoemission spectroscopy (XPS) and is adapted from ref. [10]. (b) The sensitivity  $\alpha$  to Fe (red) and Tb (green) sublattices obtained from static- (dots) and TR-MOKE (triangles) measurements.

find that the 4f shell is at around 2.4 eV below  $E_F$ . The 4f electrons of Tb become accessible in the visible spectral range, and also the conduction electrons are accessible at 2-3 eV [16]. This gives rise to a high Kerr rotation of the Tb sublattice in this regime. In fact, it can be seen from the XPS data in figure 5.2a that the large peak of the Kerr rotation around 500 nm is closely related to the peak of spin-polarized states of Tb, indicating that the MO response comes mainly from Tb.

### 5.4.1 Spectroscopic TR-MOKE

The wavelength dependence of the MO response of TbFe is studied in more detail with TR-MOKE measurements at a fixed excitation fluence of 4.4 mJ/cm<sup>2</sup>. First, we consider the dynamics in the regime  $\lambda \geq 650$  nm shown in figure 5.3a. The normalized transient Kerr rotation, i.e.,  $\tilde{\theta}_K(\lambda, t) \equiv \frac{\theta_K(\lambda, t)}{\theta_{K,0}(\lambda)}$ , is plotted as a function of the pump-probe delay time for various probe wavelengths. It can be seen that for  $\lambda > 650$  nm the MO response is independent of the probe wavelength, which demonstrates that the sensitivities  $\alpha_{Fe}$  and  $\alpha_{Tb}$  are constant in this wavelength regime.

At shorter wavelengths, the probe is sensitive to more than one sublattice. Otherwise, the magnetization dynamics  $M_i(t)/M_0$  of sublattice  $i$  would be given by  $\theta_K(t)/\theta_{K,0}$ , and the measurements at 565-600 nm would have the unphysical implication that the absolute value of the magnetic moment increases shortly after excitation. On the other hand, if the measurements give the collective response of two sublattices, it should be possible to reproduce all profiles from two traces, i.e., from the Tb and Fe dominated responses at 500 and 800 nm, respectively. We can examine this by fitting the dynamics measurements to the following function:

$$\theta_{\text{fit}}(\lambda, t, \alpha_1) = \theta_{K,0}(\lambda) \times \frac{(1 - \alpha_{Tb})\tilde{\theta}_{Fe}(t) - \alpha_{Tb}\tilde{\theta}_{Tb}(t)}{1 - 2\alpha_{Tb}}, \quad (5.3)$$

where  $\theta_{K,0}(\lambda)$  is the static Kerr rotation taken from figure 5.2a, and  $\tilde{\theta}_{Tb}(t)$  and  $\tilde{\theta}_{Fe}(t)$  are the normalized time resolved Kerr rotations at 500 nm and 800 nm, respectively. The denominator  $1 - 2\alpha_{Tb}$  ensures that the righthand term is normalized to +1 at  $t < 0$ . We note that we use only one fitting parameter, namely  $\alpha_{Tb}$ , in order to fit the whole set of time-dependencies at probe wavelength  $\lambda$ . The fits are shown in figure 5.3b as solid blue lines. The sensitivity to the Tb sublattice is presented at the right side of the figure for each probe-wavelength. It can be seen that the thus obtained fits are in excellent agreement with the TR-MOKE measurements. This demonstrates that there are only two traces that give rise to the TR-MOKE measurements at  $\lambda = 500 - 950$  nm, and validates Eq. 5.1 in this wavelength range.

Having demonstrated that we can readily measure different parts of the magnetization of TbFe by changing the probe wavelength, we have a closer look at the MO responses at 500 nm and 800 nm. The demagnetization profiles show features which are typical for Fe and Tb. The demagnetization at 800 nm is ultrafast ( $\tau \approx 0.2$  ps),

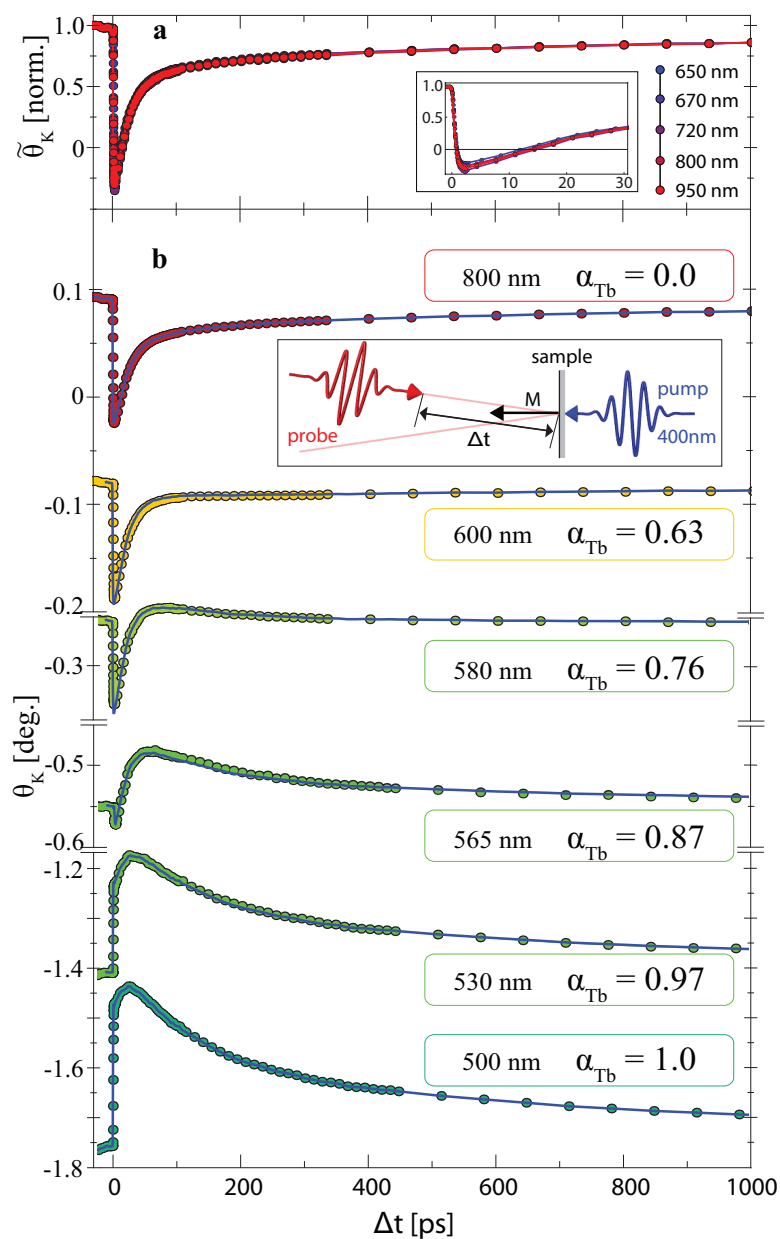


**Figure 5.3:** Spectral dependence of TR-MOKE measurements at a fixed excitation fluence of  $4.4 \text{ mJ/cm}^2$ . TR-MOKE at (a)  $\lambda = 650\text{--}950 \text{ nm}$ , and (b)  $\lambda = 500\text{--}800 \text{ nm}$ . The blue solid lines in (b) are the fits to Eq. 5.3, where the fitting parameters  $\alpha_{Tb}$  are given at the right at each wavelength. Inset: Geometry of the pump-probe pulses with respect to the sample.



succeeded by a recovery. Such “one-step demagnetization” is typical for 3d TM’s like Fe [5–8]. On the other hand, at 500 nm the drop of the MO signal is initially ultrafast ( $\tau \approx 0.4$  ps), succeeded by a slower demagnetization ( $\tau \approx 15$  ps) before it recovers. Such “two-step demagnetization” is typical for RE metals such as Tb [7, 17], and is generally assigned to their large magnetic moments. Therefore, the TR-MOKE measurements at 500 nm and 800 nm reveal fingerprints of the Tb and Fe sublattices, respectively. This is in agreement with the static MOKE measurements shown in figure 5.2a from which we concluded that the probe is sensitive to dominantly the Tb and Fe sublattice at wavelengths below and above 610 nm, respectively.

Apart from a different shape of the demagnetization profile, there is a large difference in the change in the MO contrast. The maximum change of the MO contrast is much smaller at 500 nm ( $\approx 20\%$ ) compared to 800 nm ( $> 100\%$ ). At an excitation intensity of  $6 \text{ mJ/cm}^2$ , shown in figure 5.4, these values are 95% and 150%, respectively.

The magnetization dynamics of each sublattice can be extracted from the TR-MOKE measurements once the probe sensitivity to each sublattice is known at 500 nm and 800 nm. For TbFe, we can estimate the probe sensitivity to the Fe and Tb sublattices as their magnetization is largely contained at different energy levels. We can use the static MOKE measurements presented in figure 5.2a in combination with the fact that the Kerr rotation of pure Fe decreases only little in the regime  $\lambda < 650$  nm [13]. Using  $\theta_{\text{Fe}}(\lambda) \leq 90$  mdeg, the sensitivity to the Tb sublattice at  $\lambda = 400\text{--}650$  nm can be readily calculated with Eq. 5.2, and is shown in figure 5.2b. We find that at 500 nm almost all signal comes from Tb, i.e.,  $\alpha_{\text{Tb}} > 0.95$ . Furthermore, we find that these sensitivities are in excellent agreement with the fitted values from the dynamics measurements shown in figure 5.3b.

On the other hand, TR-MOKE measurements have revealed that at longer wavelengths (650 – 950 nm) the sensitivities  $\alpha_{\text{Tb}}$  and  $\alpha_{\text{Fe}}$  are constant. In this low energy regime, MO properties arise from transitions within the conduction band. Transition metals such as Fe have a relatively large MO susceptibility in this regime as their magnetic moments are contained within the conduction band. The Tb sublattice can also contribute to the Kerr rotation in the IR regime through the 5d conduction electrons which carry approximately 3% of the magnetic moment. The Kerr rotation of Tb, however, is typically very small compared to Fe. We measured the Kerr rotations of 20 nm thin Tb and Fe films at 800 nm to be  $\theta_{\text{Tb}} \approx 10$  mdeg (at 100 K) and  $\theta_{\text{Fe}} \approx 350$  mdeg, respectively. We estimate from this that the contribution of Tb to the MO signal of TbFe is very small ( $\approx 3\%$ ) in the IR regime, and that  $\alpha_{\text{Fe}} \approx 1$ .

It should be noted that the relative Kerr rotations of Tb and Fe in alloys may deviate from their pure forms. Using Eq. 5.3, we calculated the sublattice magnetization dynamics of Fe from  $\theta_{\text{K}}(t, 800\text{nm})$  for  $0 < \alpha_{\text{Tb}} < 0.5$ . It can be seen that even under the conservative assumption that  $\alpha_{\text{Fe}} = 0.65$  ( $\alpha_{\text{Tb}} = 0.35$ ), the TR-MOKE measurement at 800 nm indicate that the magnetization of Fe temporarily reverses

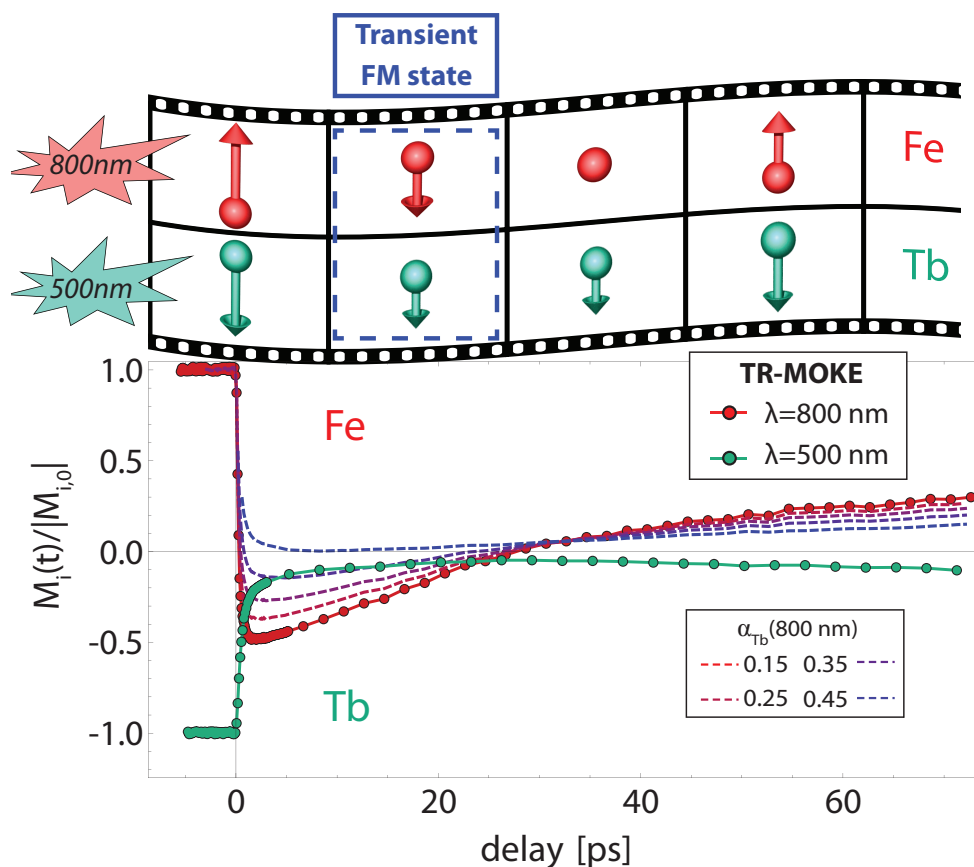


**Figure 5.4:** Ultrafast sublattice magnetization dynamics of TbFe at  $\lambda_{Fe} = 800 \text{ nm}$  and  $\lambda_{Tb} = 500$ , corresponding to dominantly the Fe and Tb sublattices, respectively. The excitation fluence was  $6 \text{ mJ/cm}^2$ . It can be seen that the system is temporarily in a ferromagnetic (FM) state just after excitation. In the case the MO response at 800 nm comes from the Fe sublattice only ( $\alpha_{Tb}(800 \text{ nm})=0$ ), then the TR-MOKE measurements at  $\lambda = 800 \text{ nm}$  give directly the magnetization dynamics of Fe. In the case Tb contributes to the MOKE signal at 800 nm, the magnetization dynamics of Fe can be obtained from a superposition of the TR-MOKE measurements at 800 nm and 500 nm, as explained in the text. The dashed lines represent the magnetization dynamics of Fe for various probe-sensitivities to Tb at 800 nm.

sign.

### 5.4.2 Transient Ferromagnetic State

The reversal of the Fe sublattice leads to a transient ferromagnetic state: a magnetic state in which both sublattices are temporarily aligned ferromagnetically, despite their antiferromagnetic coupling in the ground state. Such transient ferromagnetic state was recently discovered in GdFeCo [2], which has an antiferromagnetic coupling in its ground state too. It was demonstrated that this meta-stable state is a necessary and sufficient condition for all-optical magnetization reversal in GdFeCo [2, 18, 19], i.e., the reversal of both magnetic sublattices with a single laser pulse [1, 20]. In TbFeCo, however, we observe a different behavior; the transient ferromagnetic state is succeeded by the recovery of the magnetization.

The striking difference in the dynamics of TbFeCo and GdFeCo may be explained by the large difference in spin-orbit coupling and consequently the anisotropy in the two RE materials. Gadolinium has an exactly half-filled 4f shell. Therefore, its net orbital moment is zero and the spin-orbit coupling is very weak. As a consequence, the spins of the Gd atoms are coupled only weakly to the lattice, allowing them to follow the Fe spins relatively easily. Terbium on the other hand, is known for its strong spin-orbit coupling and anisotropy. This is the origin of the large coercive field ( $\mu_0 H_C \approx 1$  T) of TbFeCo, which is 2 orders of magnitude larger than for GdFeCo. Therefore, Tb spins are not only coupled to the spins of the Fe sublattice, but also to the lattice. This leads to two competing forces acting on the Tb spins. So far, multi-sublattice dynamics is described with a Hamiltonian which takes into account the spin-spin interactions, and neglects the anisotropy due to the spin-orbit coupling [18, 19]. This approximation is valid for Gd-TM alloys due to the small anisotropy in Gd. However, for an adequate description of the dynamics of other 4f RE metals such as Tb, the anisotropy can not be ignored and should be included in the Hamiltonian.

### 5.4.3 Generalization of Element Specific Probing with Visible Light

Element specific probing of two-sublattice magnets could be generalized to other magnetic alloys. We rewrite Eq. 5.3 for a two-sublattice magnet with either parallel or antiparallel MO coupling at  $\lambda_1$  and  $\lambda_2$ :

$$\theta_K(t, \lambda_i) = \theta_{K,0}(\lambda_i) \times \frac{\alpha_{\lambda_i} \widetilde{M}_1(t) \pm \beta_{\lambda_i} \widetilde{M}_2(t)}{\alpha_{\lambda_i} \pm \beta_{\lambda_i}}, \quad (5.4)$$

with  $\alpha$  and  $\beta$  the probe-sensitivity to sublattice 1 and 2, respectively, where  $\alpha + \beta = 1$ , and  $\widetilde{M}_i(t)$  the normalized magnetization of sublattice  $i$ . The plus or minus sign depends on the MO-coupling of the sublattices. The sign is positive if the Kerr rotation of both sublattices is in the same direction, whereas opposite Kerr rotations (e.g., in

the case of TbFe) lead to a negative sign. In general, TR-MOKE measurements give the collective responds of both magnetic sublattices, and the challenge is to extract  $\widetilde{M}_1(t)$  and  $\widetilde{M}_2(t)$  from these measurements.

On the other hand, TR-XMCD measurements give the pure response of sublattice  $i$  if the x-ray energy is tuned to an absorption edge of that element. From such measurements  $\widetilde{M}_i(t)$  is directly obtained. Hence, by performing (i) TR-XMCD measurements at the absorption-edges of both sublattices, and (ii) TR-MOKE measurements at  $\lambda_1$  and  $\lambda_2$  under similar conditions, then the probe-sensitivities to each sublattice at these optical wavelengths can be obtained from Eq. 5.4. Once a single calibration measurement is performed and  $\alpha$  and  $\beta$  are known, TR-MOKE measurements at  $\lambda_1$  and  $\lambda_2$  give full information about ultrafast sublattice dynamics of each sublattice at any excitation conditions.

It can be readily shown from Eq. 5.4 that the normalized magnetization dynamics of sublattice  $i$  and TR-MOKE measurements at  $\lambda_1$  and  $\lambda_2$  are related by the following expression if the MO kerr rotations of the sublattices have opposite signs:

$$\widetilde{M}_1(t) = \frac{\beta_{\lambda_2}(1 - 2\beta_{\lambda_1})}{\beta_{\lambda_2} - \beta_{\lambda_1}} \widetilde{\theta}_K(\lambda_1, t) - \widetilde{\theta}_K(\lambda_2, t) \frac{\beta_{\lambda_1}(1 - 2\beta_{\lambda_2})}{\beta_{\lambda_2} - \beta_{\lambda_1}}, \quad (5.5)$$

$$\widetilde{M}_2(t) = \frac{(\beta_{\lambda_2} - 1)(1 - 2\beta_{\lambda_1})}{\beta_{\lambda_2} - \beta_{\lambda_1}} \widetilde{\theta}_K(\lambda_1, t) - \widetilde{\theta}_K(\lambda_2, t) \frac{(\beta_{\lambda_1} - 1)(1 - 2\beta_{\lambda_2})}{\beta_{\lambda_2} - \beta_{\lambda_1}}, \quad (5.6)$$

On the other hand, if the Kerr rotations of the sublattices have the same sign, the relations are given by

$$\widetilde{M}_1(t) = \frac{\beta_{\lambda_2}}{\beta_{\lambda_2} - \beta_{\lambda_1}} \widetilde{\theta}_K(\lambda_1, t) - \frac{\beta_{\lambda_1}}{\beta_{\lambda_2} - \beta_{\lambda_1}} \widetilde{\theta}_K(\lambda_2, t), \quad (5.7)$$

$$\widetilde{M}_2(t) = \frac{\beta_{\lambda_2} - 1}{\beta_{\lambda_2} - \beta_{\lambda_1}} \widetilde{\theta}_K(\lambda_1, t) - \frac{\beta_{\lambda_1} - 1}{\beta_{\lambda_2} - \beta_{\lambda_1}} \widetilde{\theta}_K(\lambda_2, t). \quad (5.8)$$

These relations demonstrate that pure sublattice dynamics can be obtained from a superposition of TR-MOKE measurements at  $\lambda_1$  and  $\lambda_2$ , once the probe-sensitivities  $\alpha$  and  $\beta$  are known at  $\lambda_1$  and  $\lambda_2$  from a single calibration with TR-XMCD measurements. The only requirement for the feasibility of sublattice magnetization dynamics measurements with visible light is that the probe sensitivities to the two sublattices are different at the two probe-wavelengths, i.e.,  $\beta_{\lambda_2} - \beta_{\lambda_1} \neq 0$ . Furthermore, it can be seen that in the limit  $\beta_{\lambda_1} = 0$  and  $\beta_{\lambda_2} = 1$  (which is approximately the case for TbFe), the normalized TR-MOKE measurements at  $\lambda_1$  and  $\lambda_2$  correspond to the magnetization dynamics of sublattice 1 and 2, respectively.

Once the probe-sensitivities are extracted from the calibration measurements, sublattice dynamics can be studied with visible light at different conditions, such as different excitation intensities or magnetic fields. After the calibration with high en-

ergy photons, this procedure allows all-optical element specific measurements with the unique advantages of an optical probe.

#### 5.4.4 Comparison with Conventional Element Specific Techniques

Element specific probing with visible light has unique advantages compared to techniques utilizing high-energy photons [2–4], such as (i) superior signal-to-noise ratio due to the high photon flux, (ii) much less time-consuming and demanding measurements, (iii) no need for a vacuum environment in which it is hard to access or adjust optical components, (iv) no need to work with unique sources with limited access or to buy expensive tools for the generation of high energy photons, and (v) the use of non-ionizing photons. Unique advantages of XMCD measurements are the possibilities to resolve the spin and orbital angular moments [21], and to have a spatial resolution of only several nm. For experimental studies where the orbital and spin moments of each sublattice should be distinguishable, visible light can not serve as an alternative to x-ray measurements. However, if the magnetic moment is of interest and the sublattices of the magnetic system have substantially different wavelength dependent Kerr rotations, then the advantages of visible light allow much more accurate and faster studies than conventional x-ray techniques.

### 5.5 Fluence Dependent Measurements

Having demonstrated the feasibility of element specific probing with an ultrashort optical laser pulse and the existence of a transient ferromagnetic state at high excitation intensities in TbFe alloy, we will have a closer look at the sublattice dynamics at highly excited states. The pump pulse is incident to the front of the sample, and its intensity is varied up to  $7 \text{ mJ/cm}^2$ , while a static magnetic field of  $\pm 1.2 \text{ T}$  was applied along the easy-axis to saturate the magnetization in either “up” or “down” direction. The dependencies of the Tb and Fe sublattice dynamics to the pump fluence is presented in figure 5.5. It can be seen that at any pump fluence the Fe sublattice shows ultrafast demagnetization, succeeded by a recovery. The magnitude of the demagnetization of Fe is linearly dependent of the fluence until it saturates around  $-0.5M_0$ . On the other hand, the dynamics of Tb seems more complex. At low intensities, the ultrafast demagnetization is initially followed by a recovery, before a second and much slower demagnetization process sets in at  $t \approx 5 \text{ ps}$ . The magnitude of the second demagnetization is relatively small at low intensities, but increases rapidly at higher intensities compared to the initial and ultrafast demagnetization. As a consequence, the recovery between the two stages of demagnetization disappears at intensities higher than about  $4 \text{ mJ/cm}^2$ .

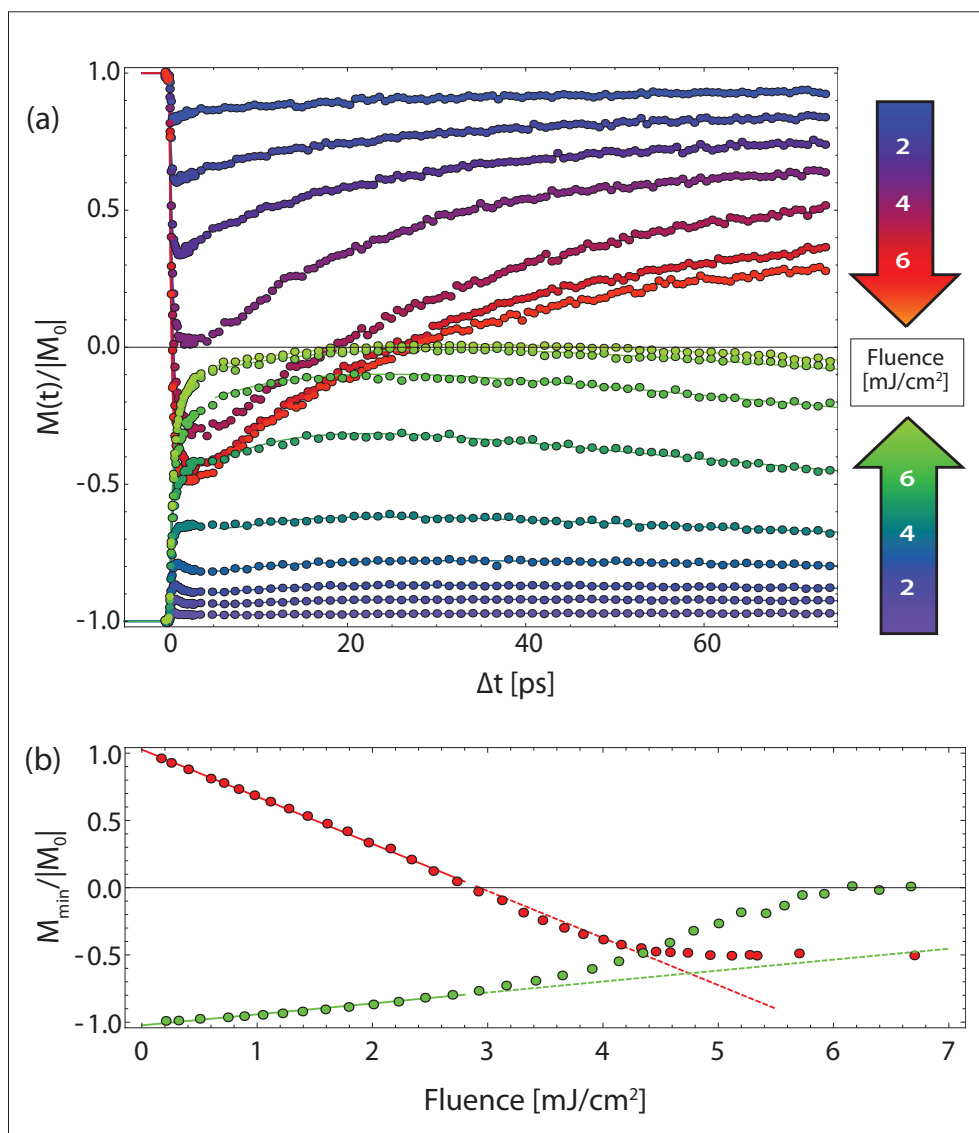


**Figure 5.5:** TR-MOKE measurements at  $\lambda_{\text{Fe}} = 800$  nm and  $\lambda_{\text{Tb}} = 500$  nm. (a) Magnetization dynamics of the Fe (top) and Tb (bottom) sublattice as a function of the fluence. The fluence increases with steps of about  $0.8 \text{ mJ}/\text{cm}^2$ . (b) Minimum magnetization of the Fe (top, red) and Tb (bottom, green) sublattice as a function of the fluence.

### 5.5.1 Demagnetization Timescales

The ultrafast demagnetization times of Fe and Tb are found by a fit of the dynamics at  $t < 3$  ps with an exponential function:

$$dM(t) = g(t, \tau_p)a \left(1 - e^{-t/\tau_1}\right), \quad (5.9)$$

where  $g(t, \tau_p)$  is an errorfunction which takes into account the cross-correlated time width  $\tau_p \approx 90$  fs of the laser pulses, and  $a$  and  $\tau_1$  are fitting parameters which represent the magnitude and the typical time of the ultrafast demagnetization.

The demagnetization time of the Fe sublattice is  $\tau_1^{Fe} = 240 \pm 50$  fs. For comparison, we studied a 20 nm thin Fe film grown under the same conditions as the TbFe alloy, and with the same multilayer structure. We found a demagnetization time of  $300 \pm 40$  fs for pure Fe, being similar to the demagnetization time of Fe in TbFe. These timescales are consistent with other TR-MOKE measurements on thin Fe layers, where demagnetization times in the range of 75 to 400 fs have been reported [22, 23].

The Tb sublattice is characterized by a demagnetization time of  $\tau_1^{Tb} = 300 \pm 60$  fs. The timescale of the second step of the demagnetization of Tb is found from another exponential fit to the measurements at  $t > 5$  ps. This “slow” demagnetization process has a typical time-constant of  $\tau_2^{Tb} = 18 \pm 4$  ps. The magnetization reaches its minimum around  $t = 30$  ps, before it recovers. Comparing these timescales with the reported demagnetization times of pure Tb [17], we notice (i) that the ultrafast demagnetization in pure Tb is roughly two times slower ( $\tau_1^{Tb} = 750 \pm 250$  fs), and (ii) the second step demagnetization in pure Tb is about two times faster ( $\tau_2^{Tb} = 8 \pm 3$  ps).

### 5.5.2 Demagnetization Profiles

The demagnetization of pure RE elements such as Gd and Tb are known for their two-step nature: an ultrafast demagnetization is immediately followed by a slow demagnetization process, succeeded with magnetization recovery. In 3d TM, however, only ultrafast demagnetization occurs. These demagnetization profiles can be modeled well with the microscopic three-temperature model (M3TM), where demagnetization is described as spin-flip events due to spin-lattice relaxation [7, 24, 25]. The ultrafast demagnetization is described resulting from an efficient spin-lattice relaxation due to the enhanced electron temperature. If the magnetic moment of a material is large, such as in Tb and Gd, more spin-flip events are necessary to reach thermal equilibrium between the spin and lattice systems. However, the spin-lattice relaxation becomes inefficient when the electron and lattice are in thermal equilibrium (typically a few ps in metals). As a result, the demagnetization proceeds at a smaller rate after a few ps (typical electron-lattice relaxation time in metals). Basically, this three temperature model can explain the one-step and two-step demagnetization profiles of pure 3d TM

and 4f RE metals by considering angular momentum transfer between only the spin and the lattice systems.

The M3TM model can, however, not explain the demagnetization profile of Tb in the TbFe alloy where a temporary remagnetization occurs. This may be due to the fact that Fe and Tb spins are in a highly excited state and out-of-equilibrium in the first ps after the excitation pulse. Therefore, they cannot be described as a single spin system as in the three temperature model, which is developed for single sublattice systems. Furthermore, in such alloys the demagnetization is not only given by angular momentum transfer from the Fe and Tb spins to the lattice, but there may be also angular momentum transfer between the Fe and Tb spins.

### 5.5.3 Intersublattice Exchange Interaction

Recently, it was observed that also in GdCo and GdFeCo alloys remagnetization occurs before a second demagnetization sets in [26]. It was demonstrated that the inclusion of the intersublattice exchange interaction in the model, which basically takes heat transfer between the two sublattices into account, explains such demagnetization profile. The important role of angular momentum transfer between two magnetic sublattices in alloys was also demonstrated with simulations of ultrafast magnetization dynamics in GdFeCo [18, 19]. It was shown that angular momentum transfer between two sublattices enhances the demagnetization of Gd and Fe in GdFe alloy. Because Fe demagnetizes faster than Gd, the system reaches a transient state in which the magnetization of the Fe sublattice is reversed and has become parallel to the magnetization of the Gd sublattice, i.e., a transient ferromagnetic state [2]. The subsequent relaxation from this meta-stable state is dominated by the intersublattice exchange interaction which forces the magnetization of the Gd sublattice to reverse, restore the antiparallel alignment to Fe, and consequently leads to a switched state.

Next to the demagnetization profile, also the magnitude of the demagnetization of Tb shows an intriguing behavior as a function of the excitation fluence. Although in single sublattice systems the magnitude of the demagnetization increases linearly as a function of the fluence, it can be clearly seen from figure 5.5a that this is not the case for Tb in TbFe: the demagnetization increases at a faster rate above 3-4 mJ/cm<sup>2</sup>.

The maximum change of the demagnetization of the Tb and Fe sublattices is presented in figure 5.5b at a high resolution in the excitation fluence. The demagnetization of both sublattices depends linearly on the excitation fluence up to about 3 mJ/cm<sup>2</sup>. At this fluence the system enters a transient ferromagnetic state due to the reversal of the Fe sublattice. It can be seen that the demagnetization of Tb increases rapidly after this point until full demagnetization is reached. On the other hand, the demagnetization of Fe remains linear as a function of the fluence until it saturates at a value of about  $-0.5M_0$ . As a guide for the eye, the maximum demagnetization in the range 0-3 mJ/cm<sup>2</sup> is extrapolated with a linear fit in figure 5.5b. It



can be seen that even the demagnetization of the Fe sublattices seems to be slightly enhanced after  $3 \text{ mJ/cm}^2$  as well. It should be noted, however, that this small change was not always seen at other positions of the sample where similar fluence dependent TR-MOKE measurements were repeated. The acceleration of the demagnetization of the Tb sublattice, on the other hand, was observed in all experiments.

This remarkable acceleration of the demagnetization of Tb in the transient ferromagnetic state can be understood from the negative intersublattice exchange interaction which tries to pull the system back to an antiferromagnetic alignment. The recovery of the antiferromagnetic alignment from a transient ferromagnetic state can be achieved in two ways: (i) the recovery of the Fe magnetization along its initial direction through remagnetization, or (ii) an enhanced demagnetization of Tb in order to reverse its magnetization. We find that both processes occur simultaneously. The recovery of Fe sets in after a few picoseconds, whereas the demagnetization of Tb enhances. The recovery of the Fe magnetization, however, is the dominating process as the Fe magnetization is recovered to its initial direction before the enhanced demagnetization of Tb leads to the reversal of its magnetization.

It was already mentioned that the strong anisotropy of Tb may play an important role in the relaxation of the Tb and Fe sublattices. It should be noted that also the strong external magnetic field, which ensures stroboscopic measurements, plays an important role in the recovery of the TbFe magnetization. This was found from single shot measurements on TbFeCo under similar excitation conditions as in the TR-MOKE measurements, but without an external magnetic field during the excitation. Initially, the sample was brought in a single domain state in either the “up” or “down” direction with the application of a strong magnetic field. Next, the material was excited with an 100 fs excitation pulse in the intensity range up to  $8 \text{ mJ/cm}^2$  in the absence of an external magnetic field. The final magnetic state of TbFe was probed with SNOM. We found that the magnetization of TbFe fully switches at excitation fluences higher than  $4\text{-}5 \text{ mJ/cm}^2$  (see Section 4.6.2). Switching of the magnetization is not observed when a strong external magnetic field is applied during the excitation with intensities up to  $7 \text{ mJ/cm}^2$ , as presented here. This demonstrates that the external magnetic field in the TR-MOKE measurements presented in figure 5.5 prevents the reversal of the Tb sublattice. However, we found that magnetization reversal in GdFe occurs even for fields up to 2 T. The strong magnetic field pulls the magnetization of GdFe back to the initial direction only at timescales larger than typically 100 ps. This difference between TbFe and GdFe may originate from the strong anisotropy in Tb, which pins the Tb spins along their initial direction as explained in Section 5.4.2.

## 5.6 Summary

The feasibility of element specific probing of ultrafast magnetization dynamics with (near-) visible light was studied in an antiferromagnetically coupled TbFe alloy. We came to the following findings:

- One can selectively study the magnetization of Tb and Fe with a probe wavelength of 500 and 800 nm, respectively.
- The magnetic moments of Tb and Fe evolve against their exchange interaction when excited with an intense 60 fs laser pulse. Consequently, TbFe enters a transient ferromagnetic state within one picosecond at fluences larger than  $3 \text{ mJ/cm}^2$ .
- The demagnetization of the Tb sublattice becomes more efficient when Fe and Tb are ferromagnetically aligned.
- The remarkable acceleration of the Tb demagnetization can be understood from the negative exchange interaction between the Fe and Tb sublattices. This intersublattice exchange pulls the magnetization of Tb towards an opposite direction in order to recover the antiparallel alignment of the Tb and Fe spins.
- Simultaneous with the continued demagnetization of Tb, the reversed magnetization of Fe relaxes back towards its original direction after a few ps, under the influence of the externally applied magnetic field. This process is faster than the demagnetization of Tb. Therefore, the system relaxes back to its original state and no magnetization reversal occurs.
- Element specific probing in the visible range can be generalized to other two-sublattice magnets with a calibration with x-rays. This approach combines the element specific character of x-rays with the high signal-to-noise and easy-to-use superiority of visible light.

## References

- [1] C. D. Stanciu, F. Hansteen, A. V. Kimel, A. Kirilyuk, A. Tsukamoto, A. Itoh, and T. Rasing, *Physical Review Letters* **99**, 047601 (2007).
- [2] I. Radu, K. Vahaplar, C. Stamm, T. Kachel, N. Pontius, H. A. Durr, T. A. Ostler, J. Barker, R. F. L. Evans, R. W. Chantrell, et al., *Nature* **472**, 205 (2011).
- [3] C. Stamm, T. Kachel, N. Pontius, R. Mitzner, T. Quast, K. Holldack, S. Khan, C. Lupulescu, E. F. Aziz, M. Wietstruk, et al., *Nature Materials* **6**, 740 (2007).
- [4] C. La-O-Vorakiat, M. Siemens, M. M. Murnane, H. C. Kapteyn, S. Mathias, M. Aeschlimann, P. Grychtol, R. Adam, C. M. Schneider, J. M. Shaw, et al., *Physical Review Letters* **103**, 257402 (2009).
- [5] E. Beaurepaire, J. C. Merle, A. Daunois, and J. Y. Bigot, *Physical Review Letters* **76**, 4250 (1996).
- [6] B. Koopmans, M. van Kampen, J. T. Kohlhepp, and W. J. M. de Jonge, *Physical Review Letters* **85**, 844 (2000).
- [7] B. Koopmans, G. Malinowski, F. D. Longa, D. Steiauf, M. Faehnle, T. Roth, M. Cinchetti, and M. Aeschlimann, *Nature Materials* **9**, 259 (2010).
- [8] L. Guidoni, E. Beaurepaire, and J. Y. Bigot, *Physical Review Letters* **89**, 017401 (2002).
- [9] M. Sultan, U. Atxitia, A. Melnikov, O. Chubykalo-Fesenko, and U. Bovensiepen, *Physical Review B* **85**, 184407 (2012).
- [10] E. Arenholz, E. Navas, K. Starke, L. Baumgarten, and G. Kaindl, *Physical Review B* **51**, 8211 (1995).
- [11] P. Hansen, *Handbook of Magnetic Materials*, vol. 6 (Elsevier, 1991).
- [12] P. Hansen, C. Clausen, G. Much, M. Rosenkranz, and K. Witter, *Journal of Applied Physics* **66**, 756 (1989).
- [13] A. Delin, O. Eriksson, B. Johansson, S. Auluck, and J. M. Wills, *Physical Review B* **60**, 14105 (1999).
- [14] S. Hufner, F. Schumann, E. Rotenberg, J. Tobin, S. H. Yang, B. S. Mun, S. Morton, J. Schafer, and D. Ehm, *Physical Review B* **63**, 085106 (2001).
- [15] J. K. Lang, Y. Baer, and P. A. Cox, *Journal of Physics F-Metal Physics* **11**, 121 (1981).

- 
- [16] K. M. Dobrich, G. Bihlmayer, K. Starke, J. E. Prieto, K. Rossnagel, H. Koh, E. Rotenberg, S. Bluegel, and G. Kaindl, *Physical Review B* **76**, 035123 (2007).
- [17] M. Wietstruk, A. Melnikov, C. Stamm, T. Kachel, N. Pontius, M. Sultan, C. Gahl, M. Weinelt, H. A. Durr, and U. Bovensiepen, *Physical Review Letters* **106**, 127401 (2011).
- [18] J. H. Mentink, J. Hellsvik, D. V. Afanasiev, B. A. Ivanov, A. Kirilyuk, A. V. Kimel, O. Eriksson, M. I. Katsnelson, and T. Rasing, *Physical Review Letters* **108**, 057202 (2012).
- [19] T. A. Ostler, J. Barker, R. F. L. Evans, R. W. Chantrell, U. Atxitia, O. Chubykalo-Fesenko, S. El Moussaoui, L. Le Guyader, E. Mengotti, L. J. Heyderman, et al., *Nature Communications* **3**, 666 (2012).
- [20] A. R. Khorsand, M. Savoini, A. Kirilyuk, A. V. Kimel, A. Tsukamoto, A. Itoh, and T. Rasing, *Physical Review Letters* **108**, 127205 (2012).
- [21] B. T. Thole, P. Carra, F. Sette, and G. van der Laan, *Physical Review Letters* **68**, 1943 (1992).
- [22] E. Carpene, E. Mancini, C. Dallera, M. Brenna, E. Puppini, and S. De Silvestri, *Physical Review B* **78**, 174422 (2008).
- [23] A. Weber, F. Pressacco, S. Gunther, E. Mancini, P. M. Oppeneer, and C. H. Back, *Physical Review B* **84**, 132412 (2011).
- [24] B. Koopmans, J. J. M. Ruigrok, F. D. Longa, and W. J. M. de Jonge, *Physical Review Letters* **95**, 267207 (2005).
- [25] T. Roth, A. J. Schellekens, S. Alebrand, O. Schmitt, D. Steil, B. Koopmans, M. Cinchetti, and M. Aeschlimann, *Physical Review X* **2**, 021006 (2012).
- [26] A. Mekonnen, A. R. Khorsand, M. Cormier, A. V. Kimel, A. Kirilyuk, A. Hrabec, L. Ranno, A. Tsukamoto, A. Itoh, and T. Rasing, submitted (2012).

## CHAPTER 6

---

### Valorisation: Data Storage with the Speed of Light

---

*“Why sir, there is every possibility that you will soon be able to tax it.”*

MICHAEL FARADAY, c. 1860

To the Chancellor,  
when questioning the usefulness of electricity.

## Introduction

The results presented in this thesis may provide new opportunities for industry. The potential impact of our findings for the information technology is discussed in this chapter. In particular, a comparison is drawn between the state-of-the-art hard disk drive (HDD) technology where magnetic field pulses are used in order to write information, and our novel approach to use light in a new generation of HDD's, illustrated in figure 6.1a. Currently, a prototype device for all-optical magnetic recording is being developed in our group.

## State of the Art

Hard disk drives have been the dominant devices for storage of data since the early 1960's. Nowadays, they are imbedded in many digital devices such as PC's, laptops, notebooks, multiple-user computers (servers), digital video recorders and automotive vehicles. Today an average household in Europe has more than two hard disks. The amount of information generation worldwide has increased from an estimated one exabyte (one billion GB) in 2000 to more than 1000 exabytes in 2011 [1]. The explosive demand for information storage has put unprecedented demands on HDD's in terms of speed, areal density, energy consumption, and reliability.

Although HDD's have experienced an impressive improvement of their performance over the last five decades, the basic concepts of HDD's are maintained since the first hard drive storage unit of IBM in 1956 (see left side of 6.1b). A logical bit is represented by a magnetic domain pointing either "up" or "down", corresponding to a "1" or "0". The speed of information transfer is limited by the time which is necessary to reverse the magnetization of a domain. Magnetization reversal is achieved by the application of a magnetic field pulse opposite to the magnetization by a current loop in the writing head, which induces a precessional motion of the magnetization and leads eventually to full reversal. This process takes typically a few hundreds of picoseconds up to one nanosecond for the achievable magnetic field strengths in commercial devices, and marks a technological limit for the read/write rate of current HDD's of roughly 1 GHz.

Due to the steady improvements of HDD's over the past 50 years, the current devices have almost reached this technological limit for read/write rates. Furthermore, it is expected that the current HDD technology will also hit a technological limit for the areal density at one Tb/in<sup>2</sup> [1–3]. At this point, the small magnetic bits become superparamagnetic: the magnetization of the bits flip randomly under the influence of temperature. To overcome this problem magnetic materials with high magnetic anisotropy are necessary. Even though such materials are available to provide stability of written information against thermal fluctuations, their application is impossible in the usual magnetic-field-writing scheme as the required switching field

greatly surpasses the practical limit of about 1 T available from today's (inductive) write technology.

To solve this dilemma, a new technique called heat-(or temperature-)assisted mag-

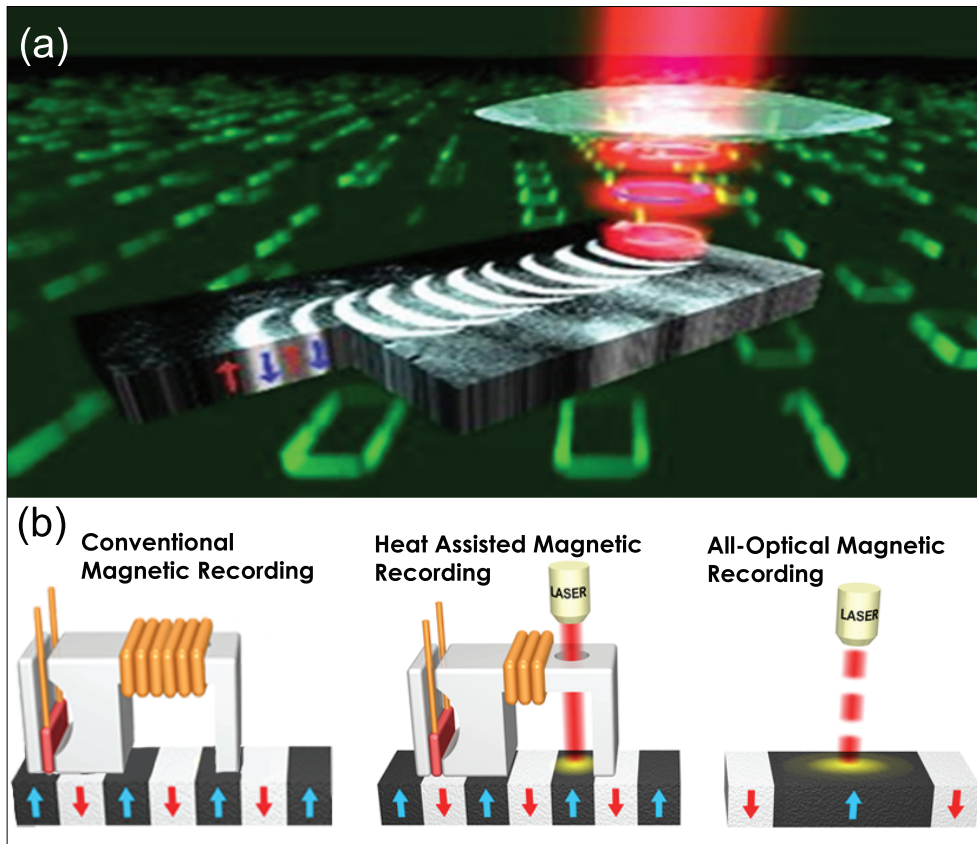


**Figure 6.1:** (a) Artistic illustration of all-optical magnetic recording (note: the written data in this picture are real, adapted from ref. [4]). (b) Three different methods for magnetic data storage. (left) Conventional magnetic recording in hard disk drives. The bits are reversed with a magnetic field pulse generated in a coil. (middle) Heat assisted magnetic recording. With this technique smaller bit sizes should be achieved, but two stimuli are required: magnetic field and laser pulse. (right) All-optical magnetic recording. In our approach a bit is reversed with a laser pulse. Magnetic fields are no longer required with this technique. All-optical magnetic recording is superior in terms of speed and could potentially push the write/read rate of the information technology from 1 GHz to the THz regime.

netic recording is being developed [5, 6]. Heat-assisted magnetic recording (HAMR) is a technology that magnetically records data on high-stability media using laser assistance to first heat the material (see middle of figure 6.1). HAMR takes advantage of the fact that the coercive field reduces with increasing temperature. However, this approach does not simplify the magnetic recording process but instead involves more elements (a magnet and a laser) leading to higher manufacturing cost as well as higher power consumption. Another limitation of the HAMR technology is that it is designed only to increase the areal bit density and not to enhance the switching time of the bits. HAMR is expected to enter the market within a few years.

## All-Optical Magnetic Recording

The control of magnetism by light is one of the most promising approaches to this problem, since a laser pulse is one of the shortest ever man-made events and can be used to manipulate magnetization. We propose a novel approach called *all-optical magnetic recording* [4, 7, 8]: only a laser pulse is used to write a magnetic bit (see right side of 6.1). Therefore, there is no need for a magnetic field, which enormously simplifies head design and manufactory compared to HAMR. In terms of speed, all-optical magnetic recording is superior compared to other information storage technologies, as the switching time of bits is at least 100 times faster. Our novel technique may push rates to an unprecedented regime of 1 THz. In addition, the writing energy per bit may be several orders of magnitude lower than current technology.

## Challenges and Achievements

However, there are several challenges to overcome in order to make all-optical magnetic recording a competitive alternative to the current technology for information storage. The results presented in this thesis contribute to three major challenges: making all-optical switching controllable and highly reproducible, decreasing the bit size to achieve higher areal bit densities, and decreasing the energy consumption for each write-event to have an economical alternative to conventional devices.

In the original discovery of all-optical magnetic recording by circularly polarized light [4], the effect was interpreted in terms of the (non-thermal) inverse Faraday effect [7]. We have demonstrated, however, that the only role of light in all-optical magnetic switching is to deposit enough energy in the magnetic system [8]. Although this is a heat-induced effect, the final state of the magnetization can be fully controlled by the amount of energy which is deposited in the magnetic system. The deposited energy in the magnetic system should overcome a threshold value in order to achieve switching, otherwise the system will relax back to its initial state. Left and right circularly polarized light switch the material at different light intensities because they are absorbed with different efficiencies in the magnetic system, due to “magnetic



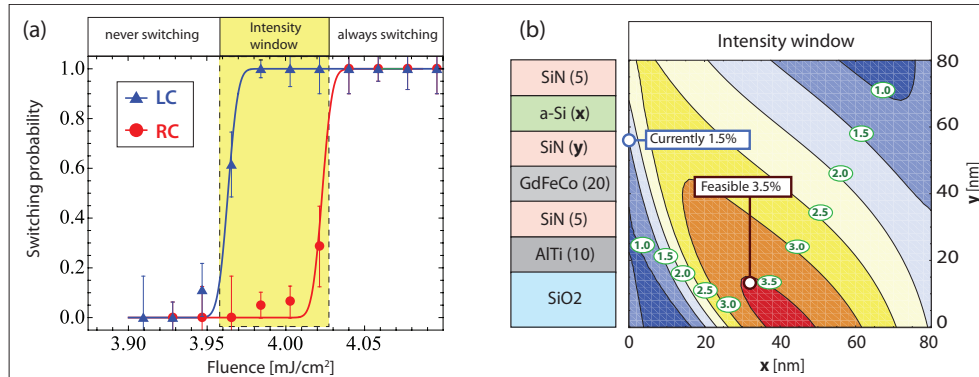


**Figure 6.2:** (a) Switching probability of the magnetization of GdFeCo as a function of the intensity for left (LC) and right (RC) circularly polarized. The excitation wavelength is 700 nm and the temporal width of the laser pulse is 55 fs. The intensity regime in which all-optical switching is helicity dependent is called the *intensity window* (yellow area). (b) The intensity window as a function of the layer thickness of a-Si ( $x$ ) and SiN ( $y$ ). At the left is shown the structure of the magnetic material.

circular dichroism”. The intensity regime in which the efficiently absorbed helicity of the light results in switching and the less efficiently absorbed helicity leads only to recovery is called the *intensity window* (see figure 6.2a). It can be seen that only for light intensities within this window switching is helicity dependent: below the intensity window there is no switching, whereas above this window there is always switching, independent of the helicity of the light.

The helicity dependence of switching in the intensity window gives the unique opportunity to fully control the final state of the magnetization after excitation with a single circularly polarized laser pulse, independent of the initial state. This can be understood as follows: Let’s assume that right circularly polarized light is absorbed more efficiently by magnetization “up” than “down”. Then, magnetization “up” will switch to “down” if it is excited with right circularly polarized light of which its intensity is tuned to the intensity window. On the other hand, magnetization “down” will not switch under the exact same conditions because of a less efficient absorption of the light pulse. This means that, independent of the initial state, the final state is always magnetization “down” if a right circularly polarized light pulse is used within the intensity window. Similarly, an exposure to a left circularly polarized light pulse will always result in magnetization “up”. Thus, helicity dependent switching gives full control over the final state of the magnetization.

This new understanding of the role of light in all-optical switching allows one to

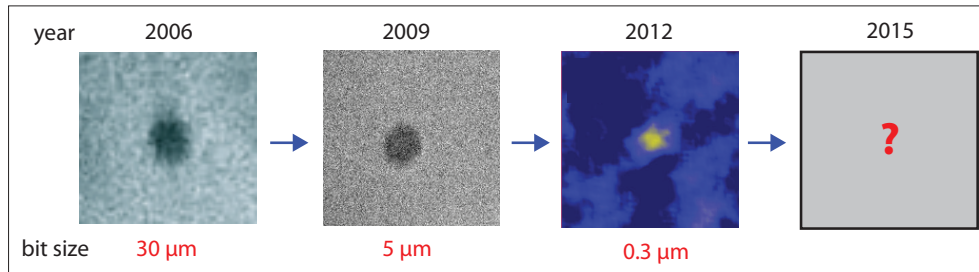


**Figure 6.3:** The progress in the achieved bit size with all-optical magnetic recording since 2006. The sizes correspond to the diameter of the switched domain. We expect that a further decrease of the bit size will continue to at least tens of nanometers, with the integration of plasmonic antennas in devices for magnetic recording.

tailor the properties of the magnetic material in order to achieve a higher degree of reproducibility. A larger intensity window is crucial for this purpose: this window must be larger than the typical pulse-to-pulse noise of a pulsed laser in order to have full control of the final magnetic state with circularly polarized light. In the current samples the intensity window is around 1%, at a similar level as the noise of the laser. However, by a proper choice of thickness and index of refraction of the cover layers, the energy transfer from the light pulse to the magnetic medium can be further optimized. We have calculated that the intensity window can be easily enhanced by more than 150% simply by changing the thickness of non-magnetic layers. This is shown in figure 6.2b. Tuning the thickness and other properties of these and the magnetic layer could enhance this window even further.

Another major limitation of all-optical switching had been the size of a switched domain, which defines the bit size and areal bit density. Until recently, this phenomenon was demonstrated only for domain sizes of at least a few microns (see figure 6.3a,b) [4, 7]. This is much larger than the achievable sizes of  $20 \times 100 \text{ nm}^2$  in the current state-of-the-art technology. In this work, we have demonstrated the feasibility of reducing the switched bit size from a few microns to at least 250 nm using a confocal microscope in combination with the use of a magnet with high magnetic anisotropy, as shown in figure 6.3c. The progress in decreasing the bit sizes with all-optical magnetic recording since 2006, is shown in figure 6.3. It can be seen that during the last 6 years, the size has been decreased by 2 orders of magnitude. We believe that the bit size could be reduced even further to potentially tens of nanometers. A fundamental issue in further decreasing the bit size is the diffraction limit of light, which is typically a few hundreds of nanometers in the visible range. Confining the energy of a light pulse to smaller dimensions than the diffraction limit is impossible with conventional optical tools such as objectives or mirrors, which limits

a further reduction of a bit size. A solution to this problem is the use of plasmonic antennas [5, 6, 9]. It has been demonstrated that light can be confined to 41 nm in GdFeCo with the use of such antennas [10]. Therefore, an integration of plasmonic antennas with all-optical magnetic recording could significantly reduce the bit sizes, making the areal density of this novel approach competitive with the current state-of-the-art HDD technology. Plasmonic antennas are already being developed and used in HAMR in order to heat nanoscale spots with a laser. Therefore, the technology for the integration of plasmonic antennas with magnetic recording has already been developed, and could be used with minimum adjustments in a future device based on all-optical magnetic recording.

The immense amount of information which needs to be stored and processed requires an increasing amount of power. The world wide power consumption of data centers (of Google, Yahoo, Microsoft, Apple, Amazon, etc.) was estimated to be 31 GW (equivalent to 30 million households) in 2012, whereas the predicted world wide energy consumption of data centers for 2050 is approaching the current electric energy generated in the 27 member states of the European Union! Therefore, a small decrease of the energy consumption for writing one bit results in a significant environmental and economical gain. In the present technologies, the energy which is required to reverse a 50x50 nm bit is on the order of typically 100 pJ (1 pJ=  $10^{-12}$  J). With all-optical switching, this is only a few pJ for a 250x250 nm<sup>2</sup> domain: a gain of almost 2 order of magnitude per bit! This gain will be even larger if the switched domain is reduced by a further confinement of the light.

Similar observations can be made for the manipulation of data in processors. Though, following Moore's law, the miniaturization of components has resulted in more energy efficient ways of generating and storing digital information, this is more than offset by the much faster growth in the use of these modern digital tools, leading to an overall growth in energy consumption and increasing demands on materials. For example, the impressive developments of Si-based electronics has allowed the developments of fast and powerful processors that are used for large scale computations of material properties as well as an enormously expanding industry of digital games and the collecting and sharing of digital information worldwide. However, though industry is already entering the next level of miniaturization (22 nm node), the clockspeed of modern processors is lagging behind because of the generation of too much heat. Spin based logic (spintronics) could provide a possible more energy efficient solution, but is lacking the necessary materials and speed. All-optical generation and manipulation of magnetic bits could provide a solution, if the proper materials and technology can be developed.

A few key characteristics of all-optical magnetic recording and conventional HDD technology are summarized in Table 6.1.

Currently, one of the challenges is to make all-optical magnetic recording feasible for other magnetic materials. Until now, all-optical switching has been observed only

**Table 6.1:** The hard disk drive technology compared to all-optical magnetic recording. The energy to write a bit with all-optical magnetic recording is 3 pJ for a  $250 \times 250$  nm<sup>2</sup> domain, whereas the expected energy for a bit of a similar size as in HDD's is 0.1 pJ.

	Hard disk drive	All-optical magnetic recording
stimulus	magnetic field	laser pulse
bit size [nm × nm]	<b>20×100</b>	250×250
reversal-time [ns]	0.3-1	<b>&lt;0.01</b>
energy per bit [pJ]	100-200	<b>0.1-3</b>

in rare-earth containing alloys. Although these elements are abundant on earth, rare-earth mining is involved and it is almost nonexistent outside China, which controls more than 95 percent of the supply. Until there are more players on the market, the HDD industry wants alternatives for rare-earth elements. With our improved understanding of all-optical switching we know that in these multi-sublattice magnetic materials the magnetization can be deterministically switched using un-polarized fs laser pulses [8, 11]. This fast switching appears to be both driven by the (hot) electron temperature and the exchange interaction between the sublattices [11, 12]. This phenomenon of heat-driven magnetic reversal, harnesses the extremely large exchange field, either by optical pulses or by electric pulses. This is a promising prospect to essentially remove the rare earth elements by designing synthetic ferrimagnetic materials consisting of antiferromagnetically coupled multilayers that can be manipulated by short laser pulses.

## Summary and Outlook

All-optical magnetic recording has significant advantages compared to the current state-of-the-art technology for data storage in terms of both speed and energy consumption. It could potentially push the write/read rate of the information technology from one GHz to the THz regime, provided the proper materials can be developed and incorporated. The areal density has already improved significantly during the last 6 years, but it is not yet at the same level as the current technology. With the use of plasmonic antennas we expect that the bit size can reach the sub-100 nm regime, becoming competitive with the current technology. With an enhancement of the areal density, together with the potentially high rates which can be achieved, all-

optical magnetic recording could also serve an alternative technology for non-volatile logic, leading to a universal memory approach and allowing instant on/off capability of computer devices.

## References

- [1] R. Wood, *Journal of Magnetism and Magnetic Materials* **321**, 555 (2009).
- [2] M. Mallery, A. Torabi, and M. Benakli, *IEEE Trans. Magn.* **38**, 1719 (2002).
- [3] R. Wood, *IEEE Trans. Magn.* **36**, 36 (2000).
- [4] C. D. Stanciu, F. Hansteen, A. V. Kimel, A. Kirilyuk, A. Tsukamoto, A. Itoh, and T. Rasing, *Physical Review Letters* **99**, 047601 (2007).
- [5] W. A. Challener, C. B. Peng, A. V. Itagi, D. Karns, W. Peng, Y. Y. Peng, X. M. Yang, X. B. Zhu, N. J. Gokemeijer, Y. T. Hsia, et al., *Nature Photonics* **3**, 220 (2009).
- [6] B. C. Stipe, T. C. Strand, C. C. Poon, H. Balamane, T. D. Boone, J. A. Katine, J. L. Li, V. Rawat, H. Nemoto, A. Hirotsune, et al., *Nature Photonics* **4**, 484 (2010).
- [7] K. Vahaplar, A. M. Kalashnikova, A. V. Kimel, D. Hinzke, U. Nowak, R. Chantrell, A. Tsukamoto, A. Itoh, A. Kirilyuk, and T. Rasing, *Physical Review Letters* **103**, 117201 (2009).
- [8] A. R. Khorsand, M. Savoini, A. Kirilyuk, A. V. Kimel, A. Tsukamoto, A. Itoh, and T. Rasing, *Physical Review Letters* **108**, 127205 (2012).
- [9] P. Biagioni, J. S. Huang, L. Duo, M. Finazzi, and B. Hecht, *Physical Review Letters* **102**, 256801 (2009).
- [10] B. Koene, M. Savoini, A. V. Kimel, A. Kirilyuk, and T. Rasing, *Applied Physics Letters* **101**, 013115 (2012).
- [11] T. A. Ostler, J. Barker, R. F. L. Evans, R. W. Chantrell, U. Atxitia, O. Chubykalo-Fesenko, S. El Moussaoui, L. Le Guyader, E. Mengotti, L. J. Heyderman, et al., *Nature Communications* **3**, 666 (2012).
- [12] J. H. Mentink, J. Hellsvik, D. V. Afanasiev, B. A. Ivanov, A. Kirilyuk, A. V. Kimel, O. Eriksson, M. I. Katsnelson, and T. Rasing, *Physical Review Letters* **108**, 057202 (2012).



## CHAPTER 7

---

### Summary

---

*“I was born not knowing and have had only a little time to change that here and there.”*

RICHARD FEYNMAN, 1985

Magnetism has a long and rich history, and has found many applications since the introduction of the compass more than thousand years ago. The magnetization of ferromagnets can point either “up” or “down”, which is defined by the history of magnetic fields in the vicinity of the magnet. In a sense, this means that a magnet has a memory: its state gives information about its past. It is this fundamental property of magnets which has served as one of the cornerstones of magnetic data storage in current hard disk drive technology. Due to the demand for “faster” and “smaller” magnetic bits, the field of (nano-)magnetism is still one of the hottest areas in the field of condensed matter physics. In order to achieve faster switching times, one needs shorter stimuli. Femtosecond lasers are of particular interest, as they are one of the shortest stimuli available. The introduction of these lasers in the nineties have allowed the study of ultrafast phenomena in magnets, a regime which is relatively unexplored and poorly understood because the traditional laws of magnetism do not longer hold in this regime, where the magnet is in a highly excited state.

Ultrafast magnetization dynamics has been explored in the past 15 years, starting with the pioneering work of Beaurepaire *et al.* in 1996. This has led to the discovery of a wide variety of novel and ultrafast phenomena. In view of this, a general overview of ultrafast spin dynamics is given in the first chapter. In particular, the recent progress in ultrafast all-optical magnetic switching is discussed. All-optical switching was discovered in 2007, revealing the feasibility to reverse the magnetization of GdFeCo with a single ultrashort circularly polarized laser pulse in the absence of an external magnetic field. This makes this discovery of potential interest for the hard disk drive industry. The origin of the light-matter interaction responsible for this novel phenomenon was poorly understand. All-optical switching serves as the main topic of this thesis. Amongst the goals of this thesis are to gain a better understanding of the role of light in this phenomenon, gain more insight in the individual behavior of each of the magnetic species at these ultrashort timescales, and to find the requirements and to show the feasibility to downsize the area of a switched domain.

Our approach is explained in Chapters 2 and 3. In Chapter 2, the magnetic and magneto-optical properties of rare earth-transition metal alloys are given, and we motivate our choice for the materials GdFeCo and TbFeCo in this study. The experimental techniques which are employed in this work are explained in Chapter 3. Amongst these techniques is ultrafast “time-resolved ultrafast magneto-optical Kerr effect” (TR-MOKE), a technique which allows to track the dynamics of the magnetization with a temporal accuracy of less than 1 fs. Furthermore, spectroscopy is extensively used in order to deduce the origin of the light-matter interaction involved in the studied phenomena.

The role of light in all-optical switching is deduced in Chapter 4. First of all, it is demonstrated that all-optical switching occurs at any optical wavelength and for any light polarization in GdFeCo. The light-intensity at which this phenomenon occurs, however, is dependent on the light helicity. The measurements reveal that the



role of light in all-optical switching is (ultrafast) heating of the magnetic medium, in striking contrast to former models which assumed that light acts as an effective magnetic field. The dependence of this phenomenon on the helicity of the light can be accurately explained by taking into account that the light absorption is dependent on the polarization through the so-called “magnetic circular dichroism”. We find that the difference in switching threshold for left and right circularly polarized light matches exactly the difference in absorption of left and right circularly polarized light in the magnetic medium. This new understanding enables the possibility to design multilayer structures with tailored properties for the application of all-optical magnetic recording. Furthermore, we demonstrated the feasibility to decrease the switched domain size from a few microns to less than 250 nm, with the prospect of achieving sub-100 nm domains. This was done by replacing GdFeCo by TbFeCo, a material which has very small domain walls, and confining the excitation pulse with a confocal microscope.

In the first hundreds of femtosecond after the excitation of a magnetic alloy, the material is in a highly excited state and each one of the magnetic species behaves differently. In order to get a better understanding of magnetic interactions on these ultrashort timescales, one needs to track the magnetization dynamics of these species individually, whereas conventional optical methods give access to the collective response of all species. Therefore, femtosecond time-resolved and element specific studies of magnetization dynamics in multi-sublattice systems (magnets consisting of multiple and distinct magnetic species which are coupled) are required to further explore and exploit the intriguing possibilities of ultrafast magnetization dynamics. Until now, element specificity was achieved through the use of soft x-rays or EUV. Techniques utilizing high energy photons have, however, considerable limitations, in particular in combination with sub-picosecond time resolution. In Chapter 5, we demonstrate the feasibility of using visible light for element specific studies, and discuss the requirements for this novel approach. We study ultrafast laser-induced magnetization dynamics of a TbFe alloy, and demonstrate that one can selectively study the dynamics of Tb- and Fe-spins choosing the wavelength of light below and above 610 nm, respectively. Furthermore, we find that at high excitation intensities the antiferromagnetically coupled spins temporarily align ferromagnetically. The magnetization of the Tb sublattice demagnetizes at an accelerated rate in this meta-stable state, and becomes almost fully quenched. The remarkable acceleration of the Tb demagnetization can be understood from the negative exchange interaction between the Fe and Tb sublattices, through which the system prefers to be antiferromagnetically aligned. Finally, we propose a procedure to generalize element specific probing in the visible range to other two-sublattice magnets, using a calibration with x-rays. This approach combines the element specific character of x-rays with the high signal-to-noise and easy-to-use superiority of visible light, and serves as a simple alternative method for performing ultrafast element specific measurements.

The research and new findings described in this thesis may result in new opportunities for the computer industry. All-optical magnetic recording has the potential to serve as an alternative technique for the storage of information. It has significant advantages compared to the current state-of-the-art technology for data storage in terms of both speed and energy consumption. The areal information density has improved significantly with the use of confocal microscopy in this work. It is expected that it will become competitive to the current technology by integration plasmonic antennas in devices for all-optical magnetic recording. Currently, one of the challenges for a large-scale application of magnetic recording is engineering magnetic systems which allow all-optical switching but do not consist of rare-earth materials. Another possible application of this work is a relatively cheap and easy alternative method to measure ultrafast magnetization dynamics with element specificity for fundamental research. This novel approach may, therefore, contribute to a better understanding of ultrafast processes and interactions in magnets.

## CHAPTER 8

---

### Samenvatting

---

*“Welnu meneer, naar alle waarschijnlijkheid kunt u er binnenkort belasting op heffen.”*

MICHAEL FARADAY, CA. 1860

tegen de minister van Financiën,  
toen hij het nut van elektriciteit ter discussie stelde.

Magnetisme kent een lange en rijke geschiedenis en heeft veel toepassingen gevonden sinds de introductie van het kompas meer dan duizend jaar geleden. De magnetisatie van een ferromagneet kan in twee tegengestelde richtingen wijzen, bijvoorbeeld naar “boven” en “beneden”, richting de noordpool van de magneet. Deze wordt bepaald door de geschiedenis van de magneetvelden in de buurt van de magneet. In zekere zin betekent dit dat een magneet een geheugen heeft: zijn huidige toestand geeft informatie over zijn verleden. Deze fundamentele eigenschap van magneten is één van de hoekstenen van de harde schijf-technologie waarmee gegevens kunnen worden opgeslagen in computers. Magnetisme mag dan wel heel oud zijn, maar de fysica achter verschillende magnetische fenomenen (en met name snelle magnetische fenomenen) zijn soms nog steeds niet doorgrond. Dit onderzoeksgebied wordt deels gedreven door de voortdurende vraag naar steeds snellere en kleinere magnetische bits en maakt magnetisme tot één van de speerpunten in het hedendaagse onderzoek van de vastestoffysica. Om snellere schakelsnelheden te behalen heeft men korte stimulatiemechanismen nodig. Femtoseconde lasers zijn bij uitstek geschikt voor dit doel, aangezien ze enorm korte pulsen kunnen leveren die veel energie bevatten. Met behulp van korte laserpulsen kunnen ultrasnelle fenomenen in magneten onderzocht worden. Dit is een relatief nieuw onderzoeksgebied waarin de conventionele modellen voor magnetisme niet meer gelden, omdat de magneet in een hoog aangeslagen toestand terecht komt.

Onderzoek naar ultrasnelle magnetisatiedynamica begon in 1996 met het pionierswerk van onder andere Beaurepaire. Dit heeft geleid tot de ontdekking van een groot scala aan ultrasnelle fenomenen in magneten. In het eerste hoofdstuk is een beknopte inleiding in de theorie van magnetisatiedynamica gegeven en een overzicht van de ontwikkelingen in het onderzoek naar ultrasnelle magnetische verschijnselen. In het bijzonder wordt de ontdekking van het geheel-optisch schakelen van magnetisatie toegelicht. Hiermee wordt bedoeld dat een enkele ultrakorte laserpuls de magnetisatie van een magneet (GdFeCo) kan schakelen zonder de hulp van een extern magnetisch veld. De onderliggende fysica van dit fenomeen, dat grote potentie heeft voor de technologie voor harde schijven, is slechts gedeeltelijk begrepen. Het hoofddoel van dit proefschrift is het ontwikkelen van een beter begrip van dit fenomeen door een combinatie van experimenten en berekeningen. We onderzoeken onder andere de rol van het licht in het geheel-optisch schakelen van magneten, de onderlinge interactie van de verschillende magnetische elementen en de mogelijkheid om de grootte van het geschakelde domein te verkleinen.

We gebruiken voor dit onderzoek magneten die een legering van zeldzame aarden en overgangsmetalen zijn. In hoofdstuk 2 worden de eigenschappen van deze materialen besproken, waarmee we onze keuze voor GdFeCo en TbFeCo toelichten. De experimentele technieken die zijn gebruikt voor dit onderzoek zijn uitgelegd in hoofdstuk 3. Eén van de technieken die we hebben gebruikt is ultrasnelle tijdsopgeloste magneto-optische Kerr effect (TR-MOKE), een techniek waarmee de magnetisatiedy-

namica kan worden bestudeerd met een temporele nauwkeurigheid van minder dan één femtoseconde. De aard van de licht-materie interactie wordt onder andere bestudeerd met spectroscopische metingen, waarbij alleen de golflengte van het licht gevarieerd wordt en andere grootheden onveranderd blijven.

De rol van het licht in het geheel-optisch schakelen is beschreven in hoofdstuk 4. Ten eerste is aangetoond dat het geheel-optisch schakelen van de magnetisatie van GdFeCo mogelijk is voor elke optische golflengte en polarisatie van het licht. De metingen tonen ondubbelzinnig aan dat de rol van het licht in het geheel-optisch schakelen ultrasnelle verhitting van de magneet is, in schril contrast met eerdere modellen waarbij werd aangenomen dat het schakelen plaatsvindt doordat het licht een effectief magneetveld creëert in de magneet. De lichtintensiteit waarbij dit fenomeen plaatsvindt is echter wel afhankelijk van de polarisatie. De afhankelijkheid van de polarisatie van het licht in dit fenomeen kan nauwkeurig worden verklaard door in acht te nemen dat de absorptie van het licht in het magnetische materiaal polarisatie-afhankelijk is door het zogeheten “magnetisch circulair dichroïsme”. Het verschil tussen de lichtintensiteit van links en rechts gepolariseerd licht waarbij het schakelen plaatsvindt is exact gelijk aan het verschil in absorptie van deze twee polarisatie-richtingen in het magnetische materiaal. Dit nieuwe inzicht maakt het mogelijk om magnetische materialen met op maat vervaardigde eigenschappen voor de toepassing van het geheel-optisch schakelen te groeien door simpelweg alleen de dikte van de verschillende materiaallagen aan te passen. Verder is in hoofdstuk 4 aangetoond dat de geschakelde domeinen met een factor 10 verkleind kunnen worden tot in ieder geval 250 nm en potentieel zelfs tot minder dan 100 nm. Dit is gerealiseerd door GdFeCo te vervangen met TbFeCo, een magneet die bekend staat om haar kleine domeinwanden, in combinatie met confocale microscopie.

Voor het verder verkennen en gebruikmaken van de intrigerende mogelijkheden van ultrasnelle magnetisatiedynamica zijn femtoseconde tijdsopgeloste technieken met elementgevoeligheid vereist. Dit is in het bijzonder belangrijk voor magnetische materialen die bestaan uit verschillende elementen die sterk met elkaar gekoppeld zijn, zoals GdFeCo en TbFeCo. In een sterk aangeslagen toestand bewegen de magnetische elementen los van elkaar. Hun individuele dynamica geeft inzicht over magnetische interacties op de ultrakorte tijdschaal. Echter, metingen met zichtbaar licht geven normaal gesproken de gezamenlijke respons van alle magnetische elementen en daarom is er geen gevoeligheid voor de afzonderlijke elementen. Tot dusver waren elementgevoelige metingen alleen aangetoond met röntgenstraling of extreem ultraviolet licht. Helaas hebben technieken die gebruikmaken van hoog-energetische fotonen aanzienlijke nadelen, met name in combinatie met subpicoseconde tijdsresolutie. In hoofdstuk 5 wordt aangetoond dat elementgevoelige metingen ook mogelijk zijn met zichtbaar licht, wat veel gemakkelijker en veiliger te gebruiken is dan hoog-energetische fotonen. We leggen deze nieuwe benadering uit en geven de eisen waaraan de experimenten en materialen moeten voldoen. We bestuderen de ultrasnelle dynamica van een TbFe

legering en tonen aan dat de respons van Fe dan wel Tb gemeten wordt met licht van een golflengte van respectievelijk boven en onder 610 nm. Verder is ontdekt dat in een sterk aangeslagen toestand de magnetisatie van Fe en Tb tegen hun natuurlijke toestand in tijdelijk parallel zijn. Deze instabiele toestand is essentieel in het geheel-optisch schakelen van GdFeCo. In TbFeCo zien we dat de demagnetisatie van Tb versnelt in deze toestand. Deze opmerkelijke versnelling van de demagnetisatie wordt uitgelegd aan de hand van de negatieve exchange-interactie tussen Fe en Tb, wat het materiaal een sterke voorkeur geeft voor een parallelle ordening. Tot slot stellen wij een generalisatie van deze elementgevoelige techniek voor andere multisubrooster magneten voor met behulp van een kalibratiemeting met röntgenstraling. Deze nieuwe benadering combineert de elementgevoelige aard van röntgenstraling met de superieure signaal-ruis verhouding en fungeert als een relatief eenvoudig alternatief voor ultrasnelle en elementgevoelige metingen.

De resultaten en nieuwe bevindingen die zijn bescheven in dit proefschrift zouden een bijdrage kunnen leveren aan nieuwe toepassingen in de computerindustrie. Het geheel-optisch schakelen van magneten zou in de toekomst als een alternatieve technologie kunnen dienen voor het opslaan van informatie. De snelheid en energieverbruik van deze nieuwe techniek is significant beter dan die van de huidige technologie. De informatiedichtheid van het geheel-optisch schakelen kan op een competitief niveau komen door gebruik te maken van plasmonische antennes. Een grote uitdaging voor het toepassen van het geheel-optisch schakelen op een grote schaal is het creëren van magnetische systemen die niet bestaan uit zeldzame aarden, maar wel de essentiële eigenschappen voor optisch schakelen bezitten. Een andere mogelijke toepassing van dit onderzoek is een relatief goedkoop en makkelijk alternatief voor het meten van ultrasnelle magnetisatiedynamica met elementgevoeligheid voor fundamenteel onderzoek. Onze voorgestelde methode kan daarom een bijdrage leveren aan een beter begrip van ultrasnelle processen en interacties in magneten.

---

## List of Publications

---

- **A. R. Khorsand**, M. Savoini, A. Kirilyuk, A. V. Kimel, A. Tsukamoto, A. Itoh, and T. Rasing, “Element specific probing of ultrafast magnetization dynamics in multi-sublattice magnets with visible light,” *Physical Review Letters*, **110**, 107205 (2013).
- **A. R. Khorsand**, M. Savoini, A. Kirilyuk, A. V. Kimel, A. Tsukamoto, A. Itoh, and T. Rasing, “Role of magnetic circular dichroism in all-optical magnetic recording,” *Physical Review Letters* **108**, 127205 (2012).
- **A. R. Khorsand**, M. Savoini, A. Kirilyuk, A. V. Kimel, A. Tsukamoto, A. Itoh, and T. Rasing, “Enhanced laser-induced demagnetization of an antiferromagnet in a transient ferromagnetic state,” (in preparation).
- A. Mekonnen, **A. R. Khorsand**, M. Cormier, A. V. Kimel, A. Kirilyuk, A. Hrabec, L. Ranno, A. Tsukamoto, A. Itoh, and T. Rasing, “Inter-sublattice exchange coupling in short-laser-pulse-induced demagnetization dynamics of GdCo and GdCoFe alloys,” (submitted).
- M. Finazzi, M. Savoini, **A. R. Khorsand**, A. Tsukamoto, A. Itoh, L. Duo, A. Kirilyuk, A. Kimel, T. Rasing, and M. Ezawa, “Laser-induced magnetic nanostructures with tunable topological properties,” (submitted).
- M. Savoini, R. Medapalli, B. Koene, **A. R. Khorsand**, L. Le Guyader, L. Duo, M. Finazzi, A. Tsukamoto, A. Itoh, F. Nolting, A. Kirilyuk, A. V. Kimel, and T. Rasing, “Highly efficient all-optical switching of magnetization in GdFeCo microstructures by interference-enhanced absorption of light,” *Physical Review B* **86**, 140404 (2012).

- R. Medapalli, I. Razdolski, M. Savoini, **A. R. Khorsand**, A. Kirilyuk, A. V. Kimel, T. Rasing, A. M. Kalashnikova, A. Tsukamoto, and A. Itoh, “The role of magnetization compensation point for efficient ultrafast control of magnetization in  $\text{Gd}_x\text{Fe}_{100-x-y}\text{Co}_y$  alloy,” *Physical Review B* **86**, 054442 (2012).
- H. Tomita, **A. R. Khorsand**, T. T. Seki, A. Kirilyuk, A. Kimel, T. Rasing, and Y. Suzuki, “Optical pump and probe measurements of the magnetization dynamics in antiferromagnetically coupled Fe layers,” *Journal of the Magnetism Society of Japan* **36**, 24 (2012).
- R. Sobierajski, S. Bruijn, **A. R. Khorsand**, E. Louis, R. W. E. V. de Kruijs, T. Burian, J. Chalupsky, J. Cihelka, A. Gleeson, J. Grzonka, E. M. Gullikson, V. Hajkova, S. Hau-Riege, L. Juha, M. Jurek, D. Klinger, J. Krzywinski, R. London, J. B. Pelka, T. Plocinski, M. Rasinski, K. Tiedtke, S. Toleikis, L. Vysin, H. Wabnitz, and F. Bijkerk, “Damage mechanisms of MoN/SiN multilayer optics for next-generation pulsed xuv light sources,” *Optics Express* **19**, 193 (2011).
- **A. R. Khorsand**, R. Sobierajski, E. Louis, S. Bruijn, E. D. van Hattum, R. W. E. van de Kruijs, M. Jurek, D. Klinger, J. B. Pelka, L. Juha, T. Burian, J. Chalupsky, J. Cihelka, V. Hajkova, L. Vysin, U. Jastrow, N. Stojanovic, S. Toleikis, H. Wabnitz, K. Tiedtke, K. Sokolowski-Tinten, U. Shymanovich, J. Krzywinski, S. Hau-Riege, R. London, A. Gleeson, E. M. Gullikson, and F. Bijkerk, “Single shot damage mechanism of Mo/Si multilayer optics under intense pulsed xuv-exposure,” *Optics Express* **18**, 700 (2010).
- J. Chalupsky, J. Krzywinski, L. Juha, V. Hajkova, J. Cihelka, T. Burian, L. Vysin, J. Gaudin, A. Gleeson, M. Jurek, **A. R. Khorsand**, D. Klinger, H. Wabnitz, R. Sobierajski, M. Stormer, K. Tiedtke, and S. Toleikis, “Spot size characterization of focused non-gaussian x-ray laser beams,” *Optics Express* **18**, 27836 (2010).
- A. J. Nelson, S. Toleikis, H. Chapman, S. Bajt, J. Krzywinski, J. Chalupsky, L. Juha, J. Cihelka, R. Sobierajski, **A. R. Khorsand**, V. Hajkova, L. Vysin, T. Burian, M. Kozlova, R. R. Faustlin, *et al.*, “Soft x-ray free electron laser microfocus for exploring matter under extreme conditions,” *Optics Express* **17**, 18271 (2009).
- E. Louis, **A. R. Khorsand**, R. Sobierajski, E. D. van Hattum, M. Jurek, D. Klinger, J. Pelka, L. Juha, J. Chalupsky, J. Cihelka, V. Hajkova, U. Jastrow, S. Toleikis, H. Wabnitz, K. Tiedtke, J. Gaudin, E. M. Gullikson, and F. Bijkerk, “Damage studies of multilayer optics for xuv free electron lasers,” *Proc. of SPIE* **7361**, 73610I (2009).



- 
- B. Nagler, U. Zastrau, R. R. Faustlin, S. M. Vinko, T. Whitcher, A. J. Nelson, R. Sobierajski, J. Krzywinski, J. Chalupsky, E. Abreu, **A. R. Khor-sand**, S. Bajt, T. Bornath, T. Burian, H. Chapman, *et al.*, “Turning solid aluminium transparent by intense soft x-ray photoionization,” *Nature Physics* **5**, 693 (2009).





---

## Curriculum Vitae

---

**Name:**  
Khorsand, Sam  
**Date of birth:**  
May 17, 1984  
**Place of birth:**  
Tehran, Iran

1997–2003      VWO, Markenhage College, Breda.

2003–2006      Bachelor studies in Physics (cum laude), Utrecht University.

2006–2008      Master studies in Physics (cum laude), Utrecht University.

2007–2009      Junior scientist in the group of Prof. Fred Bijkerk, DIFFER  
(formerly FOM Rijnhuizen), Nieuwegein.

2009–2013      PhD researcher in the group of Prof. Theo Rasing, Radboud  
University, Nijmegen.